NAVY- **AD-A276 412**

MEASUREMENTS OF VORTICITY VECTORS IN COUETTE FLOW WITH THE VORTICITY OPTICAL PROBE

DTIC
ELECTE
MAR 0 4 1994
S E D

Prepared by
R. Daniel Ferguson
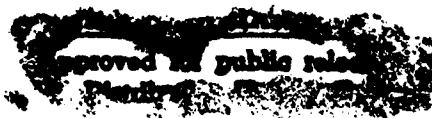Michael B. Frish
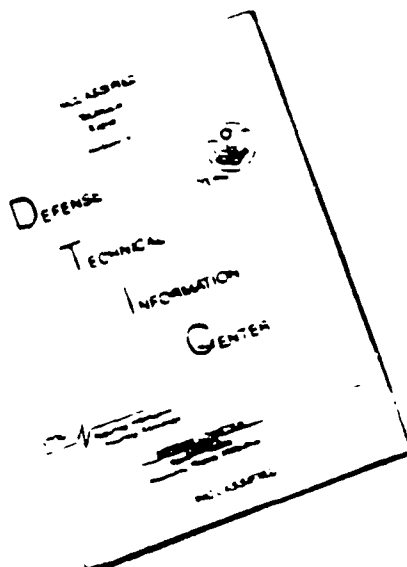Physical Sciences Inc.
Andover, MA 01810

February 1991

94-06621

DISCLAIMER NOTICE

THIS DOCUMENT IS BEST QUALITY AVAILABLE. THE COPY FURNISHED TO DTIC CONTAINED A SIGNIFICANT NUMBER OF PAGES WHICH DO NOT REPRODUCE LEGIBLY.

REPORT DOCUMENTATION PAGE

1a. REPORT SECURITY CLASSIFICATION Unclassified	1b. RESTRICTIVE MARKINGS
2a. SECURITY CLASSIFICATION AUTHORITY Unclassified	3. DISTRIBUTION / AVAILABILITY OF REPORT
2b. DECLASSIFICATION / DOWNGRADING SCHEDULE	
4. PERFORMING ORGANIZATION REPORT NUMBER(S) PSI-1093/TR-1103	5. MONITORING ORGANIZATION REPORT NUMBER(S) Item No. 0002, Sequence A002

6a. NAME OF PERFORMING ORGANIZATION Physical Sciences Inc.	6b. OFFICE SYMBOL (If applicable) HK901	7a. NAME OF MONITORING ORGANIZATION DCAMO - Boston
6c. ADDRESS (City, State, and ZIP Code) 20 New England Business Center Andover, MA 01810		7b. ADDRESS (City, State, and ZIP Code) 495 Summer St. Boston, MA 02210-2184
8a. NAME OF FUNDING / SPONSORING ORGANIZATION Office of Naval Research	8b. OFFICE SYMBOL (If applicable) N00014	9. PROCUREMENT INSTRUMENT IDENTIFICATION NUMBER N00014-89-C-0004

8c. ADDRESS (City, State, and ZIP Code) 800 N. Quincy Street Arlington, VA 22217	10. SOURCE OF FUNDING NUMBERS

PROGRAM ELEMENT NO	PROJECT NO	TASK NO	WORK UNIT ACCESSION NO

11. TITLE (Include Security Classification)

Measurements of Vorticity Vectors in Couette Flow with the Vorticity Optical Probe (U)

12. PERSONAL AUTHOR(S)
R. Daniel Ferguson and Michael B. Frish

13a. TYPE OF REPORT Draft Final	13b. TIME COVERED FROM 10/10/88 TO 5/31/91	14. DATE OF REPORT (Year, Month, Day) May 1991	15. PAGE COUNT

16. SUPPLEMENTARY NOTATION

17. COSATI CODES			18. SUBJECT TERMS (Continue on reverse if necessary and identify by block number)
FIELD	GROUP	SUB-GROUP	

19. ABSTRACT (Continue on reverse if necessary and identify by block number)

A prototype Vorticity Optical Probe (VOP) electro-optical system, data reduction and analysis procedures, and algorithms were developed and tested in this Phase II SBIR program. Also, a new type of VOP probe particle, made with acrylamide gel, was invented in this program. This achievement permits the VOP to be used in water. The VOP system was employed in a study of the vorticity fields in several precision Couette flow regimes. The measured vorticity statistics compared favorably with expected values. Several new results are reported.

20. DISTRIBUTION / AVAILABILITY OF ABSTRACT ☒ UNCLASSIFIED/UNLIMITED ☐ SAME AS RPT ☐ DTIC USERS	21. ABSTRACT SECURITY CLASSIFICATION Unclassified
22a. NAME OF RESPONSIBLE INDIVIDUAL Patrick Purtell	22b. TELEPHONE (Include Area Code) (703) 696-4405	22c. OFFICE SYMBOL 1132F

DD FORM 1473, 84 MAR   83 APR edition may be used until exhausted.
                              All other editions are obsolete.   UNCLASSIFIED

Contents

Figures

Tables

ACKNOWLEDGMENTS

LIST OF SYMBOLS, ABBREVIATIONS, AND ACRONYMS

F_R	-	flatness of $R(\omega)$ relative to normal distribution
$M(\overline{\omega}, \Delta t)$	-	rotation matrix
$P_n(t)$	-	n^{th} order orthogonal polynomial
$R(\overline{\omega})$	-	resolution function
R_c	-	Couette flow critical Reynolds number (inner cylinder)
R_i	-	Couette flow Reynolds number (inner cylinder)
R_o	-	Couette flow Reynolds number (outer cylinder)
R_s	-	shear flow Reynolds number
$S(\overline{\omega})$	-	sampling function
SNR	-	signal-to-noise ratio of raw trajectory data
a	-	particle radius
$\overline{a}$	-	vector describing trajectory geometry
b	-	impact parameter between particles on different streamlines in a shear
$\overline{c}$	-	vector describing trajectory geometry
d	-	particle diameter
e_{ij}	-	rate-of-strain tensor
f	-	frequency
h	-	perpendicular distance from particle center to wall
$\hat{n}$	-	mirror normal unit vector
$p(\overline{\omega})$, $p(\omega_i)$	-	probability density functions (PDFs)
$p(r_N)$	-	additional PDFs
$p(\sigma_i)$	-	additional PDFs
$p(SNR)$	-	additional PDFs
r	-	local rate of passage of reflection on detector
$\overline{r}$	-	arbitrary position vector on detector plane w.r.t ($x=0$, $z=0$)
r_N	-	angular size of N-point trajectory when y_d is normalized to 1 (unit sph
$r_{N,min}$	-	smallest allowed trajectory length for valid measurement
s	-	shear rate
$\overline{u}(\overline{x},t)$	-	velocity field
u_i or u,v,w	-	velocity components
y_d	-	effective distance from imaged sampled volume to detector plane
$\Delta\omega_T$	-	rms vorticity fluctuations
Δt	-	data sampling period
Δt_{opt}	-	optimum differencing interval for computing θ' and ϕ' derivatives
Ω	-	angular velocity
υ	-	Kolmogorov microscale of velocity

α	-	volume fraction of particles in fluid; also arbitrary dimensionless constant
$\overline{\gamma}$	-	general parameter space vectors
$\overline{\beta}$	-	general parameter space vectors
χ_ν^2	-	goodness-of-fit parameter
$\delta\omega_i$	-	rms instrumental broadening
ϵ	-	energy dissipation rate (per unit mass)
ν	-	Kolmogorov microscale of length
$\overline{\gamma}$	-	vector describing trajectory geometry
μ	-	dynamic viscosity
ν	-	kinematic viscosity
$\overline{\omega}(\overline{x},t)$	-	vorticity field
ω_i	-	vorticity components
ω_i'	-	VOP geometry vorticity basis
ψ	-	local angle of inclination of trajectory
ρ_f	-	fluid density
ρ_p	-	probe particle density
σ_i	-	vorticity component uncertainties
$\sigma_{i,max}$	-	range of uncertainties
$\sigma_{i,min}$	-	range of uncertainties
σ_R^2	-	variance of $R(\omega)$ relative to normal distribution
τ	-	*Kolmogorov microscale of time*
τ_D	-	detector transit time
τ_e	-	mean time between events
τ_r	-	rotational relaxation time
τ_{sr}	-	sampled volume transit time
τ_v	-	translational relaxation time
(θ,ϕ)	-	mirror normal angular coordinators
(θ',ϕ')	-	reflection angular coordinates
ℓ_u	-	dimension of sampled volume along direction of convection velocity
ℓ_ω	-	angular size of trajectory on unit sphere (how much the reflection rotates in traversing ℓ_u)
$\partial\psi/\partial r$	-	local curvature of trajectory

PROJECT SUMMARY

This report describes the work performed at Physical Sciences Inc. (PSI) as a Phase II Small Business Innovative Research (SBIR) program sponsored by the Office of Naval Research. The general goal of this program was the continued development of the flow measurement technique known as the Vorticity Optical Probe (VOP). The specific objectives of the program were to demonstrate that: 1) automated, time-resolved vorticity vector measurements can be accurately performed at a single well-defined point within a flowfield; 2) the VOP measures the correct vorticity statistics in a turbulent flowfield; and 3) the VOP can be made to work in water with a new type of water-compatible probe particle.

These three goals have been met during this program. An engineering prototype VOP electro-optical system and a data reduction and analysis algorithm were developed and tested. This VOP system was employed in the study of several precision Couette flow regimes, including laminar, turbulent and periodic flow. The measured vorticity statistics compared favorably with expected values. Finally, a new type of vorticity probe particle, made with acrylamide gel, was invented in this program. This invention permits the VOP technique to be used with water as the working fluid. In many respects, the new water-compatible particles are superior probes to those used previously in non-aqueous working fluids. The use of these particles for vorticity vector measurements in laminar, periodic, and turbulent Couette flow has been demonstrated.

The remainder of this report details these accomplishments in six chapters: Chapter 1 is a general introduction to the VOP. Chapter 2 describes the fundamentals of vorticity measurement. Chapter 3 is a detailed account of the full VOP system in its current form. Chapter 4 describes water-compatible probe particle properties and manufacture. Chapter 5 is the presentation and interpretation of the new precision Couette flow vorticity vector data. Lastly, Chapter 6 summarizes the progress on the VOP to date and examines possible future directions in VOP application and development.

1. INTRODUCTION

> "The importance of vorticity for the understanding and description of the
> turbulent flow or high Reynolds number motion of a uniform, incompressible
> fluid cannot be over-emphasized."
>
> -P.G. Saffmం

The observation of Saffman quoted above, and similar sentiments from countless other investigators of t

flow phenomena, have resounded through the fluid dynamics community for many decades. It is only v

the past decade, however, that a systematic exploration of the vorticity field of turbulent flow has becoะ

possible. This recent progress is the result of two significant developments. First, the explosive growtł

the past decade of high-speed computers (approaching 10^9 operations/sec) capable of resolving features

fundamental interest in turbulence theory, and second, new experimental methods for vorticity measurer

which have been recently devised, of which the vorticity optical probe is one. (For reviews of these mเ

see Wallace, 1986 or Foss and Wallace, 1989.)

The interest in vorticity measurement reflects the growing recognition in the fluid dynamics community

dominance of coherent structure in turbulent shear flow. Hussain (1986) has dubbed these "coherent vɾ

to emphasize the rotational nature of these objects, and to distinguish them from irrelevant large scale n

the background flow. This was also noted specifically by Laufer (1975), in his discussion of the kinem

what he calls the "quasi-ordered" structure of turbulence; "... vorticity measurements suggest themselve

most promising method for the quantitative study of the ordered motion. Unfortunately, there are sever

serious difficulties with this method: 1) direct measurement of vorticity has not yet been successfully

accomplished with sufficient accuracy; 2) single-point measurements are inadequate; and 3) following tł

vorticity-containing fluid in a Lagrangian sense is intrinsically difficult".

The first difficulty has been substantially overcome by the vorticity optical probe (VOP, Frish and Web

1981). The three components of the vorticity vector are measured, any two of them quite accurately.

Multipoint measurement arrangements have been devised (Ferguson and Webb, 1983). And lastly, the

optical probe has 'quasi-Lagrangian' character in that the vorticity is measured at the location of probe particles, as they convect passively through the sampled region.

The vorticity vector, defined in Subsection 1.1 below. It describes the rotation of a material point in the flowfield. The methods of vorticity measurement in the flow interior are divided into two categories: those which estimate vorticity or vorticity components from finite-difference approximations of the local velocity field derivatives, and direct measurements (i.e., not implicitly dependent upon velocity measurements) of the local rotation rate of fluid elements.

In the first category, finite-difference based methods place a restrictive upper limit upon the accessible Reynolds number of the flow in the laboratory like their computational counterparts on grids of finite resolution. Alternately expressed, the dimension of the finite-difference element sets a limit of spatial resolution. Free shear flows and, generally, non-parallel flows place even greater burdens upon the capabilities of finite-difference techniques due to the questionable nature of Taylor's hypothesis applied to the rapidly changing length scales and velocities in these flowfields.

The second category, direct measurement of vorticity, to our knowledge has only two members: a recently developed forced Rayleigh scattering technique (Agui Garcia and Hesselink, 1990), and the Vorticity Optical Probe (VOP). The VOP technique was developed by Frish and Webb (1981) specifically to address the problem of resolving the smallest scales of intense turbulence, even in the presence of powerful mean shear. In its present form, the VOP measures three components of vorticity in virtually any geometry, in liquid flows including water.

1.1 Motivation

Why measure vorticity? The vorticity field, $\vec{\omega}(\vec{X},t)$, which has been called the "sinews and muscles of fluid motion" (Küchemann, 1965), is defined as the curl of the velocity field $\vec{u}(\vec{X},t)$;

3

$$\overline{\omega} = \nabla \times \overline{u} \quad .$$

Taking the curl of the vorticity field, we have

$$\nabla \times \overline{\omega} = \nabla \times (\nabla \times \overline{u}) = \nabla(\nabla \cdot \overline{u}) - \nabla^2 \overline{u} \quad .$$

For incompressible flow with $\nabla \cdot \overline{u} = 0$

$$\nabla^2 \overline{u} = \nabla \times \omega \quad .$$

The solution of this equation for $\overline{u}$ is given by

$$\overline{u}(\overline{X}) = \frac{1}{4\pi} \int \frac{\hat{r} \times \overline{\omega}}{r^3} d^3 \overline{X}' + \nabla \phi$$

where $r = |\overline{X} - \overline{X}'|$, the integration is performed over the domain of non-zero vorticity, and ϕ is the
of an arbitrary irrotational flowfield.

The first obvious consequence this solution is that the velocity field is specified by the vorticity field (to

the gradient of scalar potential determined by the boundary conditions). The second consequence is that

most important action in any flowfield takes places where the vorticity resides, and important features o

flow can often be described by vorticity measurement over relatively small regions of the flowfield.

Vorticity is transported by the flow. For inviscid flow, the circulation about any open material surface

flow, which is equal to the flux of vorticity through that surface, is a conserved quantity (Batchelor, 196

$$\frac{d}{dt} \left[\int_s \overline{\omega} \cdot d\overline{s} \right] = 0 \quad .$$

In viscous flow, the Navier-Stokes equations are written (in the Eulerian frame)

$$\frac{D\omega_i}{Dt} = \omega_j \cdot e_{ij} + \nu \nabla^2 \omega_i$$

4

(with the usual summation convention on repeated indices) where e_{ij} is the rate-of-strain tensor. Because $\overline{\omega}$ (and e_{ij}) are invariant under Galilean transformation, the Lagrangian vorticity equations are

$$\frac{\partial \omega_i}{\partial t} = \omega_j \cdot e_{ij} + \nu \nabla^2 \omega_i$$

and the intrinsic rate-of-change of the vorticity vector at a material point is seen to be due only to the action of viscous diffusion or the stretching due to e_{ij}.

Finally, the enstrophy per unit volume, $|\omega^2|$ (the rotational analog of energy $|u|^2$), is directly proportional to the local energy dissipation rate per unit mass, ϵ

$$\epsilon \approx \nu |\omega|^2 \quad .$$

From the discussion above, it is seen that many of the quantities that characterize the dynamics of turbulent flow are intimately bound together in the vorticity field, whereas the connections to the velocity field statistics are often more subtle, and inherently less efficient descriptors of turbulence. It is not unreasonable to expect that vorticity correlations will provide much more powerful descriptions of the coherent structures and vortex interactions which are at the leading edge of turbulence research.

An example of the efficiency of the vorticity field description is seen in Figure 1. Figure 1(a) shows velocity measurements in a plane of a single-sided wake producing a 2-D map of an apparently complex flow pattern (Perry and Chong, 1987). A number of singularities are in evidence, including foci, nodes and saddles (F,N,S). A full description of the flowfield would ordinarily require many such planes. Figure 1(b) shows a postulated "vorticity skeleton" of the flow, and the resulting velocity field computed from Eq. (2). The vorticity field in this case is a kind of hydrodynamic shorthand describing the essential topology of the flowfield.

In addition to these very fundamental reasons for vorticity studies, there are many highly practical motivations as well. Propagating acoustical signatures due to turbulence are closely related to vorticity dynamics, and are associated with the time rate-of-change of the (low) pressure field in the cores of intense vortices (Kambe, 1986). Flows near boundary layer control devices and structure junctions are often vortex dominated flows.

5

Velocity 0 5 m/s   10 mm Length
Scale ———→   ——— Scale
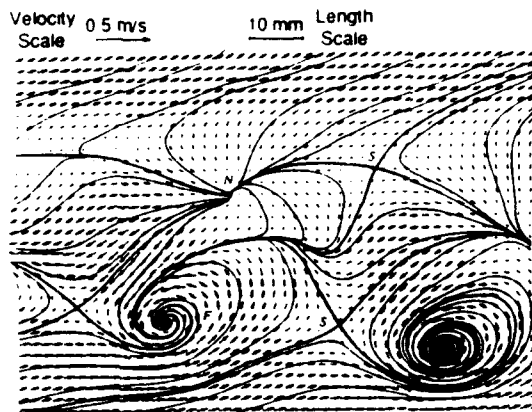
(a) Typical Instantaneous (phase-averaged) Velocity Vector Field for a
Single-Sided Wake Pattern Using a Hot Wire Probe

⟨☐ Jet   Wake ☐⟩

☉ 7K   ☉ 7K   ☉ 7K

B-7409
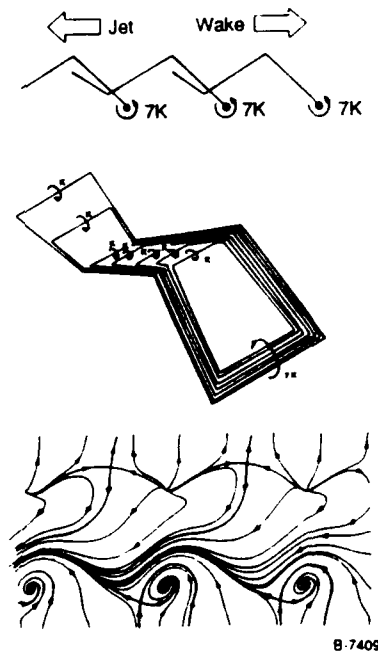
(b) (top) Side View of Vortex Skeleton for Single-Sided Structure.
(middle) Oblique view of a typical cell. K denotes a unit of circulation.
(bottom) Commputed velocity field using the Biot-Savart law (as seen by an observer moving with the c

Figure 1

Representation of a Complex Flow Pattern with a Vortex Skeleton (from Perry and Chong, 1987)

6

The behavior of high helicity $(\overline{\omega} \cdot \overline{u})$ flows (Moffatt, 1969) and swirling flows, turbomachinery and propulsor flows, is strongly affected by vorticity concentrations at inlets. Periodic flows and wake development can is best described in terms of shed vortex interactions. Also, computations are frequently formulated in terms of vorticity to take full advantage of the economy of description afforded by the vorticity field in many flows (e.g., Aref and Siggia, 1980).

1.2 Background

The development of the VOP to date is sketched briefly in the following sections.

1.2.1 VOP History

The VOP was invented by M.B. Frish at Cornell University as part of his doctoral thesis research (1981). The first direct optical vorticity measurements were single component measurements in laminar Poiseuille flow and in a transitional boundary layer (Frish and Webb, 1981). This work was continued at Cornell by Ferguson, who developed the multi-component VOP sensor based upon a dual-axis position-sensing photodiode detector. Ferguson performed the first direct optical measurements of two vorticity components simultaneously (Ferguson and Webb, 1984). This version of the VOP possessed the potential of three component vorticity measurement. The development of the VOP was continued by Frish and Ferguson at Physical Sciences Inc. (PSI) commencing with an ONR-sponsored Phase I SBIR program in 1987, described below.

1.2.2 Phase I Program

The Phase I SBIR program at PSI had two basic objectives. The first objective was to demonstrate that the VOP technique could be extended to three-component vorticity measurement using a single detector surface of finite solid-angle. The second objective was to demonstrate the volumetric potential of the VOP, by measuring vorticity vectors at several distinct locations within a large sampled volume simultaneously. A method was devised to independently determine the positions of the individual measurement points within the volume.

vorticity vectors at several distinct locations within a large sampled volume simultaneously. A method wa devised to independently determine the positions of the individual measurement points within the volume.

At the successful conclusion of the Phase 1 program, the Phase II program, which is the subject of this re: was begun. The goals of this program are summarized in the next section.

1.3 Phase II Goals and Accomplishments

The specific objectives of the Phase II program were to: 1) develop an automated instrument to acquire t resolved vorticity vector measurements at a single well-defined point within a flowfield; 2) demonstrate th VOP measures the correct vorticity statistics in a turbulent flowfield; and 3) make the VOP work in watei

These three goals have been met. An engineering prototype VOP electro-optical system and a data reduci and analysis algorithm were developed and tested. This VOP system was employed in the study of sever: precision Couette flow regimes, including laminar, turbulent and periodic flow. The measured vorticity statistics compared favorably with expected values from several sources. Finally, a new type of vorticity particle made with acrylamide gel was invented, which permits the VOP technique to be used with water working fluid. In many respects, the new water-compatible particles are superior probes to those used previously in non-aqueous working fluids. The use of these particles for vorticity vector measurements ir laminar, periodic, and turbulent Couette flow has beer demonstrated.

8

2. FUNDAMENTALS OF VORTICITY MEASUREMENT

2.1 Overview

From the definition of the vorticity field as the curl of the velocity field, $\vec{u}$,

$$\vec{\omega} = \nabla \times \vec{u}$$

it is a straightforward task to devise an experiment, at least in principle, in which the local vorticity vector may be estimated from several (Eulerian) velocity measurements at strategically chosen positions. One would, as a simple example, measure the velocity vector (u,v,w) at four positions ,i.e., $\overline{X}_0 = (x_0,y_0,z_0)$, (x_0+dx,y_0,z_0), (x_0,y_0+dy,z_0), and (x_0,y_0,z_0+dz). From the spatial Taylor expansion of the velocity field at $\overline{X}_0$, it is evident that good estimates of the velocity derivatives (and thus the vorticity vector) at position $\overline{X}_0$, can always be obtained, provided suitable restrictions are placed upon the size of the increments, $d\overline{X}$. Mathematically, these restrictions on the size of $d\overline{X}$ need only guarantee the smallness of second and higher order terms which contribute the error in gradient estimates, while minimizing the differentiation error in the gradient calculation which grows rapidly with decreasing dX in the presence of noise. In practice, sophisticated finite differencing schemes are routinely employed for velocity gradient estimation in experimental (or computational) applications (Wallace, 1986, and Foss and Wallace, 1989). Unfortunately, turbulence in real fluids introduces difficulties at the outset.

For a fluid of given viscosity, ν, the dissipation rate, ϵ, fixes the (Kolmogorov) microscale of the turbulence, $\eta = \left[\dfrac{\nu^3}{\epsilon} \right]^{1/4}$. This is the length scale at which viscous dissipation strongly damps local vorticity or velocity field fluctuations and therefore is expected to be a suitable order of magnitude of the increment, $d\overline{X}$ (Wynguard, 1969; Klewicki and Falco, 1990). Selecting a finite $d\overline{X}$ in an actual physical realization of such an experiment usually imposes a restrictive upper limit on the Reynolds number accessible to such measurements. Larger Reynolds numbers result in turbulent length scales in the flow which are smaller then the probe dimensions, resulting in the washing out of small-scale structure and possible aliasing of the vorticity measurements. The Nyquist sampling theorem applies equally to spatial resolution issues.

A more subtle problem arises when considering the time dependence of the flowfield. The implicit assum of the foregoing discussion is that the Lagrangian time derivatives of the velocity components are negligib comparison with the convective part of the total (material) derivative.

$$\frac{\partial}{\partial t} \ll u \cdot \frac{\partial}{\partial x} \quad .$$

In other words, the flowfield is assumed to pass through the (Eulerian) probe region unchanged, as if "fro Taylor's frozen flow hypothesis is then

$$\frac{\partial}{\partial X} = - \frac{1}{U_c} \frac{\partial}{\partial t}$$

suggesting that streamwise spatial derivatives can estimated from time derivatives of measured quantities a point where U_c is the convection velocity. Clearly this is true in turbulent flow only when U_c is sufficien large and constant. Great care must be exercised in measuring low-speed and highly non-parallel flows u finite difference techniques which rely in part upon Taylor's hypothesis (Piomelli, Balint, and Wallace, 1 The application of hot-wire anemometry or laser-doppler techniques (Lang and Dimotakis, 1982) to finite difference velocity gradient measurements also suffer from velocity measurement-related errors and probe interference or interaction, particularly near flow boundaries. Limited spatial resolution and the problema nature of high vorticity (i.e., near-wall) regions, obscures much of the interesting vorticity dynamics.

The other major class of vorticity measurement techniques comprises those which attempt to directly obse local deformation tensor. By whatever means this is accomplished, e.g., grids optically 'painted' in phote dyes, etc. (Fermigier, Cloitre, Guyon, and Jenffer, 1982; Chu and Falco, 1987), these are essentially qua flow visualization techniques. Local deformations of the fluid markers are analyzed to yield the fluid ang velocity about at least one axis. Particle imaging velocimetry (PIV) (Utami and Ueno, 1987; Agüi and Ji 1987; Adrian, 1991) is member of this family. These approaches still rely implicitly upon the calculation Lagrangian velocity field point by point, and subsequently, its gradients. These methods gain vorticity pr the expense of spatial resolution up to a limit set by the length microscale of the flow and incur large err that for the reasons cited. The Eulerian probes described above make similar compromises depending on

10

The VOP is a direct approach to vorticity vector measurement. It provides fixed spatial resolution limited only by particle size, but trades vorticity precision against temporal resolution. No velocity measurements are implicit in the method. The rotation of a sub-Kolmogorov scale fluid element containing a small particle is probed directly as it moves along a streamline. At very high Reynolds number, the VOP does not alias the data. Behaving rather like low pass vorticity filter, the small scales average out. The precision of the vorticity measurement in the fluid element is determined roughly by the length of time for which it can be observed. This time interval must not exceed the Kolmogorov micro-scale of time, $t = (\nu/\epsilon)^{1/2}$.

2.2 The Vorticity Optical Probe Concept

The VOP is an elegantly simple concept. A small (20 to 50 μm) spherical particle suspended in a viscous flow will quickly spin up under the action of viscous stresses at the particle's surface. The torque exerted on a sphere is proportional to difference between the sphere's angular velocity vector, $\overline{\Omega}$, and the angular velocity of the surrounding fluid, $\overline{\omega}/2$ (for local vorticity, $\overline{\omega}$). The sphere's final angular velocity (when the torque is zero) is then

$$\overline{\Omega} = \frac{\overline{\omega}}{2} \tag{4}$$

which is approached exponentially with a relaxation time of τ,

$$\tau_r = \frac{1}{15} \frac{a^2}{\nu} \frac{\rho_p}{\rho_f} \ . \tag{5}$$

where a is the particle radius, and ρ_p and ρ_f are the densities of particle and fluid, respectively. The small masses and moments of inertia of the spheres developed for this purpose insure that they react to the fastest fluctuations of velocity and vorticity in turbulent flow (Subsection 2.4.2 below).

The symmetric part of the local deformation tensor, the rate-of-strain tensor, e_{ij} has no influence upon the orientation of the particle due to the particle's spherical symmetry. Thus a measurement of the local vorticity vector in the fluid reduces to a measurement of the probe particle's angular velocity vector. The method for

11

angular velocity measurement is to reflect a beam of light from a highly reflective planar facet on or in th

particle, and observe the sweeping reflection.

To perform these measurements, Frish (1981) invented a method of encasing microscopic plane mirrors (

carbonate crystal platelets) in 20 to 30 μm clear plastic spheres having refractive indices that match the w

fluid in which they are dispersed as probes. Each particle is mechanically spherical, but optically planar

reflections and refractions are effectively eliminated at the particle surface by index matching. Only the

embedded mirror(s) remain visible. A beam of laser light reflected from a probe particle at a known loca

the fluid, is recorded as a function of time. From the reflection's angular displacements, the particle's an

velocity vector, and thus the local vorticity of the fluid, is deduced.

Following the discussion of VOP geometry in Subsection 2.3 below, a complete discussion of vorticity pr

particles, including their properties in various fluids, manufacturing methods, etc., will be presented in

Subsection 2.4. The three component vorticity measurement system is described in detail in Chapter 3.

2.3   VOP Geometry and Trajectory Analysis

The basic VOP configuration is shown in Figure 2. The laser is incident from the positive z-direction.

plane upon which the passage of the reflected beam is observed is referred to as the detector plane. The

of the reflected beam emanating from the origin, where it intersects the detector plane, is henceforward r

to as a 'reflection trajectory', or simply 'trajectory'. The mirror-normal unit vector, $\bar{n}$, has the usual poi

coordinates, θ and ϕ, defined with respect to the positive z and x axes, respectively. The angular coordir

the reflected beam are θ' and ϕ'. For reasons that become clear in the following sections, the primed ba

of vorticity vectors is preferred to that defined by the coordinate axes.

| Incident Beam and Detector Plane | Primed Vorticity Basis Vectors |

8-6940
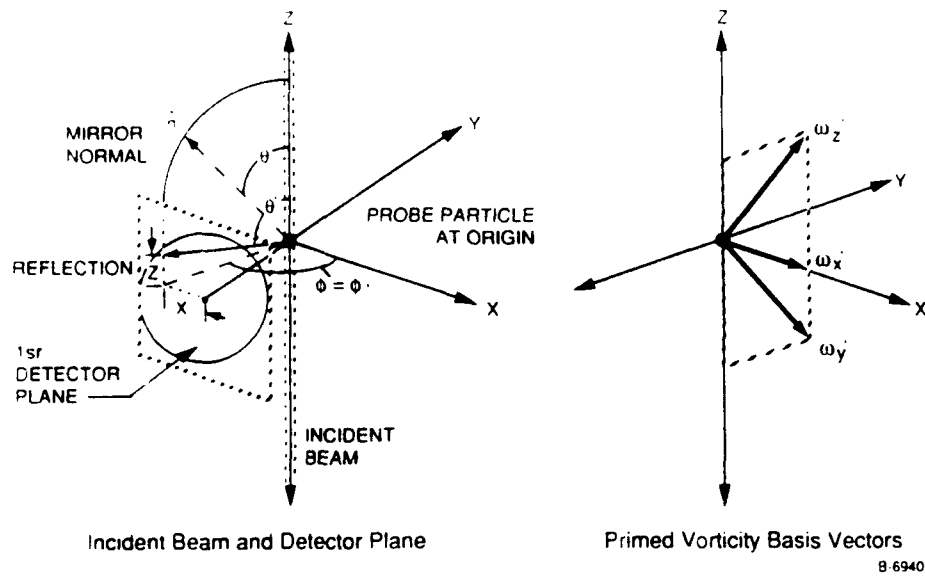
Figure 2

VOP Coordinate System

2.3.1 Differential Trajectory Equations

In time Δt, the vorticity vector carries the mirror-normal vector from its orientation when first detected, $\hat{n}_0$, to a new orientation, $\hat{n}_1$, by the action of the rotation matrix, $M(\overline{\omega},\Delta t)$. The complete mirror-normal trajectory consist of m vectors in time $m\Delta t$ and has the representation;

$$\{\hat{n}_0,\hat{n}_1,\hat{n}_2,...\hat{n}_m\} = [M_0,M_1,...M_m]\hat{n}_0 \quad .$$

The reflection trajectory is simply related to the mirror-normal trajectory as described below. This procedure was adopted for computing the trajectory simulations in Subsection 2.3.2 below, explicitly in terms of the rotation matrix and a starting vector, $\overline{n}_0$. However, n(t) is not linear in the vorticity componets. This trajectory generator has been used in a non-linear regression algorithm for trajectory analysis, but a serious disadvantage of this approach is that it is quite computationally intensive. We have therefore adopted a linearized method utilizing the rate-of-change of the mirror-normal angular coordinates.

The rate-of-change of the mirror-normal vector is related to the vorticity vector by:

$$d\hat{n}/dt = \frac{\overline{\omega}}{2} \times \hat{n}$$

Writing the mirror-normal components as

$$n_x = \sin \theta \cos \varphi$$

$$n_y = \sin \theta \sin \phi$$

$$n_z = \cos \theta$$

differentiating Eq. (6) with respect to time and solving for $d\theta/dt$ and $d\phi/dt$ gives

$$\frac{d\theta'}{dt} = \frac{1}{2}(\omega_y \cos\phi' - \omega_x \sin\phi')$$

$$\frac{d\phi'}{dt} = \frac{\omega_z}{2} - \frac{\cot\theta}{2}(\omega_x \cos\phi + \omega_y \sin\phi) \quad .$$

But the reflection (primed) coordinates are simply related to the unprimed coordinates as

$$\phi' = \phi$$
$$\theta' = 2\theta$$

thus the relationship between the rates-of-change of the reflection coordinates and the vorticity vector

$$\frac{d\theta'}{dt} = (\omega_y \cos\phi' - \omega_x \sin\phi')$$

$$\frac{d\phi'}{dt} = \frac{\omega_z}{2} - \frac{1}{2}\cot\frac{\theta'}{2}(\omega_x \cos\phi' + \omega_y \sin\phi') \quad .$$

Expressed in the primed vorticity basis:

$$\frac{d\theta'}{dt} = A\omega'_z + B\omega'_y + C\omega'_x$$

$$\frac{d\phi'}{dt} = D\omega'_z + E\omega'_y + F\omega'_x$$

where the coefficients A-F are

$$A = B = \frac{1}{\sqrt{2}} \cos\phi', \quad C = -\sin\phi'$$

$$D = \frac{1 - \cot\frac{\theta'}{2}\sin\phi'}{2\sqrt{2}} \quad , \quad E = \frac{-\left[1 + \cot\frac{\theta'}{2}\sin\phi'\right]}{2\sqrt{2}} \quad , \quad F = -\frac{1}{2}\cot\frac{\theta'}{2}\cos\phi' \quad .$$

Equations (4) through (7) are called the differential trajectory equations (DTEs). A trajectory consisting of many (θ'_i, ϕ'_i) pairs at fixed time intervals generates many such equations using finite difference estimates of the θ' and ϕ' derivatives. The vorticity components are then extracted by a simple linear least-squares analysis (see Subsection 3.2.8)

2.3.2 Trajectory Simulations

What ought these trajectories look like, and what assurance can be given of uniqueness of the vorticity vectors deduced from them? The initial orientation of mirror-normal vectors for particles moving through the sampled (laser-illuminated) volume is completely random. Thus, for a single fixed vorticity vector, there exists a family of possible trajectories on the detector surface corresponding to all of the possible starting positions of the mirror-normal vectors. Figure 3 shows several representative trajectory families corresponding to the vorticity values indicated. Figure 3(a) shows the case of pure ω'_x, while Figure 3(b) includes ω'_z. Clearly ω'_x and ω'_z are more or less directly related to the rate and angle of inclination of the trajectories' passage. The addition of ω'_y in Figure 3(c), however, gives rise to a subtle change in the trajectory curvatures. This curvature, and thus ω'_y, becomes easier to measure as trajectories become longer. In fact, the geometrical parameters, $\dot{r}$, the local rate of passage of the reflection, ψ, the local angle of inclination of the trajectory, and $\frac{\partial\psi}{\partial r}$, the local curvature, form a convenient alternate basis set from which the vorticity components may be estimated. The addition of trajectory curvature is what allows three independent vorticity components to be determined from the motion on a (two-dimensional) surface.

15

(a) Pure ω_x' (b) $\omega_x' = \omega_z'$

sr DETECTOR PLANE

(c) $\omega_x' = \omega_z' = \omega_y'$
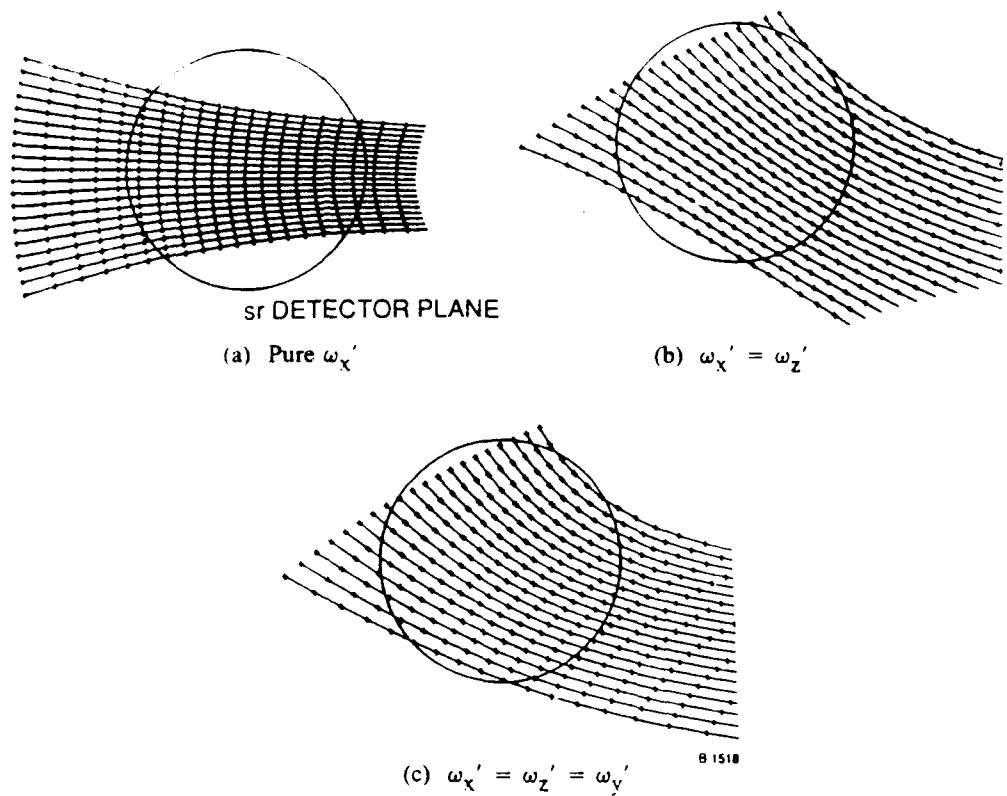
Figure 3

Some Reflection Trajectories

Note that trajectories never cross on the detector plane: for each initial mirror orientation, distinct vortic

vectors possess one and only one trajectory. The converse is certainly true: a full trajectory through a giv

point in the detector plane corresponds to a unique vorticity vector. However, one must be wary of the

singularity in the VOP geometry where trajectory uniqueness breaks down. Figure 4 shows a case of suc

singularity on the detector surface. The fixed point about which trajectories appear to orbit corresponds t

mirror-normal which happens to be parallel to the vorticity vector. In such a case, no information can be

obtained about the magnitude of the vorticity vector.

This null vorticity vector is the special case of a vorticity vector which is parallel to every mirror-normal.

results in an inherent "blind spot" in the VOP system. This does not mean that a vorticity value of zero

16
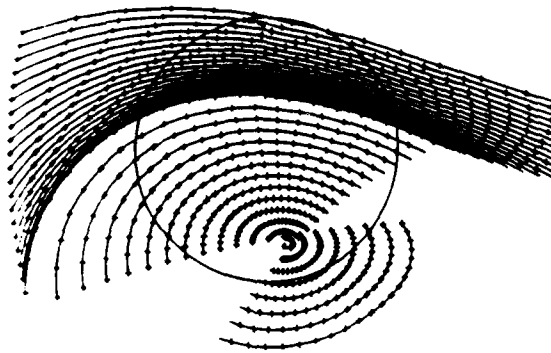
B-3096

Figure 4

The VOP Singularity

be measured, merely that it cannot be distinguished from the highly improbable situation of a finite vorticity vector parallel to the mirror-normal. Care must be taken in the interpretation these events.

At the center of the detector $(Z = 0, X = 0)$, the coefficients of the ω'_y vorticity component, B and E, in the DTEs, vanish. In this case accurate measuruments of the ω'_x and ω'_z components can be made without contamination from the uncertainty in the ω'_y value. It is reasonable to bundle all the uncertainty into ω'_y where it naturally resides (i.e., the primed vorticity basis is a diagonal representation), rather than mix it in the unprimed frame between ω_y and ω_z.

2.4   VOP Particle Characteristics

In evaluating the many VOP particle candidate materials tested in this program, mostly in the pursuit of water-compatibility, several basic guidelines of particle "design" have been applied for all particle/fluid systems. The essential features of any type of vorticity probe particles, be they solid, liquid, or visco-elastic material, are as follows:

1)   The optical properties of the particles must meet the minimum experimental requirements for acquiring useful data.

2)   The dynamic response of particles must be such that they follow the flow fluctuations at all length and time scales of interest.

17

3)   Intrinsic particle behavior must not compromise the simple interpretation of the measured angul.
velocity vector.

4)   Particle interactions must not unduly influence the turbulent statistics which are to be measured.

Each of these is considered in the following sections.

2.4.1 Optical Properties

Particles of optical quality consistent with the requirements of the VOP detection system to be discussed
Chapter 3 have the following features in common:

1)   Nearly diffraction limited reflection divergence from embedded mirrors which are free from dei
surface contamination. These mirrors should be of sufficient size to give acceptably small diver
(Basic lead carbonate, $3PbCO_3 \cdot 2Pb(OH)_2$, in the form of hexagonal crystal platelets of 15 μm
diameter and 0.06 μm thickness have been used almost exclusively to date.)

2)   Refractive index matching of the working fluid/particle system to a degree which meets the abo·
requirement and limits unwanted particle surface reflections.

3)   Optical transparency of the particle material minimizes scattered background light.

In order to maximize the accuracy with which reflection trajectories are determined over the limited soli
subtended by the detector surface, the smallest possible angular spread of the reflections is desired. A r
divergence of no more than 15 percent of the full cone angle subtended by the detector is a sensible lim.
an F1.5 optical system, this corresponds to a divergence angle of ≤ 6 deg. With 15 μm mirrors approx
5 deg of this is already taken up by diffraction. The Fraunhofer diffraction pattern of a circular apertur.

$$I(X) = \left[\frac{2J_1(X)}{X} \right]^2 \quad X = \frac{\pi}{\lambda} D \sin\theta \quad .$$

The first zero of $J_1(x)$ is at $X = 3.83$, and

18

$$\theta = 1.22\frac{\lambda}{D}$$

giving ~5 deg full cone angle for green light (the Argon ion laser line at 514.5 nm). The 5 deg full cone angle of the Airy disc contains 84 percent of the total reflected power.

Mismatching of refractive indices for fluid particle systems produces focusing effects at the curved particle surfaces. The particle surface near the embedded mirror shown in Figure 5 acts like a pair of thin lenses. For 2 percent matching, $\Delta n \sim 0.03$ with $D = 15 \mu m$

$$\frac{1}{f} \sim \Delta n \left[\frac{1}{r_1} + \frac{1}{r_2} \right] \quad , \quad f \sim \frac{1}{3} \text{ mm} \quad .$$

The farfield defocusing angle $D/f = 2.6$ deg. Therefore, index matching in the 1 to 2 percent range is necessary for holding total spot angular size near the 6 deg limit. This also leaves some room for improvement. Doubling the mirror diameter would nearly halve the cone angle and quadruple the total power in the reflection.

Ancillary benefits of good (≤ 1 percent) index matching include minimized surface reflections intensity into the collection optics, though this is of order $\left[\frac{\Delta n}{n_2 + n_1} \right]^2 \sim 10^{-4}$ near 45 deg incidence, not including geometrical
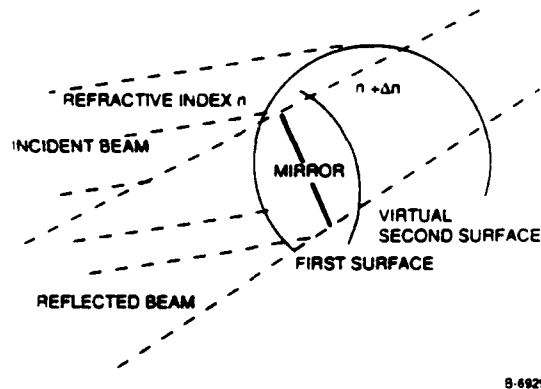
8-6929

Figure 5

Illustration of the Refractive Contribution to Farfield Reflection Divergence

19

spreading of reflections from the highly curved surfaces. Such reflections would be negligible even near 10 percent index matching. The more serious difficulty of this type, however, arises from low-angle surfa reflections and multiple low-angle internal reflections. In conjunction with beam extinction and diffractior to the mirrors, this can rapidly decrease optical depth and produce inhomogeneity in the incident and réfle laser light at high particle loading ($\sim 10^6$ particles/cm^3).

Some volume scattering from the particle material is acceptable. The fraction scattered into the detection from the few particles within the sampled volume at any one time will be orders of magnitude smaller tha reflection intensities.

2.4.2 Dynamic Response

VOP particles must not only track the translational motions of the surrounding fluid element, as is usuall concern in connection with LDV seed particles, but the angular velocity and accelerations of that fluid ele as well. For the translational part, the discussion of Buchhave, George and Lumley (1979) is recounted v some modifications.

If the Lagrangian velocity field is represented by Fourier components of random phase, then the dynamic response of the particle to the component at frequency f, $v = \bar{v}_0 \sin(2\pi f t + \phi)$, the solution of

$$\frac{\beta}{m}(\dot{x} - v) = \ddot{x}$$

is required, where $\dot{x} - v$ is the velocity of the particle relative to the local Lagrangian field and where β (Stokes) drag factor and m is the particle mass.

The solution gives the spectrum of the particle/fluid relative velocity

$$\Phi(f) = \frac{\tau_v^2 (2\pi f)^2}{1 + \tau_v^2 (2\pi f)^2}$$

where τ_v is the particle's response time.

To follow velocity fluctuations to ≤ 10 percent, requires $\tau_v(2\pi f) \leq 10^{-1}$. For $\Phi(f) \ll 1$, τ_v is obtained simply from the Stokes drag (Lumley, 1957)

$$\tau_v = \frac{a^2}{9\nu} \left[2 \frac{\rho_p}{\rho_f} + 1 \right]$$

The Kolmogorov microscales for two flow conditions in water are summarized in Table 1.

Table 1. Comparison of Turbulence Microscales and Particle Characteristics

Case 1	Case 2
for $u \sim 1$ ms water flow, $\ell \sim 10$ cm $\epsilon = u^3/\ell = 10^5$, $\nu = 0.01$ cm^2/s	for 6 ms over 2 cm $\epsilon = u^3/\ell \sim 10^8$
$\eta \sim 20$ μm $\upsilon \sim 6$ cm/s $\tau \sim 3 \times 10^{-4}$s $f \sim 3 \times 10^3$ s^{-1}	$\eta \sim 3$ μm $\upsilon \sim 30$ cm/s $\tau \sim 10^{-5}$s $f \sim 10^5$ s^{-1}
$\tau_v = \frac{a^2}{3\nu} \frac{\rho_p}{\rho_f} \sim 10^{-4}$s for 40 μm diameter neutrally buoyant particles in water	

The Kolmogorov microscales are the local scales that can be formed from the local dissipation rate ϵ ($\approx u^3/\ell$) and the kinematic viscosity ν. These are:

21

$$\text{velocity}, \; v = (\epsilon \nu)^{1/4}$$

$$\text{length}, \; \eta = \left[\frac{\nu^3}{\epsilon}\right]^{1/4}$$

$$\text{time}, \; \tau = \left[\frac{\nu}{\epsilon}\right]^{1/2}$$

$$\text{frequency}, \; f = \left[\frac{\epsilon}{\nu}\right]^{1/2}$$

v and ℓ are estimates of typical velocity and length sacle of the (outer) flow. The response time of a 40 diameter neutrally buoyant particle is included in the table for comparison. Note that for the most inten turbulence (Case 2), some small scale structure is likely to be smoothed out.

In the rotational response calculation, the treatment is fully analogous. Following Chwang and Wu (19⁻ torque on a spherical particle rotating at angular velocity $\overline{\Omega}$ in a fluid of vorticity $\overline{\omega}$ is

$$8\pi \, \rho_f \, \nu a^3 (\overline{\Omega} - \frac{1}{2}\overline{\omega}) \; .$$

As stated in Subsection 2.1 above, the steady state is achieved when $\overline{\Omega} = \dfrac{\overline{\omega}}{2}$. The equation of motion t particle is

$$15 \, \frac{\rho_f}{\rho_p} \, \frac{\nu}{a^2} \left[\overline{\Omega} - \frac{1}{2}\overline{\omega}\right] = \overrightarrow{\dot{\Omega}} \; .$$

Again, using Fourier analysis, a similar spectrum is obtained for particle/fluid relative angular velocities the same conditions stated in the translational discussion above. τ_r, the rotational relaxation time, is obt from the rotational analog of the Stokes drag.

$$\tau_r = \frac{1}{15} \, \frac{a^2}{\nu} \frac{\rho_p}{\rho_f} \; .$$

Note that a particle's rotational response time is approximately five times faster than its translational res time.

The role of the local rate-of-strain tensor is more subtle. By symmetry, it can generate no couple on a spherical particle which would tend to rotate the particle. Non-spherical particles, on the other hand, will tend to align their long axes with the principal strain rate in the flow. In a simple shear, the sum of a straining field and a rigid body rotation, the rotation rate of elongated particles will modulate in proportion to their degree anisotropy as they tumble. (Jeffrey, 1922; see Subsection 2.4.4). If the strain rate becomes sufficiently great to appreciably deform non-solid probe particles, the effect of the strain rate on the measured vorticity is not negligible. This is considered in the next section.

2.4.2 Intrinsic Particle Behavior

Rigid body rotation is by definition the only behavior that solid particles in a shear flow can exhibit under normal conditions. However, liquid and visco-elastic droplets interacting with the surrounding flowfield will, in general, exhibit internal circulation and/or deformations in addition to their translations and rotations. Such deformations can be catastrophic, breaking particles or droplets into two or more parts. Fortunately, these effects become problematic only at very high strain rates.

For an immiscible fluid, surface tension is able to maintain sphericity of small (~ 25 μm) droplets against very high shear rates. For a 40 μm diameter droplet with 20 dynes/cm surface tension with the surrounding fluid dynamics pressure fluctuation must approach $\frac{\gamma}{a} \sim 10^4$ dynes/cm to deform the droplet significantly.

Apparently then, liquid droplets containing VOP mirrors will also function as vorticity probe particles. The most significant effect on the measured vorticity within the droplet results from the internal circulation induced by relative velocity when the droplet phase is not neutrally buoyant. A detailed discussion of liquid droplet VOP particle characteristics is beyond the scope of this report, but there are many interesting implications for two phase flow studies using variations of the VOP technique.

In the case of visco-elastic probe particles, strain-induced deformations can also lead to spurious modul. the measured local vorticity. For high shear rates, S, the magnitudes of both the vorticity and rate-of-s tensor will be large. So long as the particle remains spherical, the instantaneous rotation rate remains :

If particles are deformed, the rate-of-strain tensor generates a torque. Figure 6 indicates the anticipate. deformations under extreme conditions. In a worst case scenario, e.g., the shear rate near the leading flat plate in a water tunnel with free-stream velocity 30 ft/s, shear rates can exceed 10^5 s^{-1}.

For 100 μm diameter particles in water with $\{S, a, \nu\}$ = $\{10^5$ s^{-1}, 5 x 10^{-3} cm, 0.01 cm^2/s$\}$, the Reν number of the flow in the vicinity of the particle can be estimated as

$$R = \frac{a^2 S}{\nu} \sim 250 .$$

It is expected that such a flow will be nearly potential a short distance from the particle and that the eft viscosity will be confined to a boundary layer near its surface of thickness δ,

$$\delta \sim \sqrt{\frac{\nu}{S}} \sim 5 \times 10^{-4} \text{ cm} .$$

The maximum viscous stress experienced at the particle surface is

$$\tau \leq \rho \sqrt{\nu S^3 a^2} \sim 10^4 \text{ dynes/cm} .$$

8-6938
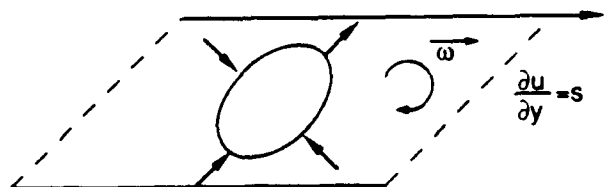
Figure 6

Deformation of Visco-elastic Particle at High Shear

24

The maximum attainable dynamic pressure forces relative to stagnation points in the particle frame are

$$\Delta p \sim \rho(sa)^2 \sim 10^5 \text{ dynes/cm}^2 \ .$$

For visco-elastic material, such as acrylamide gel (described in Chapter 4) whose bulk modulus is

$\geq 10^6$ dynes/cm^2, strains of less than 10 percent are the worst case. This corresponds to only a few percent

vorticity modulation. The yield strain of this material is 30 to 40 percent, i.e., larger deformations simply

rupture the gel network.

2.4.4 Particle Interactions

The Einstein relation for the bulk viscosity of a suspension of rigid spherical particles, μ^*, is

$$\mu^* = \mu \left(1 + \frac{5}{2}\alpha \right)$$

where μ is the continuous phase viscosity, and α is the total volume fraction of the dispersed phase. This

expression is generally accepted to hold for $\alpha \leq 0.02$. For particles of radius a, this condition on α can be

expressed geometrically with an average "primitive cell" of side r.

In each vertex of the cube is a single octant of the sphere, thus each cell contains the volume of a single sphere.

The volume fraction is $\alpha = \frac{4}{3}\pi \frac{a^3}{r^3}$, and when α is 0.02, r/a = 6. If the mean distance between particle

centers is less than 6a, the Einstein formula is no longer an adequate description. This expression is based upon

the approximation of single, independent particles perturbing an unbounded flow. Higher order terms describe

the flow field perturbations near a particle due to its nearest neighbors (Batchelor and Green, 1972b), as in

$$\mu^* = \mu \left(1 + \frac{5}{2}\alpha + C_2\alpha^2 + \ldots \right)$$

Special corrections may be required for particular flows. For example, Lin, Peery, and Schowalter (1970) have

shown that bulk viscosity of a shear flow with solid spherical particles require a correction for inertial effects at

high shear Reynold number, R_s:

$$\mu^* = \mu\left[1 + \alpha\left(\frac{5}{2} - R_s^{3/2}\right)\right] \quad , \quad R_s = \frac{a^2 S}{\nu}$$

Following Batchelor (1967), the far-field correction due to the presence of a rigid spherical particle emt a pure straining motion.

$$u'_i = \frac{1}{2} c e_{ij} \frac{x_i x_j x_k}{r^5} + O(r^{-4}) \quad , \quad c = 5a^3 \quad .$$

For a plane strain, i.e.

$$\frac{\partial u}{\partial x} = \beta \qquad \frac{\partial v}{\partial y} = -\beta$$

the far-field velocity perturbation in the plane, $z = 0$, is

$$\frac{5}{2}[\beta x \hat{x} - \beta y \hat{y}]\frac{a^3}{r^3}$$

where $[\beta x \hat{x} - \beta y \hat{y}]$ is the unperturbed straining fields at the point (x,y). The $r/a = 6$ criterion is seen equivalent to the requirement that the average velocity perturbation at neighboring particle not exceed ~ 1 percent of the background flow.

For 40 μm diameter particles, the $r/a = 6$ condition gives a particle number density, $n \lesssim 6 \times 10^5$ particles/cm^3 and an increase in bulk viscosity of 5 percent. Particle centers have > 120 μm avera separation; this degree of VOP particle loading is never likely to be exceeded. We thus have reasonabl assurance that dilute suspensions of probe particles sample the background flowfield and not the flow fi their neighbors. Under some conditions flow conditions, however, particle pair interactions can be imp

Isolated strong particle interactions, which perturb the particles' rotation rate, will occur in shear flows particles approach each other closely. A particle pair in a shear flow is shown below in Figure 7 in the reference frame of particle B. Particle A approaches particle B with velocity ωb where b is an effectiv parameter. As b becomes small ($< a$), the particle interaction is pictured sequentially in Figure 8 (e.g.

26
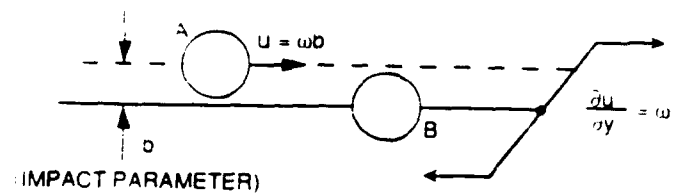
Figure 7

Particle A Approaches Particle B in the Uniform Shear at
Impact Parameter b with Velocity ω_b
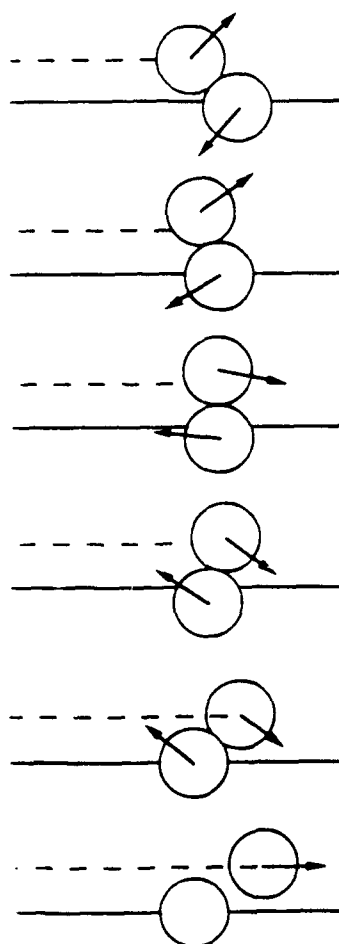
Figure 8

Sequence of Pair Positions During Interaction

Darabaner and Mason, 1967). At closest approach, at or near contact, the particle pair rotate as a rigid i.e., as a dumbell. Rather than each particle rotating at angular velocity $\omega/2$, the formula for the rigid b rotation rate of an ellipsoid of revolution with a 2:1 aspect ratio due to Jeffrey, applies approximately fo paired particles.

$$\Omega_p = \frac{4}{5}\,\omega\,\left[1 + 3\,\sin^2\,\frac{2}{5}\omega t\right]^{-1}$$

with bounds,

$$\frac{2}{5}\Omega < \Omega_p < \frac{8}{5}\Omega \quad . \quad \left(\Omega = \frac{\omega}{2}\right)$$

When the particles touch, they quickly accelerate through $8/5\Omega$, pass through Ω near vertical, and slow t as they approach alignment with the principal strain axis. Then they separate once again and continue o original paths. For small b, the probability of such an encounter is small since the velocity of approach off directly with b. The mean time between such interactions is then proportional to n/b, where n is the number density. For $b \geq d$, the particle diameter, stokes flow interactions drop off quickly, as $(b/d)^3$. the weakest attraction between particles, however, may result in a meta-stable pair which can persist for rotation periods in a laminar shear. This effect is observed experimentally, and must be invoked to exp laminar flow calibration data in Chapter 4.

Particles will also interact with solid boundaries. Some range restrictions (h/a = distance to wall/radius Failing these, the possibility of lift and/or induction effects which can induce body forces or torques on probe particle is introduced. The exact solution of the Stokes equations for the motion of a neutrally b sphere in a shear flow near a plane boundary has been calculated as a function of h/a by Lin, Lee, and : (1970). The calculated particle motion for local unperturbed shear rate ω_0 and velocity $U_0 = \omega_0 h$ for sei h/a values gives

Apparently the particle must come very close to the wall (a fraction of a micron for 100 μm particles) in to significantly reduce the measured vorticity. The reduced velocity of the particle must also locally per

28

$$\text{at } h/a = 10, \quad \frac{\Omega}{\frac{1}{2}\omega_o} = 0.9997, \quad \frac{U}{\omega_o h} = 0.9996$$

$$\text{at } h/a = 1.5, \quad \frac{\Omega}{\frac{1}{2}\omega_o} = 0.923, \quad \frac{U}{\omega_c h} = 0.921$$

$$\text{and at } h/a = 1.005, \quad \frac{\Omega}{\frac{1}{2}\omega_o} = 0.436, \quad \frac{U}{\omega_o h} = 0.495$$

boundary layer flow in this case. Still, corrections of vorticity statistics very near boundaries are not likely to be required.

3. THREE COMPONENT VORTICITY MEASUREMENT SYSTEM

The VOP apparatus is a fully automated system which acquires reflection trajectory data in real time from

small sampled volume at any point in the flowfield. These data are sequences of discrete, random event

consisting of a digitized representation of a reflection trajectory traversing the detector surface, from wh

vorticity vectors are deduced. The heart of the three-component VOP is the dual-axis position-sensing

photodiode detector. This is described in Subsection 3.1, along with the imaging and data acquisition sy

A detailed account of signal processing and data reduction procedures is provided in Subsection 3.2, foll

Subsection 3.3 by a discussion of error recognition routines for 'perturbed' or irregular trajectories and/

trajectory fragments. Lastly, a summary of system characteristics in Subsection 3.4 gives the dependenc

important system performance measures on key experimental parameters.

3.1 Three Component Detection System

The detection system of the VOP consists of three features: the detector which generates electrical sign

based on incident trajectories; the optical system which serves to define the sample volume and blocks

extraneous background light; and the data acquisition system which digitizes and stores the raw trajector

for post-processing with a personal computer. Each of these is discussed in turn below. The entire data

processing program is included as Appendix A.

3.1.1 Position-Sensing Photodiode

The dual axis position-sensing photodiode (PSD) employed in the VOP system, manufactured by United

Detector Technology, Inc., generates analog signals from which the instantaneous position (X,Z) and the

of the reflected beam are derived. The PIN SC-25 PSD device is an approximately two centimeter squa

biased photo-conductive layer over a uniform resistivity substrate. The axes are defined by four posts o

periphery of the active area, at $\pm Z_p$ and at $\pm X_p$. Current drains through the posts in proportion to th

power of light striking the surface. Because the substrate has uniform resistivity, it behaves as a two

dimensional voltage divider for a light beam striking the surface at a particular position. Thus, while th

30

of the currents draining through post-pairs is proportional to the power of the incident light (X-sum, Z-sum $\propto$ I), the difference of the currents is proportional to both the position of the centroid of the reflected beam and its power, for each axis (X-difference $\propto$ X·I, Z-difference $\propto$ Z·I). The quotient of the X,Z-difference signal and the X,Z-sum signal is therefore directly proportional to the X,Z-position of the reflection, independent of the power. The quantity (X-sum + Z-sum), however, is proportional to the incident power alone, independent of position.

The detector has a nominal sensitivity of 0.6 amps/watt and an NEP figure of $\sim 10^{-11}$ watt/$\sqrt{Hz}$, which varies somewhat with wavelength. The band width of the transimpedence pre-amplifiers is approximately 50 kHz at a gain of 10^6 V/amp; thus, the total noise of the detector is approximately 1 mV (at room temperature). A reflected power of just a few microwatts is sufficient to give a signal-to-noise ratio (SNR) of about 100 in the sum voltage signals. The junction capacitance of the detector will allow speeds approaching 1 MHz, which can be exploited in the future with faster pre-amplifiers. The detector and its sum and difference pre-amps are housed together in a single shielded unit.

The reproducibility of position measurements on the detector is generally excellent, but is dependent upon the signal-to-noise ratio. The physical position of the centroid, however, is not linear in the position deduced from the output of the detector, particularly near the edges of the active area. A detailed detector calibration must be performed and implemented in the data reduction procedure.

3.1.2 Optical Configuration

A typical optical configuration is shown in Figure 9. While a number of variations are possible, this arrangement used to view the near wall vorticity structure of Taylor-Couette instabilities, is illustrative of all the important features.

Beginning from the incident beam from within the fluid, the optical elements are described in their order along the optical path. The first optically active surface encountered in this geometry is the outer flow boundary.

INCIDENT BEAM

REFRACTIVE INDEX
MATCHED PRISM

OUTPUT
COUPLER

F1 4 50 mm
· COLLECTOR

IMAGING LENSES

F2.8 100 mm
· MAGNIFICATION
OF IMAGE: 2X

DIFFUSER FOR VIEWING
IMAGE PLANE (OR PSD
MEASURING VELOCITY)

VORTICITY PROBE
PARTICLES IN
FLOWFIELD

REFLEX MIRROR
(OR BEAMSPLITTER)

VARIABLE
SLIT DEFINES
SAMPLE
VOLUME

AUTOCOLLIMATOR
LENS FOR
VELOCITY
COMPENSATION

POSITION SENSING
PHOTODIODE
PSD MEASURES
POSITION AND
INTENSITY OF
REFLECTIONS

Figure 9

8-5778

VOP Optical System

Under some conditions, the wall material should be refractive index matched to the working fluid. This
desirable when working close to the wall at 45 deg, as in the configuration of Figure 9, since both stron
reflections and astigmatism compromise the image quality. In the case of water as the working fluid, th
been accomplished by means of a molded window section of fluorinated acrylic plastic, which forms par
boundary.

The second optical element is the coupling prism. Together with the index-matched boundary window s
they provide unrefracted entry of the incident beam and astigmatism-free imaging of the sampled volume
prism is custom-made from either Plexiglas or acrylamide gel (see Subsection 4.2.2).

32

Next is the plano-convex output coupling lens -- so-called because of its function of allowing rays to leave the prism and emerge from the lens surface without refraction; the large solid-angle requirements of the three-component VOP necessitate this as a means of eliminating both the angular magnification and spherical aberration induced by planar surfaces. For fully indexed matched components, the center of curvature of the output coupler's convex surface coincides with the position of the sampled volume in the fluid, which clearly illustrates the output coupler's function.

The imaging component consists of two lenses. The collimating (collecting) first stage is a Nikon F1.4 55 mm camera lens (inverted). The second stage is a Nikon F2.8 110 mm camera lens which provides 2X-magnification of the sampled volume at the image plane. Note that the angular magnification, however, for rays leaving the sampled volume, is 0.5X.

These lenses were chosen to afford maximum acceptance angle with minimum spherical aberration. At less than F2, it is usually necessary to resort to multi-element optics to improve image quality beyond what is commercially available from precision achromatic lenses. This was established in the laboratory having found aspheric pairs at F1.0 and achromat pairs at F1.6 unacceptable for imaging. The imaging quality concerns are made clear in considering the next optical stage.

Definition of the sampled volume is accomplished in two dimensions by the incident beam waist and in the third dimension by the variable slit mask in the image plane shown in the figure. For a 300 μm slit width, a point spread function width through the optical train of approximately 100 μm, for example, would result in more than 50 percent of the imaged area being compromised by optical aberrations. That is, all or part of the light is clipped by the slit edges in some complex way as a function of exit angle. Such difficulties are best avoided with high quality imaging available with camera lenses used in their proper mode (infinite conjugation ratio). Actual point spread functions have been indirectly measured for this system by observing the image of a point light source (~5 μm spot) passing through the slit mask at successively smaller slit widths. With the camera lenses the light continues to pass the slit mask with the full F1.5 down to 25 μm.

33

The final optical element is an auto-collimator also referred to as the velocity compensation lens. As this r implies, the function of this lens is to eliminate the effect of translational motion of the real image of the particle in the image plane. A lens of focal length f is placed at the distance f from image plane to lens principal plane, and also distance f from principal plane to the detector surface. The position of the light s on the detector is then determined solely by the angle at which the reflection exits the image plane. The av collimation principle is demonstrated by the illustrative construction in Figure 10. The determination of an velocity is not affected by particle translation within the sampled volume. The auto-collimator for this syst a 40 mm focal length, AR-coated F2.5 precision achromat.

Slit Mask in
Image Plane
greatly exaggerated)
Vertical Scale

Auto-collimator
Lens

Detector
Plane

Figure 10

B-6946
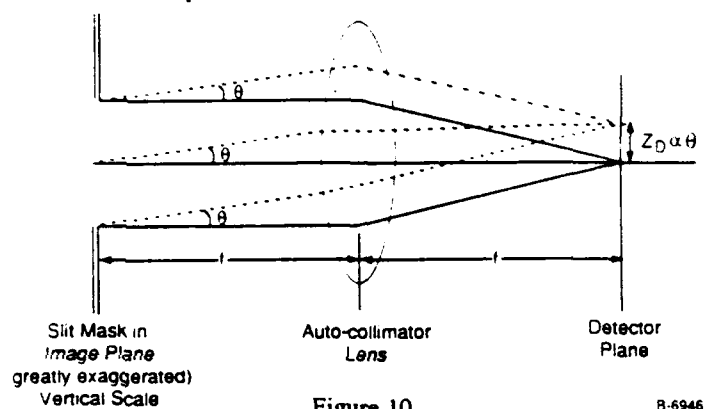
Auto-Collimator Function Illustrated. The position of the rays on the detector plane depend on exit angle θ only, not on position in the image plane

3.1.3 Data Acquisition

The four outputs of the PSD, the x-sum, x-difference, z-sum, and z-difference are acquired with a LeCroy digitizer module in a Camac crate. The four-channel 6810 has a 512 K word memory and a variable samp rate of up to 1M samples/s simultaneously on four channels. Each channel writes a minimum 1K block of 12-bit data at a uniform sampling interval for each trigger received. The trigger signal indicates the prese: a reflection on the detector surface and the level is set to exclude signals below a desired signal-to-noise r. Wrap-around buffers allow pre-triggering so that data is symmetrically acquired about the trigger point. memory is filled after writing only 128 records. Data acquisition must then cease until this data is transfe to computer disk via the Camac GPIB interface. This is sketched in Figure 11.

34

$A + {}^\prime B$ (SUM) α I (INCIDENT LIGHT INTENSITY)

$A - {}^\prime B$ (DIFF) α I · X_c (X_c = X CENTROID OF INCIDENT LIGHT)

$$X_c \; \alpha \; \frac{{}^\prime A - {}^\prime B}{{}^\prime A + {}^\prime B} \; = \; \frac{DIFF}{SUM}$$
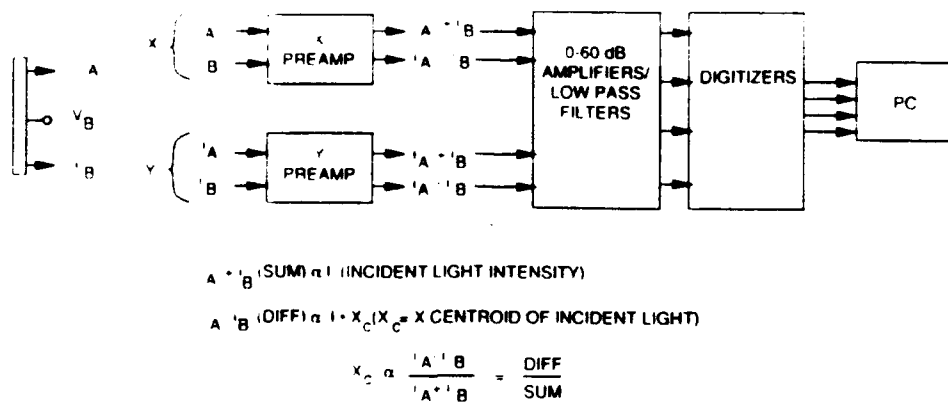
B 1544

Figure 11

Data Acquisition Path of the Three-Component VOP System.
This system has been used for development and testing purposes only

This data acquisition scheme is far from optimum. Custom-designed hardware in future VOP designs could lead to real-time acquisition and processing capability. However, for the purposes of instrument development the 6810 performed adequately and was easily incorporated into the development prototype VOP.

3.2 Data Reduction

Data reduction involves many separate operations which are listed in order below:

1) Background subtraction

2) Thresholding

3) Masking

4) Detector mapping corrections

5) Optical mapping corrections

6) Signal-to-noise ratio statistical weighing

7) Optimum differencing interval

8) Linear least-squares fitting procedure.

These steps are briefly described in the following paragraphs. After these steps have been performed, several diagnostics are used to evaluate the validity of the measurement; these are discussed in Subsection 3.3.

All of the data reduction and analysis has been performed on either a 286 or 386 PC throughout the Phase

program. Even some of those features which might be considered "signal processing" and suitable for har

implementation have been cast initially in software for convenience. For example, background subtraction

quotients, and thresholding have all been previously done with analog signal processors (Ferguson and We

1983). These were not used in the Phase II program, however, in order to accommodate the available dat

acquisition system.

3.2.1 Background Subtraction

Unfortunately, valid reflections are not the only source of light falling on the detector surface. The PSD

detector is not an imaging system but rather an averaging system, measuring the centroid of the light distr

over its surface. Several background sources and their relative importance can be identified in two catego

DC or slowly varying sources, and rapidly fluctuating sources (on the time scale of the trajectory passage)

the first category is direct or stray specular reflections from the incident beam which can potentially overw

the valid signal. Also, volume scattering (Rayleigh, fine impurities, and fluorescence of working fluids) f

the sampled volume, which is ordinarily orders of magnitude smaller than a valid reflection. The latter

contributions may grow relative to the reflection intensity for larger sampled volumes. In the second cate

are multiple valid reflections, i.e., more than one reflection on the detector at the same time giving overla

trajectories, and reflections or scattering from VOP particle surfaces or large particulate contaminants or

bubbles. The former are of the same order of brightness and violently perturb trajectories, while the latte

usually weak and affected trajectories often cannot be distinguished from "clean" trajectories.

The first category of background disturbance is easily remedied. Because it is constant or slowly varying,

(in time) background signals can be measured and subtracted from the sum and difference signals, e.g.,

$$X_{DIFF} = X_S I_S + X_B I_B \;, \quad X_{SUM} = I_S + I_S \;, \quad X_T = \frac{X_S I_S + X_B I_B}{I_S + I_B}$$

where X_T is the centroid of signal plus background, X_S is the desired x-position, and I_S the valid reflectic

optical power. and X_B and I_B are associated with the background. The background values can be estimated from the sum and difference baseline signals prior to the event so the correct values X_S, and I_S can be obtained. The actual background levels are measured by seeking the most probable digitized value in the individual 1024 point records. This is invariably the best baseline estimate.

The second category of disturbance is not fixable. Multiple reflection (coverlapping trajectory) events must be discarded. Weakly perturbed events must pass goodness-of-fit tests (see Subsection 3.3.1 below) to be accepted as good data.

3.2.2 Thresholding

Of the 1024 point record stored by the 6810 module, at most only a few hundred of the interior points represent actual trajectory data. Occasionally, multiple events occur within a single, recorded trace. The algorithm must decide where those events are located in the data stream and use the remainder for background corrections. This is often a more complex task than expected, particularly when the data is characterized by extreme intensity fluctuations. Also, some data sets are characterized by rapidly rising and falling edges whereas the opposite is frequently true for equally valid events. The goal of the thresholding algorithm is to keep the maximum amount of valid trajectory without introducing artifacts or unnecessarily clipping or chopping trajectories.

When the light power exceeds a preset threshold, the x and z-positions are calculated (from the quotients of the digitized difference and sum signals). The thresholding algorithm currently in use compares an absolute threshold value with a running n-point smooth on the sum of the digitized X-sum and Z-sum signals (the total incident power) with variable hysteresis. The value of n is chosen sufficiently large for each data set to give adequate smoothing. This algorithm eliminates rapid on-off threshold flags due to noise near the selected threshold voltage, and suppresses the possibility of splitting a single trajectory into multiple parts due to large light level excursions. It has the virtue of approximating a band-limited Schmidt trigger with hysteresis and thus corresponds to a hardware-implementable feature.

37

3.2.3 Masking

From the discussion in Subsection 2.4.4, one consequence of the finite diffraction angle from the lead carb
platelets is that reflections have a finite dimension on the detector face. Frequently, the threshold voltage
exceeded before the (Airy disc) reflection is fully on the active area. This clearly gives a false centroid va.
An effective solution is simply to restrict the position values that a valid trajectory can take on, by means
software mask. A band around the perimeter of the detector active area, which is within an average reflec
diameter of the detector edge, is likely to suffer the edge effect. All measured positions within this band r
are disallowed as possible trajectory coordinates. This is implemented in software, just as is the threshold

3.2.4 Detector Mapping Correction

Detector non-linearity becomes quite serious near the detector edges amounting to nearly 20 percent depart
from linearity in the worst case. Detector masking helps somewhat, but since measurements are extremely
sensitive to trajectory curvature, trajectory endpoints have the greatest weight in these measurements. Car
detector calibration, to ensure that measured reflection coordinates correspond precisely to true reflection
coordinates, is unavoidable. Figure 12 is a point-by-point (20 x 20) calibration of the particular PSD dete
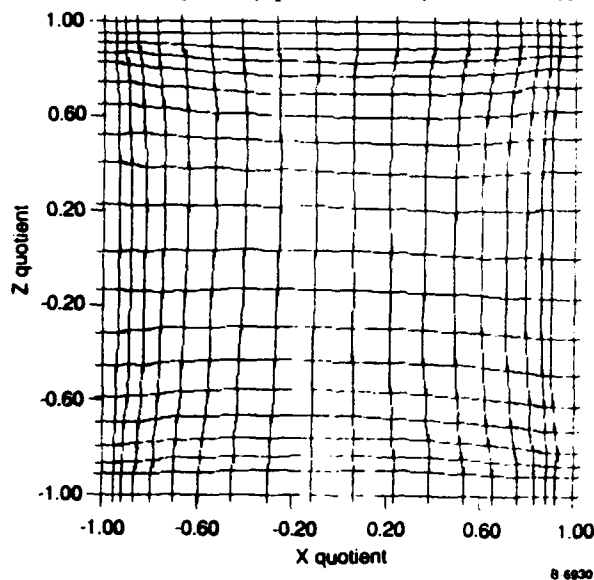
Figure 12

UDT Detector Calibration Map X-Quotient Versus Z-Quotient.
Lines are 1 mm apart in physical space

(CDT PIN SC-25) used in this program, showing lines of real physical position at 1 mm separation on a detector output grid square. The calibration was done manually by traversing a HeNe laser beam across the detector with the precision translation stage. Using this map, the data reduction program currently performs an interpolation on the non-orthogonal grid to find true position coordinates.

3.2.5 Optical Calibration

Calibration of the optical components (the imaging lenses and the auto-collimator) was performed using a HeNe laser and a 60X microscope objective as a source at the nominal sampled volume position. This reasonably approximated a point-source and filled the aperture of the 55 mm collector lens. A fine reticle with a square grid was placed perpendicular to the optic axis so that its shadow also filled the aperture. The optical system was properly focused and 35 mm film was positioned at the detector plane and exposed. One such photo is included as Figure 13. The axi-symmetrically distorted grid image was manually digitized and fit to a single
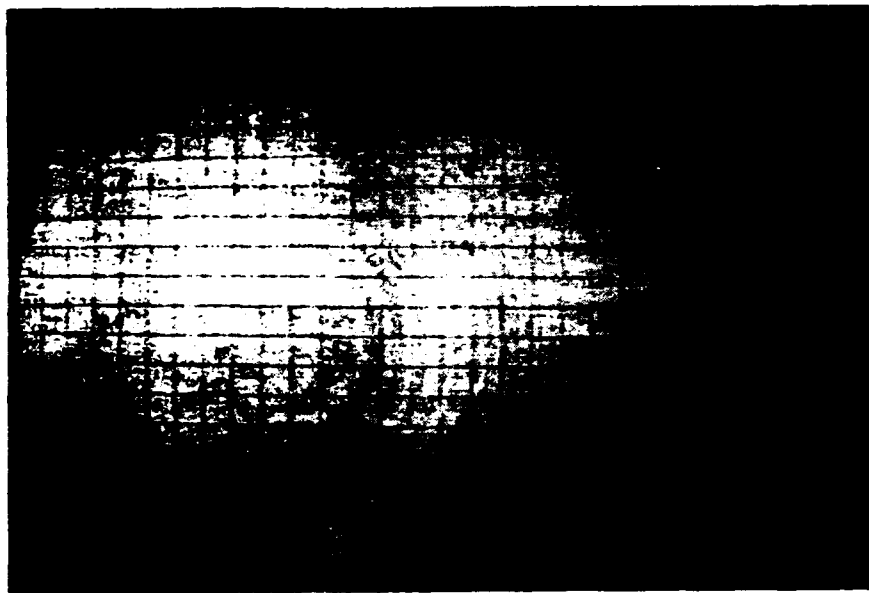
V-501

Figure 13

Optical Calibration. The shadow of a square grid passing through the optical element
provides a map of optical distortion

39

parameter equation in r, the distance from the optic axis in the detector plane. Based on the assumption that simple field curvature caused the distortion, the best fit was given by,

$$r_{actual} = 1.284 \, \sin^{-1}\left[\frac{r_{detector}}{1.284}\right] \quad .$$

This correction effectively flattens the field. Figure 14 is a typical digitized trajectory for which all of th preceding corrections have been made (Subsections 3.2.1 through 3.2.5).
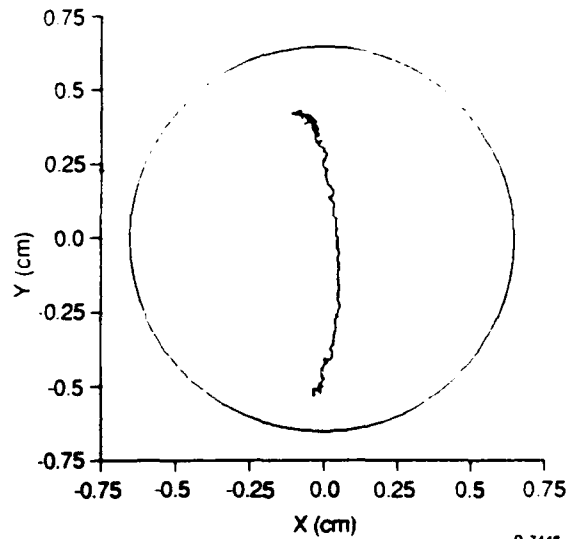
Figure 14

Digitized Representation of a Corrected Trajectory

3.2.6 Signal-to-Noise Statistical Weights

As mentioned in Subsection 3.2.3, light level excursions can be quite extreme. It is not unusual to find variation of more than an order of magnitude over a data set. Since the noise power is fixed at given gas variations in signal-to-noise ratio (SNR) are correspondingly large. (The calculation of the SNR random variable, and estimates of its distribution versus system parameters are given in Appendix B.) Clearly, n data points should be equally weighted in the fitting routine. Their proper statistical weights are $\left[\frac{1}{\sigma_{\dot{\theta}'_i}}\right]^2$ and $\left[\frac{1}{\sigma_{\dot{\phi}'_i}}\right]^2$ corresponding to the dependent variables $\dot{\theta}'_i$ and $\dot{\phi}'_i$. Propagating the errors detector signals through the computation of $\dot{\theta}'$ and $\dot{\phi}'$ and gives

40

$$\sigma_{\theta'} \approx \frac{D}{2} \frac{\sqrt{1 + z^2}}{SNR \cdot \Delta t \cdot y_d} \qquad \sigma_{\phi'} \approx \frac{D}{2} \frac{\sqrt{1 + x^2}}{SNR \cdot \Delta t \cdot y_d} \qquad (8)$$

where Δt is the sampling interval, y_d is the y distance from the imaged sampled volume to the detector plane, and D is the diameter of the detector active area. Henceforward, all distances on the detector surface are normalized by y_d, with the system F-number $y_d/D \sim 1$. Lengths are thus equivalent to angles on the unit sphere.

By accounting for the true instrumental noise, the X_ν^2 goodness-of-fit parameter described in Subsection 3.3.1 below, takes on useful physical meaning and is used to evaluate how well the trajectory equations and a single vorticity vector represent a trajectory at any instrumental noise level. Uncertainties in the vorticity components properly reflect both the instrumental noise and the fit quality.

3.2.7 Optimum Differencing Interval

Consider an arbitrary trajectory traversing the detector with a given constant vorticity. In general, it will display some local rate of passage on the detector, $\dot{r}$, and some angle of inclination, ψ, with respect to the detector plane coordinate axes (x,z), as well as some finite curvature $\frac{\partial \psi}{\partial r}$. Indeed, recalling the discussion of Subsection 2.3.2, the measurement of $\dot{r}$, ψ, and $\frac{\partial \psi}{\partial r}$ represent a natural geometrical basis for the description of ω'_x, ω'_z, and ω'_y. For a trajectory traversing the entire detector surface (~ 1 radian), sampled at uniform intervals, Δt, the number of sampled points in the digitized record can be estimated by $N \sim \left[\frac{1}{\bar{\dot{r}} \Delta t} \right]$. To measure the mean value of $\dot{r}$, denoted $\bar{\dot{r}}$, over the entire trajectory with the maximum achievable precision, the optimum differencing interval Δt_{opt}, on which the time derivatives are based, must be selected.

The Taylor expansion in time of the trajectory coordinate r about r_0 is

$$\frac{\bar{r} - \bar{r}_0}{\Delta t} \approx \vec{\dot{r}}_0 + \frac{1}{2} \vec{\ddot{r}}_0 \Delta t \quad .$$

41

But to first order. the uncertainties in $\dot{r}$ and $\bar{\dot{r}}$, denoted $\delta\dot{r}$ and $\delta\bar{\dot{r}}$, estimated from Eq. (8), are given by

$$\delta\dot{r} = \frac{\alpha}{SNR\cdot\Delta t} \quad , \quad \delta\bar{\dot{r}} \sim \frac{\delta\dot{r}}{\sqrt{N}}$$

where α is a constant of order unity. Thus, with the estimate of N above

$$\delta\bar{\dot{r}} \propto \frac{1}{\sqrt{\Delta t}} \quad .$$

Clearly as $\Delta t\rightarrow 0$, the loss in precision in $\bar{\dot{r}}$ is more rapid with decreasing Δt than the corresponding incre
the number of measurements, N, can offset, and $\delta\bar{\dot{r}}$ grows. On the other hand, if the intervals become t
great, errors due to second order (acceleration) terms in the expansion begin to appear as estimates of the
derivatives become increasingly poor. The optimum differencing interval is defined as that for which the
sources of error are comparable in magnitude:

$$\delta\dot{r} \sim \frac{\alpha}{SNR\cdot\Delta t_{opt}} \approx |\ddot{r}|\Delta t_{opt}$$

where $\ddot{r}$, a measure of local acceleration on the trajectory, is order $\partial\frac{\psi}{\partial}\dot{r}^{-2} \cdot \frac{\partial\psi}{\partial r}$ for a typical trajectory i
order unity, so Eq. (9) gives an optimum differencing interval, Δt_{opt},

$$\Delta t_{opt} \sim \frac{1}{\ddot{r}\sqrt{SNR}}$$

or the number of intervals for a full trajectory, n_{opt}

$$n_{opt} \sim \sqrt{SNR}$$

and therefore, from Eqs. (9) and (10),

$$\delta\bar{\dot{r}} \approx \frac{\alpha\bar{\ddot{r}}}{\sqrt{SNR}\sqrt{N}} \quad .$$

This analysis can be extended to $\bar{\psi}$, and $\frac{\partial\bar{\psi}}{\partial r}$, and include partial trajectories as described in Appendix C

In terms of the data reduction algorithm, precision is considerably improved when derivatives are computed over m-point intervals where $\Delta t_{opt} = m\Delta t$, e.g.,

$$\dot{\theta}'_1 = \frac{\theta_{m+1} - \theta_1}{m\Delta t} , \quad \dot{\theta}'_2 = \frac{\theta_{m+2} - \theta_2}{m\Delta t} , \quad \cdots .$$

This approach will not yield as great a precision in $\overline{\omega}$, or be as statistically sensitive to goodness-of-fit tests, as non-linear regression directly on trajectories, but it is computationally many times faster.

3.2.8 Linear Least-Squares Fitting Procedure

The least-squares fit of the data to the differential trajectory equations (DTEs) is conventional. The three vorticity components are obtained through the accumulation of appropriate sums and 3 x 3 matrix inversion, a simple extension of standard linear least-squares methods. The linear DTEs can be written

$$\dot{\theta}' = \overline{\alpha} \cdot \overline{\omega} , \quad \dot{\phi}' = \overline{\beta} \cdot \overline{\omega}$$

and χ^2 is therefore

$$\chi^2 = \sum_\ell \left[\frac{\dot{\theta}'_\ell - \alpha_{\ell k}\omega_k}{\sigma_{\theta_\ell}} \right]^2 + \left[\frac{\dot{\phi}'_\ell - \beta_{\ell k}\omega_k}{\sigma_{\phi_\ell}} \right]^2 .$$

The linear least-squares technique determines the $\overline{\omega}$ which minimizes χ^2, i.e.,

$$\frac{\partial \chi^2}{\partial \omega_i} = \sum_\ell^N \left[\frac{\alpha_{\ell_i}\left(\dot{\theta}'_\ell - \alpha_{\ell k}\omega_k\right)}{\sigma_{\theta_\ell}^2} + \frac{\beta_{\ell_i}\left(\dot{\phi}'_\ell - \beta_{\ell k}\omega_k\right)}{\sigma_{\phi_\ell}^2} \right] = 0$$

or, dropping the ℓ index ($= 1,\ldots N$) with the understanding that weighted summation is implied

$$\left(\alpha_i\dot{\theta}' + \alpha_i\dot{\phi}'\right) = \left[\alpha_i\alpha_k + \beta_i\beta_k\right]\omega_k , \quad (i,k=1,2,3) .$$

43

The solution is provided by inverting the curvature matrix, $[c_{ik}] = [\alpha_i\alpha_k + \beta_i\beta_k]$

$$\omega_k = [\alpha_i\alpha_k + \beta_i\beta_k]^{-1}(\alpha_i\dot{\theta}' + \beta_i\dot{\phi}')$$

Uncertainties are estimated from the elements of the curvature matrix.

3.3 Error Recognition and Rejection

Some of the trajectories collected by the VOP system will be contaminated or rendered useless by one or of the following effects:

1) Trajectory overlap.

   Two or more reflections on a detector render these events uninterpretable. The probability of tr overlap is data rate dependent (see Subsection 3.4.3, below).

2) Detector edge effects.

   Large reflection divergence angles often attributable to multiple-mirror clusters within particles, spurious reflection coordinates and speeds while the reflection is moving onto the detector active Detector masking accounts for most, but not all of these events.

3) Non-spherical particles.

   Malformed or clustered particles cause modulation of the particle rotation rate relative to the lo vorticity. (It is possible to sample the rotation of such a particle when $\partial\Omega/\partial t$ is large. This situ difficult to distinguish from a true, local angular acceleration, $\partial\omega/\partial t$, due to turbulent flow fluctuations.)

4) Trajectory fragments.

   Under some conditions, fragments which are too small to provide reliable information on traject curvature and accelerations, couple the uncertainty in ω'_y strongly into ω'_x and ω'_z. This is rel

5) The zero vorticity problem.

   A stationary reflection on the detector can arise in the case of zero vorticity, a finite vorticity v parallel to the mirror-normal vector, or diffuse reflection from a contaminant particle.

44

Trajectories suffering from any of the above complications are referred to as irregular trajectories. Some strategies designed to identify such errors and reject correct or flawed trajectories are discussed below.

3.3.1 The χ_ν^2 Statistic

The basis of least-squares fitting algorithms is the minimization of the χ^2 statistic, whether by linear or non-linear regression. The χ^2 variable is defined as

$$\chi^2 = Z_1^2 + Z_2^2 + \ldots + Z_n^2$$

where Z_i are independent random variables normally distributed with zero mean and unit variance (Bendat & Piersol, 1971). In the context of curve fitting, such a variable is usually constructed from the measured dependent variable, y_i, the known variance of its Gaussian noise, σ_i, and the assumed functional form for $y(x,\ldots,\{p\})$, evaluated at the independent control variable(s), $x,\ldots$. We obtain

$$Z_i = \frac{\left(y_i - y(x_i,\ldots)\right)^2}{\sigma_i^2}$$

or

$$\chi^2 = \sum_{i=1}^{n} \frac{\left(y_i - y(x_i,\ldots)\right)^2}{\sigma_i^2} \quad .$$

The best fit is defined as the set of parameters $\{p\}$ in $y(x_i,\ldots,\{p\})$ which result in the minimum attainable χ^2. The number of degrees of freedom for a fit with p independent parameters is $\nu = n-p$ and the expected value of χ_ν^2 is

$$\chi_\nu^2 = \frac{\chi^2}{\nu} \sim 1 \quad .$$

when the variances σ_i^2 have been correctly estimated, and when the deviation from $y(x_i,\ldots,\{p\})$ is attributable entirely to noise. If the former condition is met, increases in χ_ν^2 are assumed to arise from systematic deviation of the measured values from the fitted expression. This is the basis of goodness-of-fit tests. A large χ_ν^2 value, i.e., $\chi^2 >> 1$, is a strong indication of a poor fit to the data because the function $y(x_i,\ldots\{p\})$ cannot describe the data for any parameter values.

45

Unfortunately, χ_ν^2 is not an absolute test of the adequacy of the fitting function. The distribution of sig noise ratios of trajectories in a data set can be broad. Identical trajectories, each containing the same ob detect, are represented in Figure 15. Figure 15(a) possesses a large SNR whereas Figure 15(b) has a lo and instrumental position noise is comparable in variance to the deviations from the true trajectory. (Suc error might be due to a second reflection striking the detector while the first is traversing the detector. cases, the centroid of the pattern is strongly deflected from a legitimate or regular trajectory shape.) In case, the best fit curve shown as the solid line, is likely to be very similar. On the other hand, if χ_ν^2 is partitioned into the contributions from systematic deviations, Δ, from the fitted curve and those due to r noise $\sigma_A \propto \dfrac{1}{SNR_A}$ and $\sigma_B \propto \dfrac{1}{SNR_B}$ in Figures 15(a) and 15(b), respectively, then

$$\chi_\nu^2 \sim \frac{\Delta^2 + \sigma^2}{\sigma^2}$$
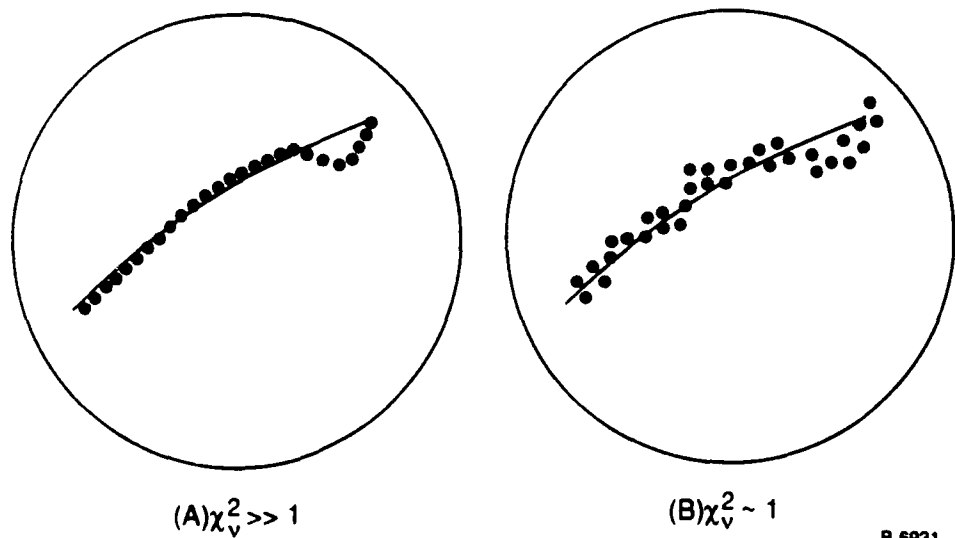
$(A)\chi_\nu^2 \gg 1$ $(B)\chi_\nu^2 \sim 1$

B-6931

Figure 15

Trajectories (points) and Fits Illustrating the Relative Sensitivity of the χ_ν^2
Goodness-of-Fit Statistic to Systematic Deviations

46

But, from the discussion above, $\sigma_A \ll \bar{\Delta}$ and $\sigma_B \approx \bar{\Delta}$, therefore

$$\chi^2_{\nu A} = 1 + \frac{\bar{\Delta}^2}{\sigma_A^2} \gg 1 \quad , \quad \chi^2_{\nu B} = 1 + \frac{\bar{\Delta}^2}{\sigma_B^2} \approx 2 \quad .$$

χ_ν^2 can be quite insensitive as a goodness-of-fit parameter when the precision of the measurements is poor and parameter uncertainties are large.

This situation is exacerbated when fitting the differential trajectory equations. Noise magnification of the σ_A and σ_B values as a result of differentiation often eliminates the goodness-of-fit utility of the χ_ν^2 test entirely. In this case, an auxiliary approach is needed for trajectory evaluation.

3.3.2 Orthogonal Polynomial Decomposition

The differential trajectory equations (DTEs) describing a single reflection and constant vorticity can be fit to any measured trajectory. Not all measured trajectories, however, result from single reflections at constant vorticity. Irregular trajectories, those which could not have been produced by the equations or which are pathological (near the VOP singularity), must be identified and rejected. A fast algorithm is needed to quantify trajectory shapes and decide whether they belong to the subset of legitimate or regular trajectories which the DTEs can produce. Trajectories are described by $(\theta'(t_i), \phi'(t_i))$, the set of N angular coordinates of the reflection sampled at fixed time intervals, Δt. The θ' and ϕ' projections of each trajectory are easily fit to generalized orthogonal polynomials using a very efficient linear algorithm (Bevington, 1969).

Orthogonal polynomials are defined as a basis set of functions $P_n(t)$ on an interval $[t_1, t_2]$ such that an arbitrary function $\theta(t)$ can be expressed as

$$\theta(t) = \sum_n \alpha_n P_n(t) \text{ with } \alpha_n = \int_{t_1}^{t_2} P_n(t)\theta(t)dt \text{ and } \int_{t_1}^{t_2} P_n(t)P_m(t)dt = 0 \text{ for } n \neq m \quad .$$

In other words. the α_n are independently specified and do not affect the other α_m, $m \neq n$.   The polynoi

$$\theta'(t_i) = \alpha_0 + \alpha_1(t_i\text{-}t_1) + \alpha_2(t_i\text{-}t_2)^2 + \dots$$

$$\varphi'(t_i) = \beta_0 + \beta_1(t_i\text{-}t_1) + \beta_2(t_i\text{-}t_2)^2 + \dots$$

where the t_n depend only on the number of points, N, α_0 represents the mean θ' value, α_1 gives the 'av

slope. α_2 the average curvature and so on. Based upon the symmetries of the VOP geometry and trajeu

equations. polynomials up to the third order adequately span nearly all of the allowed trajectory space.

an arbitrary trajectory shape can be expressed as a vector in 8-dimensional vector space

$[\alpha_0,\alpha_1,\alpha_2,\alpha_3,\beta_0,\beta_1,\beta_2,\beta_3] = [\overline{\alpha},\overline{\beta}]$. $\chi_\nu^2 = \chi_{\theta'}^2 + \chi_{\phi'}^2$ are also generated. Some representative orthogc

polynomial decompositions (OPDs) are reproduced in Figure 16.

The figure gives the impression that the OPDs span a $[\overline{\alpha},\overline{\beta}]$ space that is much larger than that spanned

DTEs: Figure 16b is not a legitimate (regular) trajectory. To reject this trajectory, a (7-dimensional) t

could be found in $[\overline{\alpha},\overline{\beta}]$ within which trajectories are considered to be regular. However, with the assu

B-7
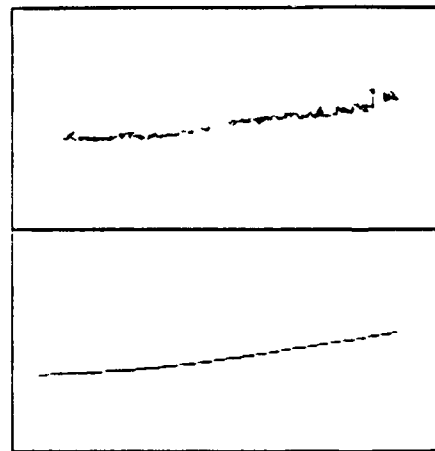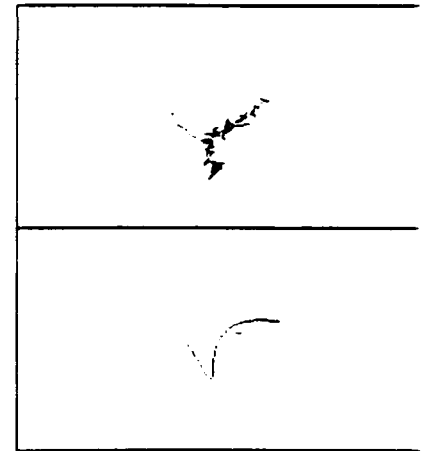
(a) Regular Trajectory   (b)   Irregular Trajectory
                                                        (i.e., not producible with the DTE

Figure 16

Some Representative Trajectories with their Orthogonal Polynomial Representations

48

that all regular trajectories are contained in $[\bar{\alpha}, \bar{\beta}]$, a trajectory that cannot be fit by the third order OPD is unlikely to be regular. It follows that the χ_ν^2 goodness-of-fit statistics for the OPD can be immediately employed to reject many irregular trajectories. These statistics, computed from trajectories directly rather than their time derivatives, are more sensitive tests of goodness-of-fit, as noted in the preceding section. The regular trajectory boundaries in $[\bar{\alpha}, \bar{\beta}]$ have not yet been fully explored.

A useful extension of the OPD χ_ν^2 test for edge effects is used routinely. For OPD χ_ν^2 values above a threshold, the trajectory is re-analyzed with a smaller detector area. An additional swath of 10 percent of the detector diameter around its perimeter is added to the software mask. If the OPD χ_ν^2 value drops below yet another threshold, the error is assumed to have been edge effect-related and this trajectory is analyzed over the new smaller detector area. Otherwise it is rejected.

3.3.3 Proximity Tests

The last two classes of problems noted above, trajectory fragments and zero vorticity, are closely related. The proximity tests are so-called since they monitor the proximity of the measured vorticity to the VOP singularity: $\bar{\omega}$ parallel to the mirror-normal vector. Both zero vorticity and the shortest trajectory fragments may suffer the effects of the VOP singularity, the former by virtue of actually being parallel to the mirror-normal, and the latter by spurious curvature estimates at finite SNR. The discussion of the actual implementation of these tests has been deferred to Appendix D. The parameters upon which these tests are based must first be introduced.

3.4 System Characteristics

The three-component VOP measurement, though simple in concept, involves a number of subtleties in analysis and interpretation which complicate the experimental technique in practice. In this respect the VOP technique is rather like Laser-Doppler Velocimetry (LDV) which suffers the effects of finite size sampled volumes, noise, sampling bias due to velocity fluctuation, etc. The VOP system measures a reflection from mirrors, log-normally distributed in diameter, moving in a fluctuating turbulent velocity field, passing through a gaussian

beam profile at random position. The reflection (and sometimes fluctuating background light) strikes the detector at a random initial (X,Z) position, for a time period (and trajectory size) dependent upon the v vector, the velocity vector, the position of the particle in the sampled volume, and the mirror diameter. of the independent random variables (less the number of relations correlating some of them) in the abov description is a convincing argument for care in analyzing and interpreting data. On the other hand, th also quite rich in information about the vorticity and velocity fields, and yields simple parameters which used to monitor instrumental precision.

The following subsections outline the necessary correction to raw vorticity component PDFs, as well as guidelines for interpreting the statistics obtained from these distributions. First, an analysis of the expec distribution at constant $\overline{\omega}$ is presented. This is the resolution function. Next, a correction for vorticity s non-uniformity due to both instrumental and flowfield parameters, called the sampling function, is descr This function accounts for vorticity variation at fixed instrumental resolution. A method for correcting vorticity PDFs using both the resolution and sampling functions is outlined. Lastly, issues relating to s and temporal resolution are considered.

3.4.1 Vorticity Resolution Function

The vorticity resolution function is defined as the distribution that would be obtained by measuring a vo δ-function. The width of this distribution is due entirely to instrumental noise, and it is this function th. convolved with measurement of fluctuating vorticity which must be accounted for:

$$R(\overline{\omega}_0) = \int_\omega R(\overline{\omega})\, \delta(\overline{\omega} - \overline{\omega}_0) d^3\overline{\omega}$$

and the measured PDFs:

$$P_{measured}(\overline{\omega}) = \int_\omega p(\overline{\omega'})\, R(\overline{\omega} - \overline{\omega'})\, d^3\overline{\omega'}$$

In general, the form of $R(\overline{\omega})$ will vary with $\overline{\omega}$, but it is not possible to measure a vorticity δ-function at every point in vorticity space in order to catalogue the behavior of $R(\overline{\omega})$. On the other hand, if the uncertainties in vorticity measurement and their distributions can be described as a function of $\overline{\omega}$ and relevant experimental parameters, then $R(\overline{\omega})$ can be directly calculated. In the following, separability of

$R(\overline{\omega}) = R_x(\omega_{\overline{x}}) \cdot R_y(\omega_y) \cdot R_z(\omega_z)$ has been assumed.

Approximate geometrical relationships elicit the essential features of the VOP trajectory equations. The uncertainty of any particular vorticity measurement can be estimated from relations of the vorticity components to $\dot{r}$, ψ, and $\frac{\partial \psi}{\partial r}$ (the alternate vorticity basis described in preceding sections). These values, in turn, are simply related to the basic trajectory data, where errors are derived from known noise and trajectory characteristics. When the noise and trajectory characteristics (i.e., angular size, etc.) are distributed in known ways, depending upon experimental parameters, then all of the information needed to generate a resolution function is at hand. The propagation of measurement error through $\dot{r}$, ψ, and $\frac{\partial \psi}{\partial r}$ is described in Appendix C. Since the uncertainty of given vorticity measurement is based upon these parameters, it is important to known with what probability a given SNR or r_N (and thus vorticity component uncertainty, σ_i) will occur. The distributions of signal-to-noise ratio and/or transit times, and trajectory angular size are derived in Appendices B and E, respectively.

Figure 17 shows the geometry of an arbitrary trajectory. The figure is a representation of the unit solid angle chord (detector) surface on the unit sphere, where $\overline{a}$ is the distance of the centroid of the trajectory from detector center $(x=0, z=0)$, $\overline{\gamma}$ is the distance from the centroid to the effective center of curvature of the trajectory with $\gamma \sim \left[\frac{d\psi}{dr} \right]^{-1}$, and $\overline{c}$ is the distance from detector center to the apparent center of curvature.

$$\vec{C} = \vec{a} \cdot \vec{r}$$
$$= (a_x + y\cos\psi) + (a_z \cdot y\sin\psi)$$
$$\omega_c = \frac{\dot{r}}{y}$$

TRAJECTORY
SEGMENT

UNIT SOLID ANGLE
SURFACE ON UNIT
SPHERE
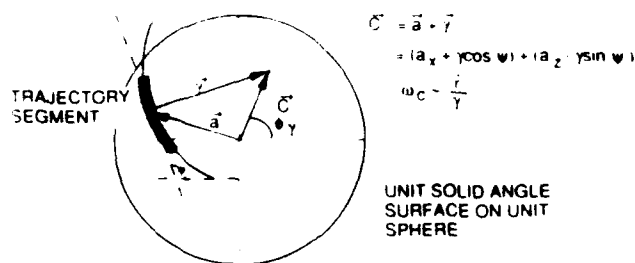
R 6932

Figure 17

Trajectory Geometry

For modest $|c|$ values ($\lesssim 1$), the approximate rotation rate of the reflection about the apparent center curvature is denoted $\omega_c \approx \dot{r}\frac{\partial\psi}{\partial r}$, and the vorticity components can be estimated by

$$\omega'_z \sim \frac{\omega_c\ |c|\ \sin\phi_\gamma}{\sqrt{|c|^2 + 1}}$$

$$2\omega'_x \sim \frac{\omega_c\ |c|\ \cos\phi_\gamma}{\sqrt{|c|^2 + 1}}$$

$$\omega'_y \sim \omega_c\frac{1}{\sqrt{|c|^2 + 1}}$$

In terms of the alternate basis $\dot{r}$, ψ, and $\frac{\partial\psi}{\partial r}$, Eq. (12) are

$$\omega'_z \sim \dot{r}\frac{\partial\psi}{\partial r}\ \frac{1}{\sqrt{1 + |c|^2}}\left(a_z - \frac{\cos\psi}{\frac{d\psi}{dt}}\right)$$

$$2\omega'_x \sim \dot{r}\frac{\partial\psi}{\partial r}\ \frac{1}{\sqrt{1 + |c|^2}}\left(a_x + \frac{\sin\psi}{\frac{d\psi}{dt}}\right)$$

$$\omega'_y \sim \dot{r}\frac{\partial\psi}{\partial r}\ \frac{1}{\sqrt{1 + |c|^2}}\ .$$

The propagation of the uncertainties in the quantities $\dot{r}$, ψ, and $\frac{\partial \psi}{\partial r}$, through Eq. (13) for the vorticity components, gives the component uncertainties. Keeping only dominant terms

$$\sigma_z = \delta\omega'_z \sim \left| \frac{\dot{r}a_z}{\sqrt{SNR}\cdot r_N} , \frac{\dot{r}\cdot\sqrt{r_\Delta}}{\sqrt{SNR}\cdot\sqrt{r_N}} \right|$$

$$\sigma_x = \delta\omega'_x \sim \left| \frac{\dot{r}a_x}{\sqrt{SNR}\cdot r_N} , \frac{\dot{r}\cdot\sqrt{r_\Delta}}{\sqrt{SNR}\cdot\sqrt{r_N}} \right| \qquad (14)$$

$$\sigma_y = \delta\omega'_y \sim \left| \frac{\dot{r}}{\sqrt{SNR}\cdot r_N} \right|$$

where the $|,|$ notation in Eq. (14) indicates the square root of the sum of the squares. The approximate total length, r_N, of the N-point trajectory, is the fraction of the (1 radian) angular size of the detector, and r_Δ is the minimum angular spacing between successive trajectory points. As expected, the curvature-related contribution to the uncertainty in ω'_x and ω'_z vanishes at detector center ($a_z = 0$, $a_x = 0$). In this case, the second (smaller) term dominates in the expression for $\delta\omega'_x$ and $\delta\omega'_z$.

In the large $|c|$ limit in which vorticity vectors are nearly perpendicular to the mirror normal, the ω_c approximation fails. In this case, $|\omega| \approx \dot{r}$, and $\overline{c} \approx \overline{\gamma} \gg \overline{a}$, giving

$$\omega'_z \approx \frac{\dot{r}}{\sqrt{1 + |c|^2}} (a_z - |\gamma|\cos\psi) \approx \dot{r}\left[a_z \frac{\partial \psi}{\partial r} - \cos\psi \right]$$

$$2\omega'_x \approx \frac{\dot{r}}{\sqrt{1 + |c|^2}} (a_x + |\gamma|\sin\psi) \approx \dot{r}\left[a_x \frac{\partial \psi}{\partial r} + \sin\psi \right]$$

$$\omega'_y \approx \frac{\dot{r}}{\sqrt{1 + |c|^2}} \approx \dot{r}\frac{\partial \psi}{\partial r} \quad .$$

The large $|c|$ limit gives the same uncertainties in the vorticity components. This error analysis is therefore expected to be valid for any arbitrary vorticity vector.

53

Having described the dependence of the errors on trajectory characteristics, the error distributions can b[...] derived in Eq. (14) for the component uncertainties, the dominant terms in the σ_i, $\sigma_i \propto \left(\sqrt{SNR} \cdot r_N\right)^{-1}$ [...] the determination of the distribution $p(\sigma_i)$ since the distributions of $p(SNR)$ and $p(r_N)$ are known. With t[...] power threshold set sufficiently high (Subsection 3.2.2), the variation in SNR produces a modest uniform broadening of the σ_i distribution. The variation in r_N then dominates the error distribution. This distrib[...] as a function of ℓ_ω (the total angular size of trajectory on the unit sphere) is derived in Appendix E. In large ℓ_ω approximation the distribution of trajectory lengths is given by

$$p(r_N) \propto \frac{r_N}{\sqrt{R^2 - r_N^2}} \qquad 0 < r_N < R, \ \ell_\omega \gg R$$

where R is the angular measure of the detector radius. (The random variation of a_x, and a_z is not inclu[...] this error analysis, and is yet another source of broadening.) Since $\sigma \propto \left(\sqrt{SNR} \cdot r_N\right)^{-1}$, we obtain

$$p(\sigma_i) \propto \frac{1}{\sigma_i} \frac{1}{\sqrt{\sigma_i^2 - \sigma_{i,min}^2}} \qquad \sigma_{i,min} < \sigma_i < \sigma_{i,max}$$

thus for large σ_i, Eq. (15) is approximately

$$p(\sigma_i) \cong \frac{C}{\sigma_i^2} \qquad .$$

The broadening due to the SNR distribution (and the contribution of a_x and a_z), suffices to remove the (integrable) singularity at $\sigma_{i,min}$ so that Eq. (16) is a good approximation over the full range. The uppe[...] limit $\sigma_{i,max}$ is either a function of the cutoffs imposed in the proximity tests (Appendix D) for a preset [...] This error distribution estimate is borne out by the calibration data (single vorticity vector) presented in Chapter 4 where the error distribution for each ω component in a laminar flow are presented. The know[...] distribution of errors leads naturally to an approximate resolution function described below.

For a subset of measurements of the quantity x, derived from a normal parent distribution characterized by σ_j, the contribution to the total distribution function in the range $\Delta\sigma$, is

$$P_x(x:\sigma_j) = \frac{a_j}{\sigma_j} e^{-x^2/2\sigma_j^2} w_j \, \Delta\sigma \qquad \sigma_j - \frac{\Delta\sigma}{2} < \sigma_j < \sigma_j + \frac{\Delta\sigma}{2}$$

where a_j is the amplitude of the jth contribution and w_j is the statistical weight. The expected form of the resolution function in the limit of a continuous σ distribution is then

$$R_x(x) = \int_{\sigma_{min}}^{\sigma_{max}} P_x(x:\sigma) \, p(\sigma)d\sigma$$

$$= c \int_{\sigma_{min}}^{\sigma_{max}} e^{-x^2/2\sigma} \frac{d\sigma}{\sigma^5}$$

$$= \frac{1}{x^4}\left[\left(\frac{x^2}{2\sigma_{min}^2}\right)^2 + \frac{x^2}{\sigma_{min}^2} + 2\right]e^{-x^2/2\sigma_{min}^2}$$

$$- \frac{1}{x^4}\left[\left(\frac{x^2}{2\sigma_{max}^2}\right)^2 + \frac{x^2}{\sigma_{max}^2} + 2\right]e^{-x^2/2\sigma_{max}^2} \quad .$$

(17)

These resolution function(s) are derived from calibration data with σ_{min} and σ_{max} estimated from the experimental error distributions. The calculation of the moments of this distribution is straightforward.

$$\overline{X^n} = \int_{-\infty}^{\infty} x^n R_x(x)dx$$

$$= \frac{\displaystyle\int_{\sigma_{min}}^{\sigma_{max}} \frac{d\sigma}{\sigma^4} \int_{-\infty}^{\infty} x^n \frac{\sqrt{\pi}}{\sigma} e^{-x^2/2\sigma^2} dx}{\displaystyle\int_{\sigma_{min}}^{\sigma_{max}} \frac{d\sigma}{\sigma^4} \int_{-\infty}^{\infty} \frac{\sqrt{\pi}}{\sigma} e^{-x^2/2\sigma^2} dx} \quad .$$

The moments of the normalized Gaussian distribution are $\bar{x} = 0$, $\overline{x^2} = \sigma^2$, $\overline{x^3} = 0$, $\overline{x^4} = 3\sigma^4$, etc. Then

$$\overline{X^2} = \sigma_R^2 = \frac{\displaystyle\int_{\sigma_{min}}^{\sigma_{max}} \frac{d\sigma}{\sigma^2}}{\displaystyle\int \frac{d\sigma}{\sigma^4}} = \frac{3\left| \dfrac{1}{\sigma_{min}} - \dfrac{1}{\sigma_{max}} \right|}{\left(\dfrac{1}{\sigma_{min}^3} - \dfrac{1}{\sigma_{max}^3} \right)}$$

$$\overline{X^4} = \frac{9(\sigma_{max} - \sigma_{min})}{\left(\dfrac{1}{\sigma_{min}^3} - \dfrac{1}{\sigma_{max}^3} \right)} \quad .$$

The variance and flatness relative to a normal distribution $\left| \dfrac{\sigma_{max}}{\sigma_{min}} = 1 \right|$ are

$$\frac{\sigma_R}{\sigma_{min}} = \left[\frac{3}{1 + \dfrac{\sigma_{min}}{\sigma_{max}} + \left(\dfrac{\sigma_{min}}{\sigma_{max}} \right)^2} \right]^{1/2}$$

$$\frac{F_R}{3} = \frac{\sigma_{max}}{\sigma_{min}} \left[1 + \frac{\sigma_{min}}{\sigma_{max}} + \left(\frac{\sigma_{min}}{\sigma_{max}} \right)^2 \right] \quad .$$

Note that for unbounded σ_{max}, the resolution function width σ_R, is $\sqrt{3}$ time greater than the gaussian val

$\sigma_{min} = \sigma_{max}$. Equations (18) and (19) are plotted versus $\dfrac{\sigma_{max}}{\sigma_{min}}$ in Figure 18.

56
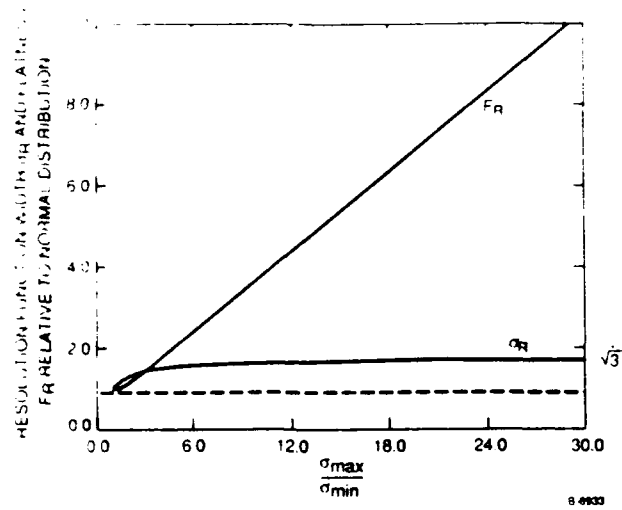
Figure 18

RMS Distribution Widths and Flatness Factors for Resolution Function Versus $\dfrac{\sigma_{max}}{\sigma_{min}}$,

Relative to the Normal Distribution Values

It is usually impossible to set $\overline{\ell}_\perp$ (the mean total trajectory angular size) to an arbitrary high value, since it is determined in part by the vorticity/velocity ratio:

$$\frac{|\overline{\omega}|}{|\overline{u}|}\, \ell_u = |\overline{\omega}|\, \tau_{tr} = \ell_\omega \tag{20}$$

where ℓ_u is the sampled volume dimension parallel to the flow and τ_{tr} is the transit time. As described in Appendix B, in geometries where the flow is inclined to the beam, the variation of the traversed sampled volume dimension and therefore transit time, results in a range of ℓ_ω at constant $\overline{\omega}$. Turbulent velocity fluctuations contribute to the $\ell_\perp$ broadening in a similar fashion.

For modest $\overline{\ell}_\perp$ in a turbulent flow a better estimate for $p(\sigma_i)$ is

$$p(\sigma_i) \approx \frac{C}{\sigma_i} \qquad .$$

Then Eq. (18) becomes

$$
R_\chi(x) = C \int_{\sigma_{min}}^{\sigma_{max}} e^{-x^2/2\sigma^2} \frac{d\sigma}{\sigma^4} = -\frac{C}{x} \frac{d}{dx} \left[\int_{\sigma_{min}}^{\sigma_{max}} e^{-x^2/2\sigma^2} \frac{d\sigma}{\sigma^2} \right]
$$

$$
= \frac{C\sqrt{\pi}}{2x^3} \left[erf\left(\frac{x}{\sqrt{2}\,\sigma_{min}}\right) - erf\left(\frac{x}{\sqrt{2}\,\sigma_{max}}\right) \right] - \frac{C}{\sqrt{2}\,x^2} \left[e^{-x^2/\sigma_{max}^2} - e^{-x^2/2\sigma_{min}^2} \right]
$$

These resolution functions are broader and their moments can be computed as before. The second mome this case (Eq. (21)) gives

$$
\frac{\sigma_R}{\sigma_{min}} = \left[2 \frac{\left(\dfrac{\sigma_{max}}{\sigma_{min}}\right)^2 \ln\left(\dfrac{\sigma_{max}}{\sigma_{min}}\right)}{\left(\dfrac{\sigma_{max}}{\sigma_{min}}\right)^2 - 1} \right]^{1/2}
$$

The resolution function width diverges weakly with unbounded σ_{max}, though σ_R is still less than $3\sigma_{min}$ a

$\dfrac{\sigma_{max}}{\sigma_{min}} = 30$. It is convenient, in any case, to truncate the error distributions beyond a present σ_{max} levt

order to produce reliable bounds on σ_R and minimize F_R.

In general, some intermediate form of $p(\sigma_i)$ is expected, and under differing experimental conditions the inclusion of other factors may be necessary, e.g., SRN and ℓ_ω broadening. If $p(\ell_\omega)$ is known, then

$$
p(\sigma_i:\dot{r}) = \int_{r_N} \int_{\ell_\omega} PSNR\left(\frac{\alpha \dot{r}^2}{\sigma_i^2 r_N^2}\right) p(\ell_\omega) \, d\ell_\omega \, dr_N
$$

where p_{SNR} is the SNR distribution function (Appendix B), $\dfrac{\alpha \dot{r}^2}{\sigma^2 r_N^2}$ is substituted for SNR from the expr

for σ_i, and $p(r_N:\ell_\omega)$ is computed in Appendix E. In experiments where turbulent flow fluctuations domi:

instrumental broadening, the detailed form of $p(\sigma_i)$ is obviously of less importance to the shape of the PDFs and values of the moments.

It must be emphasized that the σ_{min} and σ_{max} limits the expression for the normalized resolution function R, scale directly with the vorticity. Thus the resolution functions vary systematically with vorticity, complicating the deconvolution of instrumental broadening from true vorticity fluctuations. This inhomogeneous broadening, however, preserves the integral probability of vorticity component PDFs. When the probability of sampling a particular vorticity is influenced by the vorticity, corrections are required to eliminate this bias. In order to preserve the simple form of the resolution functions above, turbulent vorticity PDFs are corrected for vorticity dependence via sampling functions.

3.4.2 Vorticity Sampling Function

What is the probability per unit time of measuring vorticity $\vec{\omega}$, under fixed experimental conditions, and how should that value be weighted to obtain a true, unbiased vorticity distribution? The answer to this question constitutes a vorticity sampling function. The true vorticity PDF, $p(\vec{\omega})$ is related to the measured PDF, $p_m(\omega_i)$ by

$$p_m(\omega_x) = \int S(\vec{\omega}) \ p(\omega_x, \omega_y, \omega_z) d\omega_y d\omega_z$$

for example, where some normalization is imposed over the range of integration, and

$$p(\vec{\omega}) = S^{-1}(\vec{\omega}) \ p_m(\vec{\omega})$$

where $S(\vec{\omega})$ is the vorticity sampling function. Note the probability of measuring ω_i is influenced in general by the values of all components. The data rate at any point in vorticity space is given by

$$R = nAu \ S(\vec{\omega}) \tag{22}$$

where n is the probe particle number density and A is the cross-sectional area of the sampled volume normal to the flow velocity $\vec{u}$.

Proper statistical weights are given to vorticity components when generating PDFs and statistics. To the e that the statistical weighing factor, $1/\sigma_i^2$, varies systematically with vorticity, this must be corrected for. sampling corrections to the PDFs for data reduced with the optimal differencing scheme can be deduced fr the form of σ_i.

$$\sigma_i \propto \frac{\dot{r}}{\sqrt{SNR} \cdot r_N}$$

The explicit appearance of $\dot{r}$ in σ_i can be corrected directly by the sampling factor

$$S_r(\overline{\omega}) \propto (\dot{r})^{-2} \approx \left[\omega'^2_z + (2\omega'_x)^2 + |\overline{a}|^2 \, \omega'^2_y \right]^{-1}$$

A more subtle contribution with increasing $\dot{r}$ is the tendency of the r_N distribution to favor longer trajecto As seen in Appendix E, the mean trajectory length is a function of ℓ_ω. Variations in $\dot{r}$, and therefore ℓ_ω affect the PDFs through r_N. (Also, functional the form of the resolution function is weakly ℓ_ω dependent which is not strictly a sampling function type correction as defined.) In the large ℓ_ω approximation discus the preceding section, however, this effect is negligible and will not be examined here.

An important sampling function factor arises from the increased probability per unit time at higher vortici: that reflections will be swept into the detector solid angle. Again, for sampled volume transit time τ_{tr}, w $\dot{r} \sim \ell_\omega/\tau_{tr}$, which leads to

$$S_\Omega(\overline{\omega}) \propto \left[\frac{\pi + 4F\dot{r}\,\tau_{tr}}{16\pi F^2} \right]$$

where F is F-number of the optical system (which has been approximated by 1 in order to simplify all of foregoing discussions). The first term in the brackets is the fraction of the solid angle 4π subtended by th detector surface and the second term is the additional solid angle swept out by the detector surface in time in a frame rotating at $\dot{r} \approx \ell_\omega/\tau_{tr}$. In the general case where individual τ_{tr} values are unknown, this appr is inappropriate. Fortunately, an equivalent correction exists, based on detector transit time, τ_D. Detector

60

transit time weighing is needed in the case of the VOP for precisely the reasons sampled volume transit time weighing is required in Laser-Doppler Velocimetry (LDV). A proper time average is obtained for discrete random events of finite duration, like VOP data and "burst"-type LDV data, only when these events are weighted by the time interval over which they are observed (Buchhave, George, and Lumley, 1976)

$$\bar{\omega}_{true} = \sum_i \omega_i \tau_{Di} \Big/ \sum_i \tau_{Di} \qquad (25)$$

To verify that τ_D is the proper weighing factor, its mean value can be estimated using the same arguments which led to Eq. (24)

$$\bar{\tau}_D = \frac{\ell_u}{|u|} \left[\frac{\pi}{\pi + 4 \tau F \, \tau_{tr}} \right] \qquad (26)$$

where the second term in the denominator corrects for the probability that the reflection leaves the detector area in time τ_{tr}. At zero vorticity, this expression correctly reduces to $\bar{\tau}_D = \ell_u/|u| = \tau_{tr}$. The mean detector transit time weighted data rate. combining Eqs. (22), (24), and (26), is thus dependent of u and ω.

$$nA|u| \, S_\Omega(\bar{\omega}) \, \bar{\tau}_D = \frac{nV\pi}{16F^2}$$

where V is the sampled volume. Detector transit time weighing simultaneously eliminates both vorticity and velocity sampling bias.

This correction simultaneously accounts for the enhanced probability of measurement at high vorticity and the reduced contribution of these short events to the time average. This is illustrated in Figure 19. In the sampled volume transit time limited case. $\tau_D = \tau_{tr}$, and detector transit time is identical to the conventional LDV form.
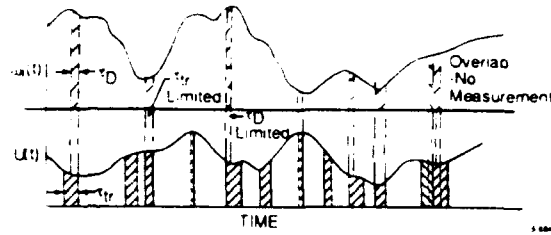
Figure 19

Transit Time Corrections. Correct averages are obtained by weighing vorticity values
in proportion to τ_{Di}, the time interval during which the particle is observed

Potentially the most difficult sampling corrections are those near zero vorticity, or the VOP singularity wh

$$S_0(\overline{\omega}) \to 0 \quad \text{and} \quad p_m(\overline{\omega}) \to 0 \text{ , as } |\overline{\omega}| \to 0 \text{ .}$$

This is related to the interpretation of near zero vorticity by the proximity tests (Appendix D) and has not

been fully clarified, nor has any explicit form of S_0 been derived. In such cases there is little available

information. Assumptions about the form of $p(\omega'_y)$ are probably required (i.e., that the vorticity field is t

dimensional and that the ω_y' contribution can be ignored) in order to fill in $p(\omega'_x)$ and $p(\omega'_z)$ near $|\overline{\omega}|$ =

an unbiased fashion. Statistically significant null vorticity caused intermittent irrotational flow ($\overline{\omega}=0$) can

be distinguished from the normal background errors. This is only expected to be troublesome for turbulei

flows with little or no mean shear or significant intermittency, and will be pursued in future work.

Another problematic form of sampling bias is the direct interaction of the vorticity/velocity ratio with the

proximity tests. Trajectory fragments are typically obtained when the convection velocity is high relative

local vorticity. Since proximity tests limit the allowable contamination of ω'_z and ω'_x measurement by t

large uncertainty in ω'_y, two-component fits are generally acceptable only near the detector center. This

effectively smaller detector area creates a sampling bias whose effects were observed experimentally and :

noted in Chapter 5.

The complete vorticity sampling function is

$$S(\overline{\omega}) = S_0(\overline{\omega}) S_r(\overline{\omega}) \tau_D \qquad (28)$$

which can be incorporated directly into the statistical weights during data analysis. (At present, S_0 is set to unity.)

The sampling function assures that no vorticity vector is systematically over- or under-counted in the measured PDFs. However, the implicit r dependence in the vorticity resolution function results in inhomogeneous broadening of the PDFs. Formally, the deconvolution of the PDFs alluded to in the previous section should be performed on the three-dimensional joint PDF, $p(\omega_x, \omega_y, \omega_z)$ with the resolution function $R(\omega_x, \omega_y, \omega_z)$. Since the breadth of the resolution functions scale approximately with $|\overline{\omega}|$, i.e., $\delta\omega/\omega \approx$ constant, the deconvolution can be linearized by transforming to logarithmic coordinates (scaled by $\ln|\omega|$). The final PDFs, $p(\omega_i)$, are the projections of the corrected PDF onto the coordinate axes. Such a computation is likely to be impractical, however, and approximate method will need to be employed. Empirical corrections to the moments, for example, as employed in Chapter 5, may be a generally satisfactory solution.

3.4.3 System Spatial and Temporal Resolution

The intrinsic spatial resolution of the VOP (particle diameter) has been discussed in Chapter 2. No discussion has yet been offered of the effects of finite sampled volume size. Apart from the direct effects on the vorticity statistics due to spatial gradients of the mean vorticity field, which are readily correctable, there is the more important issue of the vorticity/velocity ratio, $\dfrac{|\omega|}{|u|}$. If the velocity, $\overline{u}$, becomes large at given vorticity and sampled volume dimension ℓ_u (parallel to u), then the transit time, τ_{tr}, drops off along with trajectory angular size r_N. Since a much smaller angular displacement is observed, the precision of vorticity measurement suffers.

Conversely, if we insist upon maintaining a minimum mean $r_N = r_{N,min}$, then

$$\ell_u \geq \frac{r_{N,min}}{\frac{|\omega|}{|u|}}$$

which is a condition upon the sampled volume dimension parallel to the mean velocity. If $r_{N,min} = 0.1$ ra

and $\frac{|\omega|}{u|} = 1\ cm^{-1}$, then ℓ_u must be ≥ 1 mm.

Clearly the particle's position is not known within this volume without auxiliary data (i.e., simultaneous v

measurement). This is of little concern for vorticity statistics, when the mean flow parameters change onl

slightly in the streamwise direction and the Lagrangian vorticity fluctuations are slow. This is problematic

however, in transforming from the Lagrangian to the Eulerian viewpoint where the spatial vorticity structu

convecting through the sampled volume is sought based upon the random time series. The minimum corre

distance is typically several (6 to 8) particle diameters at high particle loading (Subsection 2.4).

The temporal resolution of the VOP is a more difficult issue. Independent of flow fluctuations, the instru:

uncertainty in the vorticity components, $\delta\omega_i$, can be expressed as an uncertainty relation

$$\delta\omega_i\, \tau_D = C_i$$

where τ_D, detector transit time, is the time for which the particle is observed and C_i is a constant (or func

which depends upon experimental parameters. The longer the particle reflection can be observed the bette

the precision of the vorticity measurement. A changing vorticity, however, imposes an upper limit on τ_D

In a turbulent flow, an eddy is not usually expected to persist for more than a single rotation, i.e., the vor

vector, $\bar{\omega}$, changes by $O(\bar{\omega})$ in the time $\sim 2\pi/\omega$. The time for which the particle is observed is $\tau_D \sim \frac{r_N}{\omega}$

$$\frac{\delta\omega}{\omega} \sim \frac{r_N}{2\pi}$$

independent of instrumental noise. The error associated with being always arbitrarily close to short-lived fine scales of turbulence (the "support" of the dissipation) produces an additional broadening in turbulent PDFs which does not exist in laminar distributions. Interestingly therefore, even χ_ν^2 distributions should have strong turbulence signatures, since non-constant vorticity (vortex stretching) degrades fit quality (see Subsection 5.2.2). The implications of Eq. (29) deserve further study.

The other temporal resolution issue is data rate. Specifically, what is the peak mean data rate? Since overlapping trajectories can be recognized and rejected, events of mean duration $\overline{\tau_D}$, can be crowded together with mean time between events τ_E, until overlap eliminates more events per unit time than are added by decreasing τ_E. For random data, a Poisson distribution describes the probability that an event will occur at time t, given an event at time $t = 0$, and a mean time between events, τ_E, or event rate R_E ($= 1/\tau_E$),

$$p_E(t;\tau_E) = e^{-\tau/\tau_E}$$

For events of mean duration τ_D, the (average) total probability of overlap is the probability that the next event begins within time τ_D.

$$P_{overlap}(\tau_E;\overline{\tau_D}) = \tau_E \int_0^{\overline{\tau_D}} e^{-t/\tau_E} dt = \left(1 - e^{-\overline{\tau_D}/\tau_E}\right) \quad .$$

But for each overlap, two events are lost. Thus the net data rate is the mean event rate, R_E, less the overlap rate

$$R_{DATA} = R_E - 2R_E\left(1 - e^{-\overline{\tau_D}/\tau_E}\right) \qquad \text{(valid for } \tau_E \gg \overline{\tau_D}) \quad .$$

The peak mean data rate is that for which R_{DATA} is a maximum:

$$\frac{dR_{DATA}}{d\tau_E} = 0, \quad \text{at } R_E\overline{\tau_D} = \overline{\tau_D}/\tau_E = 0.31 \quad .$$

65

The mean time between events must be about three times the mean event duration to achieve the highest rate which $R_{PEAK} = 0.46 R_E$. The peak mean data rate for $\overline{\tau_D} \sim 0.5$ ms is ~ 300 Hz. At peak rate, half of the events must be discarded due to trajectory overlap. Under these circumstances, the importan. reliable error recognition algorithms is evident. The peak instantaneous data rate is considerably higher. only by the minimum spacing of the shortest events. These closely space events, however, are extremel and very short time autocorrelation data is sparse for most applications.

4 WATER COMPATIBLE VOP PARTICLES

The description of the VOP to this point has been quite general in regard to fluid/particle systems, stressing the need for refractive index matching and the advantages of neutral buoyancy, etc. For water as the working fluid, however, these simple prescriptions constituted a real technical challenge: the list of possible particle materials satisfying these needs is very brief (see Table 2 below).

In practical terms, water-compatibility is essential for the development of the VOP into a widely used research instrument. Most fluid dynamics laboratories around the world have either water tunnels or wind tunnels. Organic fluids cannot be seriously considered for large-scale applications (with the notable exception of the Pennsylvania State University glycerine tunnel in which the PMMA VOP particles could work).

To solve this problem, a new class of vorticity probe particle made of Acrylamide gel which provides excellent index and density matching was invented. The quality of the match is due primarily to the fact that gel is comprised of 90 to 95 percent water. After a brief review of particle manufacturing methods and materials, the new Acrylamide process will be described and VOP water calibration data in laminar Couette flow will be presented.

Table 2. Candidate Materials

Material	n_D	ρ_p/ρ_f	Status
Fluorocarbon solids Pentadecafluorooctyl Methacrylate (PDFOMA)	~1.355*	1.8*	Mirrors incorporated, low yield: VOP tested
Fluorocarbon liquids Perflorinated polyether Perfluorophenanthrene	~1.31* 1.334	2.0* 2.0	Mirrors not yet incorporated
Gels Agar (polysacharrides) Acrylamide (5 to 10%)	? ~1.34*	? 1.04*	Not yet tested Best probe particles to date
*Values are concentration, or molecular weight dependent.			

67

4.1 Review of Particle Manufacturing Techniques

For a description of the original VOP particle process, refer to Frish and Webb (1981). The technique i briefly recounted below to introduce the concepts of suspension polymerization.

4.1.1 Suspension Polymerization

All types of VOP particles are manufactured by suspension polymerization techniques involving four bas features:

1) Liquid monomer, from which the solid polymer is made in the presence of a polymerization init dispersed as small droplets in a medium in which it is insoluble.

2) The medium, either aqueous or non-aqueous depending upon the type of monomer, actively or passively inhibits coalescence of the dispersed monomer droplets.

3) The surface tension between the phases maintains sphericity of the droplets during the period in the material cures.

4) Lead carbonate mirrors dispersed in the monomer prior to creating the suspension remain withii droplets.

The pearl pigmentation additive ZTX-B (formerly a product of the Mearl Corporation, now available on foreign suppliers), containing basic lead carbonate mirrors was designed by the manufacturer for use in : plastics. It contains a plasticizer, dibutyl-pthalate (DBT), and ketones as solvents or thinners. This slur: readily miscible with methyl methacrylate, the monomer of poly(methyl methacrylate) (PMMA) from wi original particles were made. The target concentration of mirrors in the distilled monomer will produce average of one to two mirrors per 30 μm diameter droplet. It is evidently important for the mirrors to r well dispersed in the monomer to achieve the most uniform distribution of mirrors in the suspension. A quantity of benzoyl peroxide is added to this solution (1 g/liter) as an initiator. A suspension of small n droplets is made in a buffer solution by vigorous agitation (a blender works well).

The buffer solution consists of low molecular weight, 80 percent hydrolyzed poly(vinyl alcohol) (PVA) at 10 to 20 g/liter in distilled water. The PVA acts as an active dispersant which inhibits thinning of the buffer solution layer between droplets when they interact. The surfactant action of the PVA also aids by inhibiting the formation of new surface by creating a skin-like layer on the droplet. Small quantities of salts are added; NaCl modifies surface tension, and reduces the tendency for electrostatic forces to promote coalescence, and ammonium thiocyanate, NH_4SCN, inhibits the formation of emulsion polymer. This suspension is heated and stirred, and the droplets cure. The product is a fine powder of hard, clear, spherical PMMA particles and the mirrors remain inside of spheres of sufficient size to accommodate them. The desired size distribution is obtained by repeated gravitational sedimentation.

This is the model of suspension polymerization that has guided and informed the development of water compatible VOP particles using new materials. The first approach to water compatibility used the fluorinated acrylic plastic poly(pentadecafluorooctylmethacrylate) or PDFOMA. Several crucial differences, due to the troublesome nature of fluorocarbon chemistry, limit the usefulness of the PMMA model in this case. The second and most fruitful avenue employed acrylamide gel. This water soluble polymer network effectively turns the PMMA model inside-out, with a non-aqueous buffer and an aqueous polymer solution as the dispersed droplet phase. After summarizing the fluid/particle systems that have been used or are still in development, a description of the water compatible particles is given in Subsection 4.2.

4.1.2 Summary of Fluid/Particle Systems

Table 3 lists the fluid/particle systems conceived to date, along with the relevant physical properties of the materials and the particle dynamic response. For PMMA probe particles, both p-cymene and DBT are routinely used as working fluids in small scale experiments and in our precision Couette flow apparatus described in Chapter 5. P-cymene is a light, strong-smelling, aromatic hydrocarbon. Its toxicity is low, but it is quite flammable. DBT, as mentioned above, is a commercial plasticizer with 30 times the kinematic viscosity of p-cymene. These two fluids provide a convenient means of spanning a large Reynolds number range with a

69

Probe Particle	Fluid	Densities ρ_p,ρ_f	Refractive Indices n_p,n_f	Translational Response T_u (ms)	Rotational Response T_r (ms)	F Vis ν_f
30 μm Diameter Particles				ψr^2	ψr^2	
PMMA	P.Cymeme	1.2,0.9	1.49,1.49	0.18	0.04	0.0(
PMMA	Dibutylpthalate	1.2,1.04	1.49,1.49	0.006	0.001	0.1
PMMA	60 wt% Z 1 in water	1.2,2.0	1.49,1.49	0.06	0.025	0.0
PDFOMA	Water	1.75,1.0	1.355,1.33	0.1	0.026	0.0
Acrylamide gel, 8 wt%	Water	1.04,1.0	1.34,1.33	0.08	0.016	0.0
LLNL Aerogel*	Air	0.005,0.001	1.00,1.00	0.03	0.008	0.1

Poly(methlmethacrylate) = PMMA
Poly(pentadecafluoroctylmethacrylate) = PDFOMA
*Not yet attempted

single flow apparatus. Aqueous ZnI_2 solutions are not currently used because they are quite dense and corrosive.

New silica aerogel technology from Lawrence Livermore National Laboratories has made anair-compatit a possibility. These "frozen smoke" aerogels have been produced with densities of ~0.004 g/cc and ret index near unity. A VOP probe particle of this type could be used in wind tunnels. The potential of manufacturing such aerogel spheres is under study.

4.2 Water Compatible Particles

Two successful approaches to water-compatibility , the fluorinated acrylic plastic and acrylamide gel met are described below.

4 2.1 <u>PDFOMA Particles</u>

PDFOMA is a perfluoroalkyl ester of methacrylic acid which is used in the contact lens industry, co-polymerized with other materials. It is quite expensive, about $3 per gram. Its polymerization chemistry is essentially the same as other acrylics, except for its extreme sensitivity to the presence of oxygen which inhibits polymerization. Azobis-isobutyronitrile (AIBN) is the preferred initiator. The first difficulty encountered with PDFOMA is that basic lead carbonate mirrors do not disperse readily the monomer. The suspending agents in ZTX-B (or P80-H) are not compatible with the monomer. Careful multiple washings in alcohol are required to remove the suspending materials (e.g., even a mono-layer of DBT on mirror surfaces is apparently enough to promoted clumping of mirrors in PDFOMA). Final dilution must be one part in $\sim 10^8$. Even so, the strongly hydrophobic perfluorinated chains are not compatible with the basic lead carbonate mirrors. In order to render the mirrors equally hydrophobic they are 'teflon-coated' by treatment with a dilute perfluoroalkyl triethoxysilane solution. The adhesion of the silanol groups to the mirrors is still rather poor, but evidently enough to give good dispersion in the monomer. This monomer solution must be de-gassed to eliminate oxygen and excess alcohol. The buffer solution must also be modified. *The hydrophobic droplets tend to cluster quickly. Increased concentrations of higher molecular weight PVA are required.* NH_4SCN is no longer needed but higher NaCl concentrations are used. Pure nitrogen is bubbled through the buffer while heating and stirring prior to and during polymerization to prevent oxygen poisoning.

A transmission/reflection photomicrograph of the resulting product is shown in Figure 20. The boundaries of the spherical poly(PDFOMA) particles are clearly visible. These particles are from 10 to 50 μm in diameter and only 25 percent contain mirrors which are barely visible in the photograph. Some mirrors can be seen nearly edge-on, while others show clear reflections. Some mirrors exhibit a poorly understood surface contamination which reduces their reflectivity.

Poly(PDFOMA) particles have been tested in water. The reflections are adequate, but the data rejection rate is high. Further, these particles are too dense to be used in many applications, particularly when larger
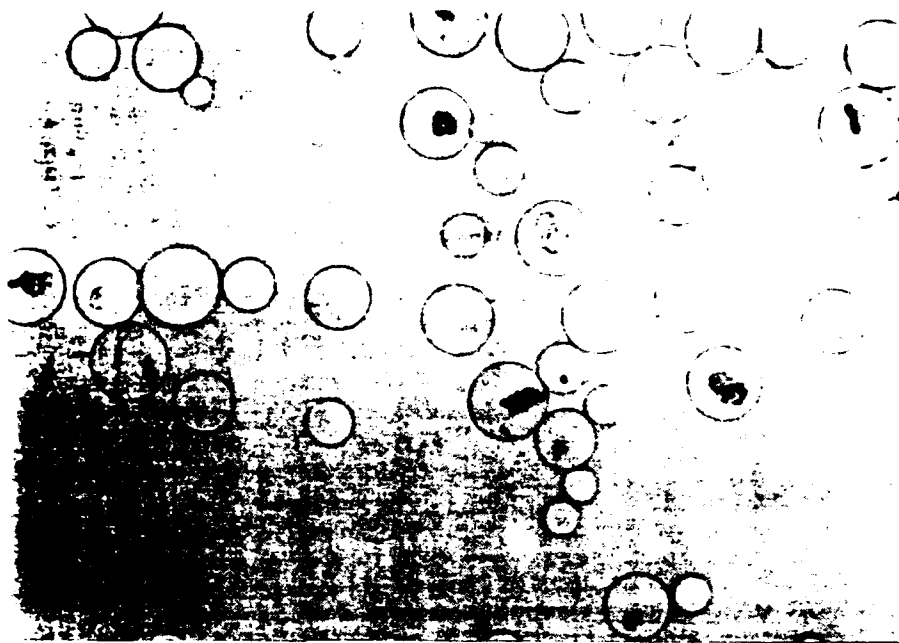
V-502

Figure 20

Transmission/Reflection Photomicrograph of PDFOMA VOP Particles

particles/mirrors are needed. The success of the acrylamide gel process, however, obviates the need to PDFOMA process further.

4.2.2 Acrylamide Gel Particles

Acrylamide gel is a visco-elastic material that is commonly used as an electrophoresis medium in bioch: research and biotechnology industries. The gel is made by polymerizing acrylamide with small quantit; acrylamide in a dilute aqueous solution, resulting in cross-linked polymer network which forms a rubbe that is 90 to 95 percent water by weight. The polymerization reaction requires the addition of an initia ammonium persulfate, and proceeds rapidly when a catalyst, tetramethylethylenediamine (TEMED) is a the solution. The mechanical and optical properties of the resulting gel material are controllable via pol concentration and degree of cross-linking, but typically has an index of refraction of ~1.34 and densit; 1.04 g/cc. Satisfactory VOP particle characteristics have been achieved using an 8 percent by weight a solution of acrylamide/bis-acrylamide at a 50:1 ratio.

72

To the author's knowledge, suspension polymerization (in a non-aqueous medium) has never before been used to manufacture acrylamide gel spheres. This procedure is not a straightforward extension of textbook methods. In particular, difficulties are encountered because the polymer forms rapidly (often within seconds) after addition of the TEMED catalyst to the unpolymerized acrylamide solution, thereby preventing the break-up into droplets. Furthermore, the mirrors tend to clump in the aqueous solution and tend to migrate to the boundary between the solution and the suspending medium.

The first of these difficulties is solved by selecting a suspending medium with special properties. "Thoroil", a product of the Kurt J. Lesker Company, is chemically inert, is immiscible with the gel ingredients, has low toxicity and is inexpensive. Most importantly, it is sufficiently polar to dissolve the TEMED catalyst. This latter property is critical to the success of the gel particle manufacturing process since by dissolving the catalyst directly in the oil, the catalytic action is inhibited until the acrylamide solution is dispersed in the oil. The catalyst then enters the spherical droplets by diffusion and curing begins. The problem of mirror clumping and migration is remedied by the addition of high molecular weight polyethylene oxide (≤ 0.1 percent). This has the effect of producing a highly non-Newtonian fluid which effectively immobilizes the mirrors. Acrylamide polymerization is also inhibited by oxygen. All of these fluids, including the suspension oil, must be thoroughly degassed. A more detailed discussion of acrylamide particle manufacture is included as Appendix F.

A phase contrast photomicrograph of an early batch of acrylamide gel particles is shown in Figure 21. The hexagonal mirror shape can clearly be seen. The index match is so close that without phase contrast, the gel sphere boundaries would be invisible. Many of these spheres are more than 100 μm in diameter, and some mirror clumping is visible. Quality control and continuous processing can improve these particles and better control their size distribution, though they have already provided high quality vorticity data in water without the problems associated with the PDFOMA process.

73
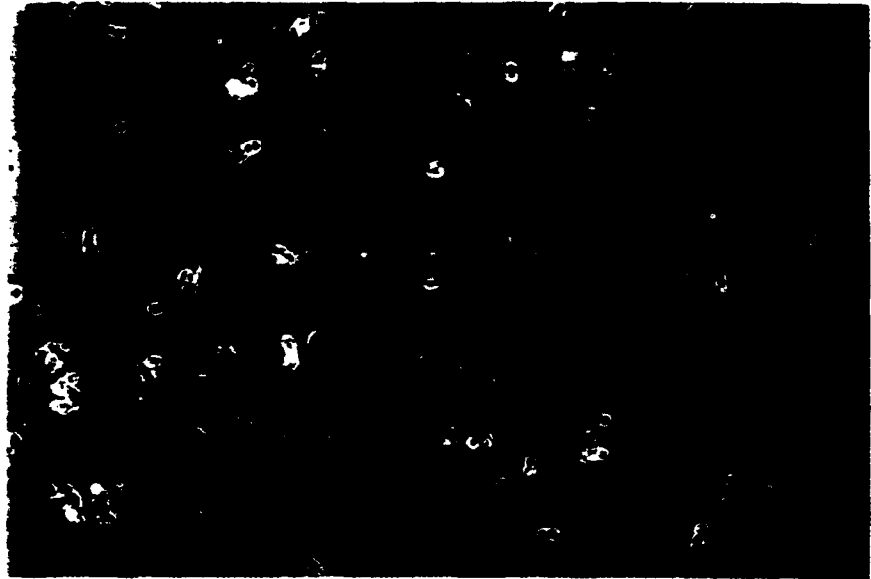
V-503

Figure 21

Phase Contrast Photomicrograph of Acrylamide Gel VOP Particles

4.2.3 Water Calibration Data

The acrylamide gel particles were first tested in water using a precision Couette flow apparatus. This de
described in Chapter 5. Suffice it here to say that the particles were uniformly distributed in a laminar
with a spatially and temporally constant vorticity field with expected value

$$(\omega'_x, \omega'_y, \omega'_z) = (0, 0, 1.35 \text{ s}^{-1}) \quad .$$

The measured vorticity distributions are presented in Figure 22. The ω_z (spanwise) distribution Figure
exhibits a strong peak at 1.25s with a FWHM ~10 percent. It should be emphasized that this is a calit
Small variations in the positions of optical elements result in a net departure from the nominal angular
magnification. The calibration factor, i.e., the ratio of the expected and measured peak values quoted a
should be used to scale all data acquired in the same optical configuration thereafter. Figure 22(b) is th
(streamwise) whose mean value is near zero as expected, with ~5 percent FWHM. The ω_y (normal)
distribution is many times broader than the others. This is the anticipated consequence of the VOP geo
and finite instrumental precision examined in Chapter 3.

74
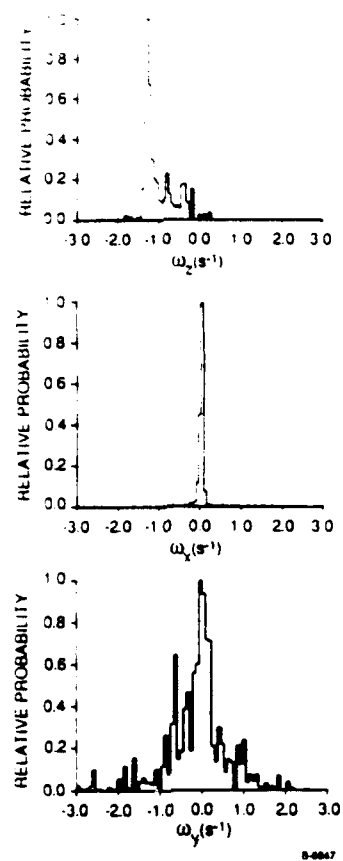
Figure 22

Laminar Flow Histograms (R/R$_c$ = 0.5) Water Calibration Data

Several aspects of these calibration data require some discussion. In particular, the existence of a broad secondary peak at $\sim \omega'_z/2$ must be accounted for. Examination of the individual events comprising the secondary peak appear to be valid data. Indeed they are. This peak is the result of stable particle pairing at low shear rate (ω_z) due to weak surface interaction. Also the widths of these distribution should be derivable from the component error distributions and the resolution function arguments of Chapter 3.

From the expression of Jeffrey (1922), the angular velocity Ω, of an ellipsoidal particle in a uniform shear, ω_0, is

$$\Omega = \frac{\alpha_\eta \omega_0}{1 + \beta_\eta \sin^2 \gamma_\eta \omega_0 t}$$

where α_η, β_η, and γ_η are coefficients depending upon the aspect ratio, η, of the particle. Paired spheric. particles of radii a_1, and a_2 are taken to behave as ellipsoids of aspect ratio

$$\eta = \frac{a_1 + a_2}{\max(a_1, a_2)} \quad .$$

For $a_1 = a_2$, $\eta = 2$. The expression for $p_\eta(\Omega)$, the probability density function (PDF) of observing the rate Ω, is

$$P_\eta(\Omega) = C \left[\frac{\partial \Omega}{\partial t} \right]^{-1} \quad .$$

Differentiating Eq. (33) and eliminating t, gives

$$P_\eta(\Omega) = \alpha_\eta \left[\alpha_\eta^3 \gamma_\eta \Omega^2 \sqrt{\left[\frac{\alpha}{\beta \Omega} - \frac{1}{\beta} \right] - \left[\frac{\alpha}{\beta \Omega} - \frac{1}{\beta} \right]^2} \right]^{-1}$$

in the interval. $\gamma_\eta < \Omega < \alpha_\eta$. The PDF for a single spherical particle reduces to $p_0(\Omega) = \delta(\Omega - \Omega_c$ the total PDF is

$$p(\Omega) = (1-f)p_0(\Omega) + fp_\eta(\Omega)$$

where f is the fraction of paired particles observed. For the calibration data shown here, $f \approx 0.4$.

If the steady state is taken to be paired fraction f, at the shear ω_0, then a calculation of pairing (i.e., col rate should allow an estimate of pair lifetimes in the shear. If collisions are assumed to take place for a of impact parameter $b \leq d$ $(=2a)$, where d is the particle diameter (Subsection 2.3.4) then the total co frequency is

$$\dot{n} = \int_0^d 8n\sqrt{d^2 - b^2}\ \omega_0 b\ db$$

$$= \frac{4}{3} n\omega_0 d^3$$

$$= \frac{\alpha\omega_0}{\pi}$$

where α is the volume fraction of particles in the flow. If the pairs have a mean lifetime τ_{pair}, then the equilibrium pair fraction is

$$f = \frac{\alpha\omega_0\tau_{pair}}{\pi} \qquad . \tag{34}$$

For the low shear calibration data, $\alpha \approx 10^{-3}$, $\omega_0 \sim 1\ s^{-1}$, and $f \sim 0.4$, so $\tau_{pair} \sim 10^3 s$, suggesting that the pairs survive indefinitely at this shear rate.

This result is somewhat surprising. Figure 23 is a map of the relative motion of sphere centers in the plane of a uniform shear, taken from Batchelor and Green (1972a). Open sphere trajectories are those for which $(b/a)^2 \geq 0$ in the preceding analysis where a is the particle radius, but for $(b/a)^2 < 0$ (imaginary impact
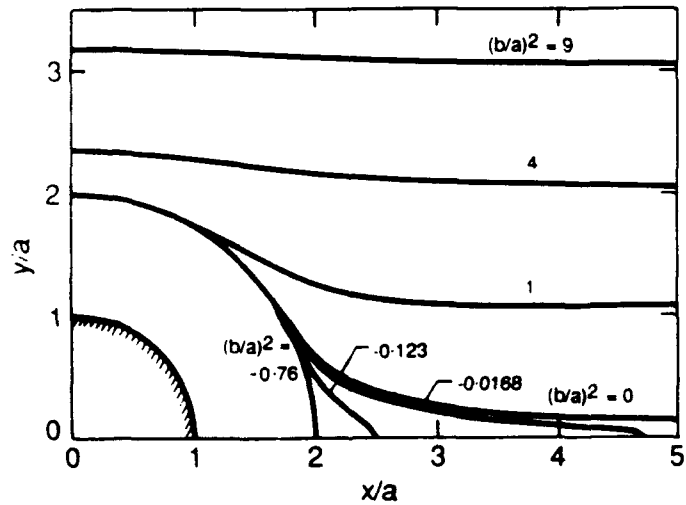
Figure 23

Interaction of Two Freely-Moving Spheres in a Linear Shear Flow (from Batchelor & Green, 1972a)

77

parameter. b') sphere trajectories are closed, i.e., the pairs are stably bound. The imaginary impact par simply interpreted as the inaccessability of the $(b/a)^2 < 0$ region to unperturbed trajectories. Apparent: brownian motion, triplet interaction, or flow field fluctuations (perhaps also sphere imperfections, comp surface interactions) can transport spheres in relative motion across the $(b/a)^2 = 0$ boundary (in both directions). Pair lifetimes can be quite large in Laminar shear flows. After a sufficient period of time shearing flow, starting from some initial distribution, it appears that a steady supply of single particles available only because triplets, etc., are unstable in the flow and the odd particles is always stripped loc unstable pairs (e.g., in a turbulent shear flow) the lifetime approaches one turnaround time $1/\omega_0$, and th equilibrium pair concentration reduces to $\sim \alpha/\pi$. Evidence for pair disruption by turbulence is seen in Chapter 5.

The component error (σ_i) distributions are shown in Figure 24. As was argued in Subsection 3.4.1, the seen to be distributed approximately as $1/\sigma_i^2$. From estimates of σ_{min}, and σ_{max} the expected resolutic functions can computed and compared to the measured calibration PDFs. In the special case of ω_z, the resolution function is convolved with Eq. (33) to include the pair contribution. The mean aspect ratio 1 to be $\bar{\eta} = 1.6$ and $f = 0.4$. These PDFs are shown in Figure 25. The essential features of these data apparently accounted for in this analysis. There appears to be an excess noise not seen in the σ_i distrib however, which is particularly apparent in the wings of the ω_y PDF. Further study is required.
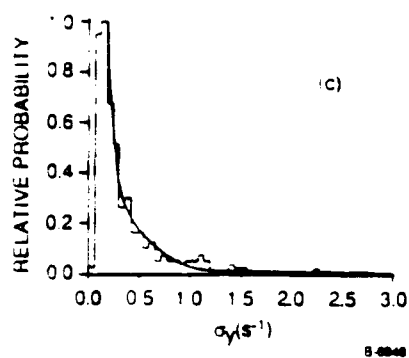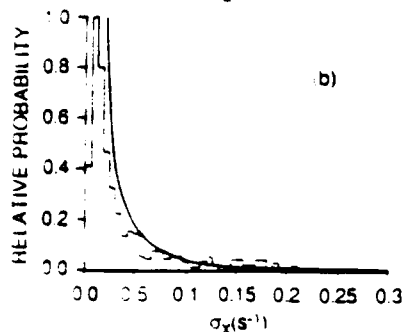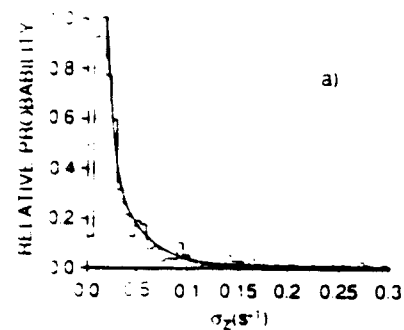
Figure 24

Measured Error Distributions Corresponding

to the Histograms of Figure 22.
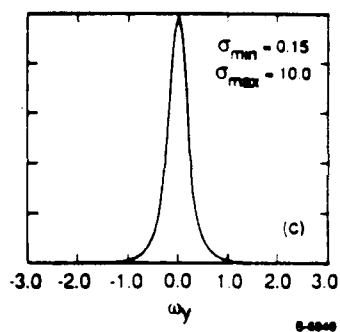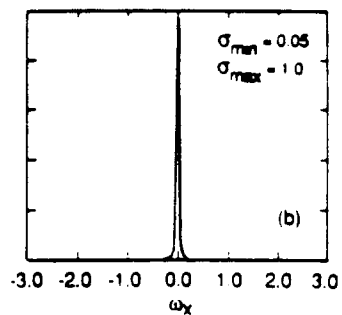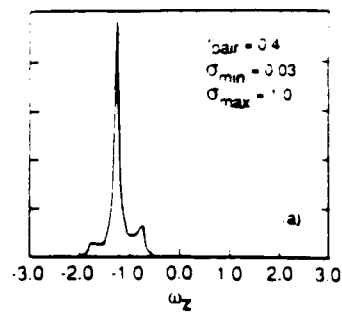
Figure 25

Resolution Functions Calculated from the Measured

Error Distributions (Compare with Figure 22)

Taylor-Couette flow, the flow between concentric rotating cylindrical surfaces, continues to be an impor laboratory for the study of the transition to turbulence and of large scale coherent vortical structures. V measurements have been performed in six distinct Couette flow regimes, which are enumerated in Subsection 5.1.1. Calibration data is acquired in the laminar flow regimes. Evidence of coherent vorti structure is observed in the outer boundary rotation turbulence data. The statistics of these turbulent flo similarities to standard turbulent boundary layers. Inner boundary rotation flows show the characteristic patterns of the "spectral evolution" to turbulence (Coles, 1965) as verified by flow visualization at Reyn number corresponding to the measurements. Spatial and temporal periodicity of the components of the are measured, which are compared with numerical simulations.

5.1 Couette Flow

In selecting a flow field in which to verify the operation of the VOP both in laminar and turbulent flow conditions, the following criteria were applied: 1) the flow apparatus must be useable with all of the V(working fluids used previously, culminating with water; 2) it should be a device of small to moderate s 3) it must possess well defined laminar regimes where the vorticity distribution is well known; 4) it mu range of accessible Reynolds number sufficient to reach fully developed turbulence with statistics comp other standard flows; and 5) the potential to display coherent vortical structures. It is difficult to concei flow which meets these criteria more precisely than Couette flow. A benchtop precision Couette flow d be made to function with virtually any fluid in relatively small volumes. Sub-critical flows posses a cor vorticity vector everywhere in the flow. Depending upon which boundary surface is rotating, Couette t vorticity field exhibit astonishing variety and richness.

5.1.1 Couette Flow Regimes

As mentioned above, there is great variety in Couette flow behavior which can be generally divided into categories: flows dominated by the rotation of the inner (cylindrical) boundary or those dominated by boundary rotation.

80

Let the radius and angular velocity of the inner and outer cylindrical boundaries be denoted r_i, Ω_i and r_o, Ω_o respectively. The boundary conditions on the velocity field are $U_\theta(r=r_i) = \Omega_i r_i$ and $U_\theta(r=r_o) = \Omega_o r_o$, the time-independent (sub-critical) solution of the Navier-Stokes equations gives (Landau and Lifshit. 1959)

$$U_r = U_z = 0 \qquad U_\theta = ar + \frac{b}{r}$$

where $a = \dfrac{r_o^2 \Omega_o - r_i^2 \Omega_i}{r_o^2 - r_i}$ and $b = \dfrac{(\Omega_i - \Omega_o)r_i^2 r_o^2}{r_o^2 - r_i^2}$

From the equation for the curl operator in cylindrical coordinates, the only non-zero component or the vorticity is

$$\omega_z = \frac{1}{r}\left[\frac{\partial(rU_\theta)}{\partial r}\right]$$

$$= 2a$$

Thus the vorticity vector has a constant magnitude and direction everywhere in flow field. Note that when $\Omega_o r_o^2 - \Omega_i r_i^2 = 0$, then $a = 0$ and the flow is irrotational. This is a special point. The necessary and sufficient condition for the stability of the (inviscid) flow field is the Rayleigh criterion

$$\frac{d}{dr}\left(rU_\theta(r)\right)^2 > 0$$

which reduces to

$$\Omega_o r_o^2 > \Omega_i r_i^2$$

For the case of outer boundary rotation ($\Omega_o = 0$) the flow is stable. For inner boundary rotation ($\Omega_o = 0$) the flow is unstable. For finite viscosity, there is a critical Reynolds number for inner cylindrical rotation marking the onset of more complex flows.

81

Each cylinder can be thought of as possessing its own Reynolds number based upon boundary surface speed and gap, $g = r_o \cdot r_i$.

$$R_o = \frac{\Omega_o r_o (r_o - r_i)}{\nu}, \quad R_i = \frac{\Omega_i r_i (r_o - r_i)}{\nu}$$

the height of the fluid annulus is usually much greater than g., i.e., $h/g \geq 30$. A flow is generally described by particular type of coordinates (R_o, R_i) on a map of R_i versus R_o. One interesting aspect of Couette flow that the flow at (R_o, R_i) is not necessarily unique. Several different stable states may be reached depending upon how (R_o, R_i) is approached.

A map of R_o versus R_i from Busse, Gollub, Maslowe, and Swinney (1985) is reproduced below in Figure 26(a). The outer boundary rotation dominated flow map is indicated in Figure 26(b) by greatly extending the R_o axis. Only the cases of $R_o = 0$, $R_i > 0$ and $R_o \neq 0$, $R_i = 0$ are considered. Moving up R_i axis from 0, at $R_i = R_c$ the Couette flow becomes unstable and secondary flows known a Taylor vortic appear. These vortices are stationary counter-rotating vortex pairs stacked up and down the span (see Figure in Section 5.3.1). At $R_i/R_c \sim 1.2$ the secondary flow itself becomes unstable to azimuthal disturbance, a: flow selects one of several possible periodic states known as wavy-vortex flow (Coles, 1965). This state characterized by traveling azimuthal waves superposed (non-linearly) on a Taylor vortices. At $R_i/R_o \sim 1$ incommensurate frequencies appear in the wavy-vortex spectra (Fenstermacher, Swinney, and Gollub, 197 giving rise to quasi-periodic flows. With increasing R_i, broadband background fluctuations begin to appe finally overwhelming the periodicity which is no longer detectable at $R_i/R_c \geq 23$. The basic Taylor vorte pattern still persists with fine turbulent structure everywhere in the flow. This process is referred to as the "spectral evolution" to turbulence (Coles, 1965).

The behavior along the R_o axis is distinctly different. For $R_i = 0$, is stable and persists in the giving the expected Couette value

(a) From Busse, Gollub, Maslowe, and Swinney (1985)

(b) Note That Onset of Fully Developed Turbulence is Dependent on Flow Conditioning

Figure 26

Couette Flow Map. VOP Measurements at ●

$$\omega_z = \frac{2\Omega_0}{1 - \left[\dfrac{r_i}{r_o}\right]^2} \tag{35}$$

until wall-bounded shear flow instabilities akin the ordinary boundary lay type initiates a 'catastrophic' transition

to turbulence. This turbulence is initiated at isolated spots in the boundary lay which grow, dominate the flow,

and then disappear, with a pulsating sort of regularity. In this respect, turbulent Couette flow is similar to pipe

flow, exhibiting intermittency with increasing Reynolds number, until the intermittency factor, , approaches

unity when the flow is fully turbulent.

83

The Couette flow device, designed and constructed for this program, is shown below in Figure 27. The relevant parameters are specific in Table 4. This design is unusual in several respects. First, it is actuall Couette flows rather than one, as seen in the figure. The middle cantilevered cylinder rotates freely abou central cylindrical spindle. A fixed outer cylinder was required on which flats could be cut or molded for

OUTER FLUID SECTION —
INNER FLUID SECTION —
ROTATING PRECISION CUT AND POLISHED PLEXIGLAS SHELL —
OUTER PLEXIGLAS SHELL —
— BEARINGS
— COOLING CORE
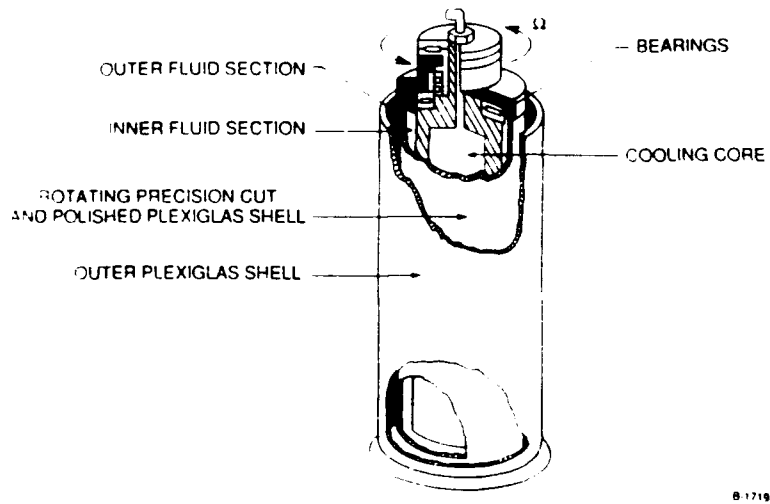
Figure 27

Precision Couette Flow Apparatus (timing belt drive)

Table 4. Couette Flow Apparatus Parameters

Inner Fluid Annulus

$r_o = 4.477$ cm, $r_i = 3.944$ cm, $r_i/r_o = 0.881$

$G = 0.559$ cm, $h/g = 39$

Outer Fluid Annulus

$r_o = 4.738$ cm, $r_i = 5.127$ cm, $r_i/r_o = 0.894$

$G = 0.611$ cm, $h/g = 36$

mounting of the output coupling optics for the VOP described in Subsection 3.1.2. The rationale for this approach derives from the need to accommodate the fixed outer cylinder constraint, and the desire to study both of the basic flow types described in the previous section with a single apparatus. As only the central cylinder rotates, the outer fluid annulus constitutes an inner boundary rotating flow, and the inner fluid annulus gives an outer boundary rotating flow.

The above design provides this flexibility at low cost since no elaborate seals or bearings need be immersed in the working fluid. This last feature contributes much to the overall advantage of this design since three different working fluids are used which no single set of seals could accommodate.

The fixed central spindle and base plate were machined from stainless steel as is the rotating chuck which rides on sets of thrust and roller bearings pressed onto the spindle. The plexiglas cylinders were precision machined and polished. The outer fixed cylinder is mounted on a stainless steel base plate and the central rotating cylinder is mounted in the chuck with adjusting screws for alignment. The rotating cylinder is aligned and balanced in place. Baffles cut from teflon suppresses irregular end disturbances. Total runout due to machining and alignment flaws is less than two thousandths of an inch up and down the full span of the annuli. The central cylinder is turned with a variable speed synchronous AC motor with a frequency variable synthesized three-phase controller. Timing belts and pulleys are used. Cylinder rotation rates are stable against long term drift to ~ 0.01 percent (i.e., drifting by no more than $\sim 2\pi$ in 10^4 rotations). Periodic speed fluctuations are observed during a single rotation of ~ 0.1 percent. The Reynolds number ranges accessible to this apparatus using three working fluids is summarized below in Table 5.

THIS

PAGE

IS

MISSING

IN

ORIGINAL

DOCUMENT

translation stage. The surface of the stainless steel inner cylinder was black-passivated to eliminate specular reflections form its surface.

The vorticity components measured in this geometry and their relationship to the flowfield are indicated in the figure. Explicitly, the standard VOP primed basis is related to the cylindrical coordinate vorticity components $(\omega_z, \omega_\theta, \omega_r)$ by

$$\omega_z' = \omega_z$$

$$\omega_z' = -\frac{1}{\sqrt{2}} (\omega_o + \omega_r) = \omega_s \qquad (36)$$

$$\omega_y' = \frac{1}{\sqrt{2}} (\omega_\theta - \omega_r) = \omega_n$$

where ω_s and ω_n are the components in and normal to the plane of the principal axis of the rate-of-strain tensor, respectively. The component ω_s in this plane should thus experience the most rapid stretching and consequent intensification.

5.2.1 Transition to Turbulence in P-cymene

Probability density functions (PDFs) of two vorticity components for the outer boundary rotating flow are presented in Figure 29(a) through (d). Starting at 1 Hz rotation rate (a) (cylinder surface speed of 28 cm/s) and increasing by factors of 2 up to case (d) at 8 Hz (surface speed 2.25 m/s) where the boundary layer appear to be fully turbulent. (Some residual intermittency may persist at this Reynolds number ~ 25,000 as indicated in Figure 26(b) but a laminar peak is difficult to distinguish against the background turbulence.) Figure 30(a) through (c) are flow visualization photographs corresponding approximately to the 1, 4, and 8 Hz cases. The flow visualization particles have been introduced into the inner fluid annulus only. Figure 30(a) is the purely laminar case. Figure 30(b) show the formation of fine-grained turbulent zones which migrate through the flowfield. In Figure 30(c) the turbulence has essentially filled the inner fluid annulus.
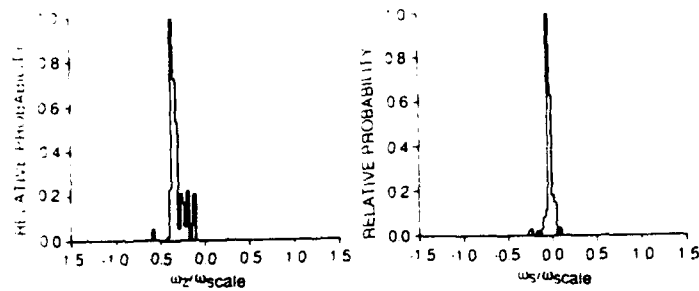
(a) 1 Hz, $\omega_{scale} = 150 \text{ s}^{-1}$, $R_o = 2.5 \times 10^4$
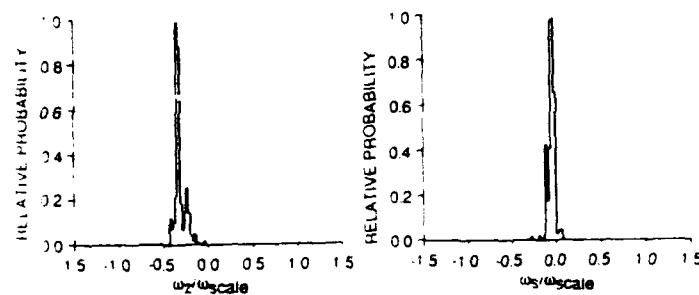
(b) 2 Hz, $\omega_{scale} = 300 \text{ s}^{-1}$, $R_o = 5 \times 10^4$
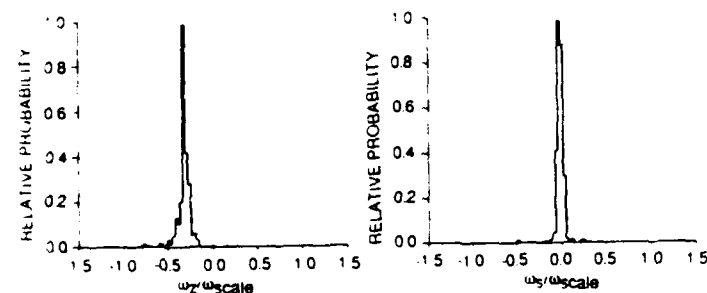
(c) 4 Hz, $\omega_{scale} = 600 \text{ s}^{-1}$, $R_o = 10^5$
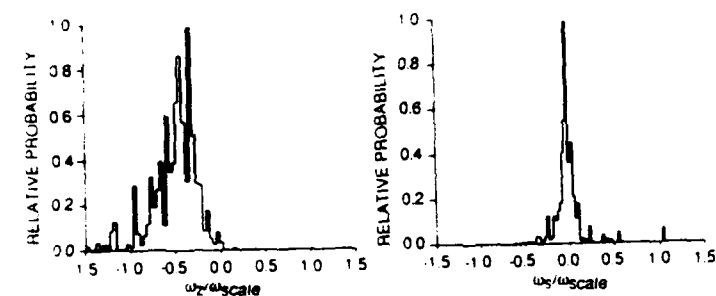
(d) 8 Hz, $\omega_{scale} = 1200 \text{ s}^{-1}$, $R_o = 2 \times 10^4$

B 5793a

Figure 29

Transition to Turbulence in P-Cymene Outer Cylinder Rotating

88

(a) 1 Hz, R_o = 3200: laminar   (b) 4 Hz, R = 12,500: intermittent turbulence   (c) 8 Hz, R = 25,000: fully developed turbulence
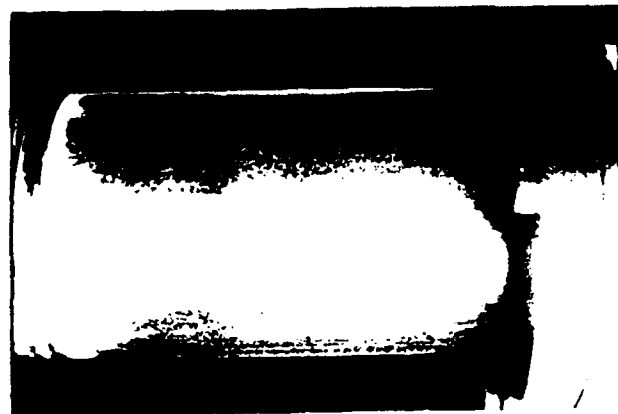
V 504

Figure 30

Outer Cylinder Rotatom Flow Visualization

In Figure 29, the PDF vorticity axes have been scaled exactly with the increasing rotation rate, in order t

visual comparison will convey the constancy of $\delta\omega/\omega$ up to the strong transition to turbulence at 8 Hz. T

$\omega_\gamma(=\omega_n)$ distributions are not included since the instrumental breadth of these distributions dominates th

turbulent fluctuations. This is not to say, however, that the mean values and second and higher moments

be obtained from these distributions. The question will be examined in the next section (Subsection 5.2.2

below).

There is some evidence at low speed (1 and 2 Hz) of particle pairing as was noted in Chapter 4. Howev

4 Hz, the characteristic side lobes have been reasonably suppressed. This can be interpreted as good evi

that weak intermittent turbulence is an adequate mechanism for disrupting stable pairs, and it follows tha:

developed flows are unlikely to have significant pair populations.

5.2.2 Vorticity Statistics and Profiles

Table 6 contains the statistical parameters which can be extracted from these data with some confidence.

each rotation rate, the vorticity scale, the Reynolds number, the distance from the inner (stationary) cylir

which the measurements were made, and the corresponding laminar vorticity (from Eq. (35)) are provide

Note that the number of measurements in each PDF is not large. The error in the second moments is of

$\Delta\omega_i/\sqrt{N}$, or ~5 to 10 percent for these data. Because of the inefficient nature of the current data acqu

and reduction procedure, several hours and 30 to 40 data sets are required to generate a few histograms

those in Figure 29, though the data is collected for each set in a matter of seconds. (A new system, cur

the design stage, will acquire data and process vorticity data in real time.) For the conditions specified i

table the component mean vorticity $\bar{\omega}_i$, rms fluctuation $\Delta\omega_i$ and an estimate of the rms instrumental broa

based on the error distributions, $\delta\omega_i$, are given. Instrumental broadening scales with rotation rate as expe

The widths of the z, s, and n components of vorticity can be seen to be accounted for by instrumental n

until the onset of intermittent turbulence at 4 Hz. Turbulent fluctuations then apparently dominate the ω

Table o. Vorticity Statistics for the PDFs of Figure 29.

Ω Hz	measure	R	σ(cm)	No of Measurements	$\omega_{Z,laminar}$	z			s			n		
						ω_z	$\Delta\omega_z$	$\delta\omega_z$	ω_s	$\Delta\omega_s$	$\delta\omega_s$	ω_n	$\Delta\omega_n$	$\delta\omega_n$
1	150	3200	0.07	138	-55	-46.6	13.2	11.6	4.4	8.3	7.1	6	120	96
2	300	6400	0.03	224	-110	-91.7	18.5	18.3	9.4	12.6	13.6	17	160	167
4	600	12.500	0.03	262	-220	-191	54	29.5	2.2	37.5	20.0	9.8	287	294
8	1200	25,000	0.03	443	-440	-608	325	76	0.7	222	56	104	931	750

distribution widths. This is not so in the case of ω_n, however, where instrumental noise continues to dominate. At this level of statistics (N), estimates of the turbulent contribution to the second moment

$$(\Delta\omega_n)^2 - (\delta\omega_n)^2$$

are unreliable and very sensitive to the estimate of $\delta\omega_n$. The same may be said for higher moments, i.e., skewness and flatness factors, for the PDFs of ω_z and ω_s . To obtain the flatness of the ω_z distribution to < 10 percent accuracy would require two orders of magnitude increase in the volume of data.

Mean and fluctuating vorticity profile data, normal to the inner cylinder surface, was also obtained only at a few points at or below 8 Hz. The normal y coordinate will always be referred to the stationary boundary. The mean vorticity profile and rms fluctuations are shown in Figure 31. No significant variations in the vorticity across the boundary layer were observed for laminar cases (2 Hz data is shown) which maintained their Couette flow values at all stations. For the turbulence case (8 Hz) the rapid increase of mean vorticity $\bar{\omega}_z$ near the wall is clear indication of the development of boundary layer type turbulence. Very little data on this flow is available in the literature (e.g., Taylor,1936, Coles,1965 and Reichardt,1956). Near the inner wall, however, the flow is quasi-parallel and centripetal accelerations vanish. The flow in this region should behave much like a boundary layer in turbulent channel flow.

91
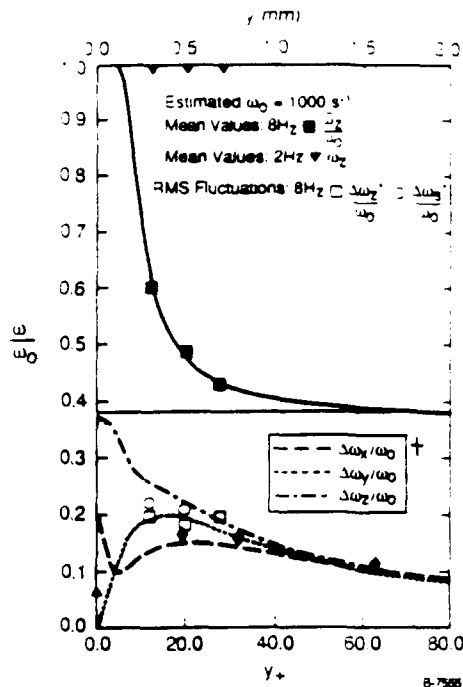
* Corrected for instrumental and gradient broadening
† From Kim, Moin, and Moser (1987)
♦ w_x from Kastrinakis and Eckelmann (1983)

Figure 31

Comparison of Measured Couette Flow Vorticity Statistics with
Turbulent Boundary Layer Computations and Data

On this assumption, the law-of-the-wall vorticity profile was superposed upon a uniform background vorti

Assuming a symmetric vorticity distribution across the flow (which is not strictly true, e.g., Taylor, 193(

discussion of Reynolds number dependence below) the $\bar{\omega}_z$ profile data was fit to the proposed vorticity

distribution with the constraints that: 1) the estimated (y) integral of mean z vorticity across the flow was

to the known outer boundary velocity (2.25 m/s); and 2) that y was non-dimensionalized in the usual way

$$y_+ \text{ by } \frac{u^*}{\nu} \left(= \sqrt{\frac{\omega_0}{\nu}} \right), \text{ where } \omega_0 \text{ is the mean spanwise vorticity at the inner wall } (y=0).$$

The best fit was obtained for estimated $\omega_0 \sim 1000 \text{ s}^{-1}$ and the mean background vorticity $\sim 360 \text{ s}^{-1}$, and

plotted in the figure.

92

Because of the finite width of the laser beam (150 μm or about 6 y_- units for the above data), regions of substantial spatial vorticity gradients produce an additional broadening (of $\Delta\omega_z$ in this case). From the estimated slope of the mean ω_z profile, and the known width of the gaussian beam profile, a simple subtraction of the estimated gradient broadening suffices to correct $\Delta\omega_z$. Based upon the arguments of Chapter 3 and the measured error distributions of the vorticity components, estimates of the widths of the vorticity resolution functions $\delta\omega_i$ were derived, ignoring the variation with vorticity. The true rms fluctuations are obtained from the difference of the squares of the measured rms values and the instrumental noise, $\delta\omega_i$.

The rms vorticity fluctuations, when corrected for both instrumental and vorticity gradient broadening, show qualitative agreement with turbulent boundary layer data. The direct numerical simulations of Kim, Moin, and Moser (1987) for example, from which the rms vorticity curves are taken, agree with the measured $\dfrac{\Delta\omega_z}{\omega_0}$, at least to edge of the buffer layer ($y_- \sim 40$). These data are also consistent with the hot-wire vorticity of streamwise vorticity of Kastrinakis & eckelmann, and the 9-wire hot-wire measurements of Balint, et al. Beyond this point the Couette values are likely to be greater due to the large mean shear away from the wall. The $\Delta\omega_s$ values are more interesting. They appear to be larger than both the $\Delta\omega_z/\omega_0$ and the curves predicted by the simulation. This should not be surprising, however, since $\omega_s \left(= \dfrac{1}{\sqrt{2}}(\omega_x + \omega_y) \right)$ lies in the plane of the principal axis of the rate-of-strain tensor, where the vorticity fluctuations due to vortex stretching are anticipated to be most intense.

These comparisons are quite sensitive to the estimate of ω_0. Further the argument employed to fit the data to the law-of-the-wall plus background vorticity is tenuous. With increasing Reynolds number the Couette flow vorticity profile appears to become increasingly asymmetric and the integrated vorticity near the inner wall will bear no simple relationship to the outer boundary velocity. A more detailed profile is required. More extensive measurements at $R_0 = 32,000$ are presented below.

5.2.3   Three-Component Vorticity Fluctuations near the Wall

At 10 Hz outer boundary rotation rate, corresponding to $R_o = 32,000$, two profiles were obtained: the $\imath$ with counterclockwise rotation so that the most accurately measured components are ω_z and ω_s in the no of Figure 28, and the second with the rotation in the opposite sense, so that in the same vop geometry th accurately measured components were w_z and w_n. Thus the mean and fluctating values of three orthogo. vorticity components could be accurately obtained without greatly increasing the number of data points r

The profile data for the mean spanwise vorticity, $\dfrac{\overline{\omega_z}}{\omega_o}$, and the rms fluctuations $\dfrac{\Delta\omega_z}{\omega_o}$, $\dfrac{\Delta\omega_s}{\omega_o}$, $\dfrac{\Delta\omega_n}{\omega_o}$ in and n components are shown in Figure 32. These values have seen normalized by the measured wall v $\omega_o = 975\ s^{-1}$. The beam waist for this data was ~ 100 μm corresponding to 4.6 y_+ unit. The rms flu
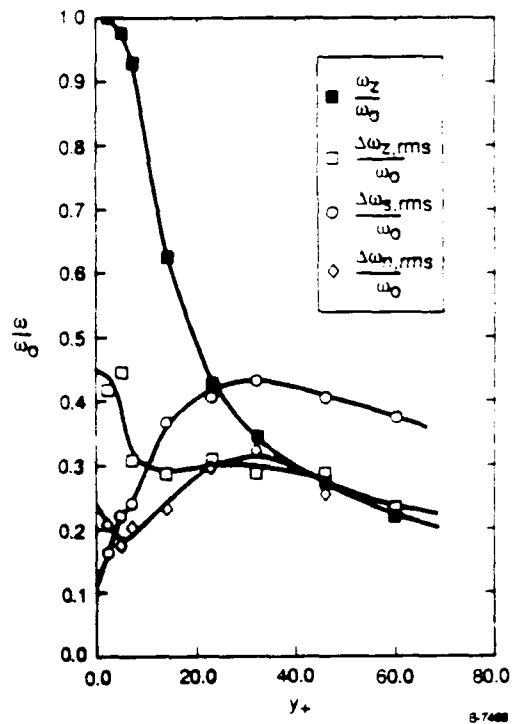
Figure 32

Profiles of Mean Spanwise Vorticity $\dfrac{\overline{\omega_z}}{\omega_o}$ and rms Fluctuations

$\dfrac{\Delta\omega_z}{\omega_o}$, $\dfrac{\Delta\omega_s}{\omega_o}$, $\dfrac{\Delta\omega_n}{\omega_o}$ for 10 Hz Outer Boundary Rotation ($R_o = 32,000$)

have been corrected for instrumental noise and gradient broadening as described above. This figure combines the z data for the clockwise and counterclockwise rotation which were found to be in agreement within experimental error as expected, except for the change of algebraic sign. The mean values of the other components are zero within experimental error.

The mean spanwise vorticity profile is clearly boundary layer-like. The scaling is no longer in doubt since measurements of mean wall vorticity were performed deep within the viscous sublayer ($y_- \approx 2.3$). At $y_- < 10$, the fluctuating vorticity statistics show good agreement with the simulatins of Kim, et.al, though it must be remembered ω_ζ and ω_η represent a 45 deg rotation of the ω_x, ω_y basis in the simulations. Neither $\Delta\omega_{s,rms}$ nor $\Delta\omega_{\eta,rms}$ should tend to zero at the wall, as is required of $\Delta\omega_{y,rms}$ since all x and z spatial derivatives are identically zero at the wall. The expected persistance of strong vorticity fluctuations beyond $y_- \sim 40$ due to the non-zero background shear, is observed. The vorticity fluctuations in the plane of the principal axis of the rate of strain tensor, $\Delta\omega_{\zeta,rms}$, are profoundly amplified well beyond $y_- = 40$, which in a boundary layer would be the logarithmic region. The could be taken as confirmation of the numerical observations of Rogers and Moin (1987), that all turbulent shear flows should exhibit strong vortical concentrations inclined at $\sim 45°$ to the mean flow direction, in the direction of the principal strain. The near equality of spanwise and normal fluctuations is also consistent with their observation in direct numerical simulations, that vortex filaments (those distinguishable from the background) under compression tend to "buckle" and turn, rather than weaken. This level of detail within the sublayer has never before been observed due to serious question regarding accuracy (Taylor's hypothesis) and spatial resolution.

These values are generally larger than those measured by in channel flow by Balint et al. (1987) using the 9-wire hot-wire probe. While it is difficult to compare these flows directly, it seems clear that the vorticity optical probe performs admirably under the worst conditions, i.e., high Reynolds number, near wall, etc. The questionable nature of Taylor's hypothesis in turbulent shear flows, particularly in the wall region (Piomelli et al., 1989; and Champagne, 1978) further enhances confidence in the VOP which does not depend upon Taylor's hypothesis in any way.

95

The PDFs up to now have been treated as one-dimensional. In fact, they are projections of the measure vorticity vectors onto selected vorticity basis vectors. Since the components are measured simultaneously possible view the projections of vorticity vectors onto selected planes, forming two-dimensional joint These then represent the probability of finding a vortex filament or tube, or just random background, w particular angle of inclination in the plane. In a manner analogous to the quadrant analysis of the Reyn stress, Willmarth and Lu (1972), such vorticity maps could potentially lead to a more quantitative under of coherent structure, in particular, "coherent vorticity" (Hussain, 1986). For the turbulent case at 8 H. two-dimensional PDFs are presented as scatterplots in the $\omega_z.\omega_s$ plane at two locations in the flow.

Figure 33(a) is the $\omega_z.\omega_s$ scatterplot at y_+ = 12, and Figure 33(b) at y_+ = 28. Although the statistics poor, the distinctly different character of these planes is clear. At y_+ = 12 the transverse fluctuation in strong as expected and large vorticity excursions appear to be forming a pattern, which is not quite disc At y_+ = 28, however, even at this level of statistics, a pattern is emerging which has been emphasized dotted triangle.

(a) y_+ = 12

(b) y_+ = 28

Figure 33

ω_z, ω_x Scatterplots

96
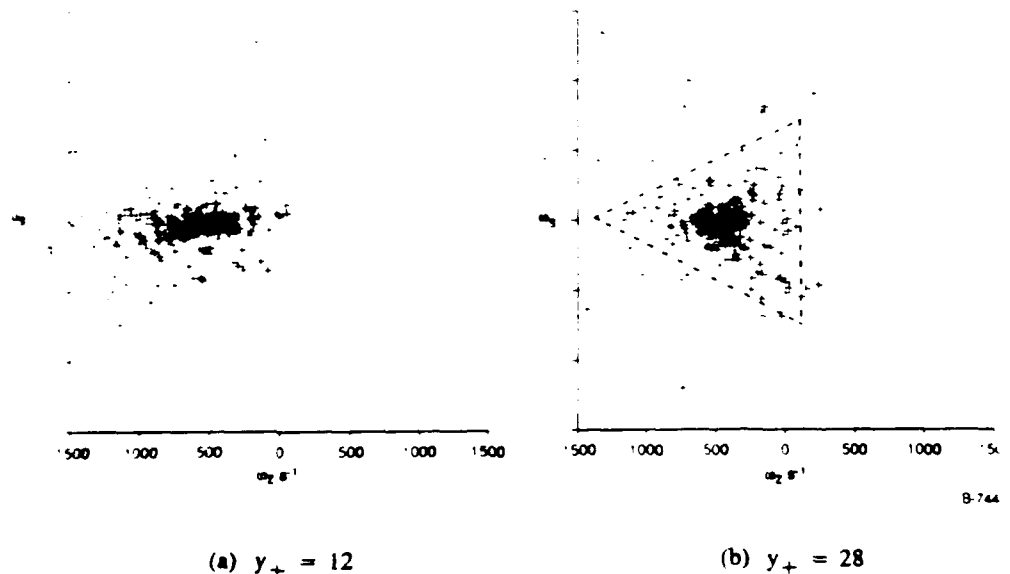
For the case of the 10 Hz rotation rate, the joint PDFs of the profile data are shown in Figure 34(a) and 34(b) as scatterplots in the $\omega_z.\omega_s$ plane and $\omega_z.\omega_n$ plane respectively. Again, a pattern emerges which is not evident from the profiles in Figure 31. Two significant features stand out in these joint PDFs: 1) Aside from the mean flow core which is becoming more symmetrical, there is a distinct tendency for large streamwise (ω_s) excursion to have small spanwise excursion, and vice-versa. This suggests the symmetrical bending and amplification of vorticity for reasonable fraction of the sample data. This is consistent with the counter-rotating vortices of the hairpin vortex model, particularly in the $\omega_z.\omega_s$ plane though it is not discernable whether the vortices occur in spatially contiguous pairs; and 2) There is also the smattering of very intense activity scattered about the $\omega_z.\omega_s$ plane near y_+ that is not as pronounced elsewhere. Little can be made of this at this stage (e.g., in terms of filament pairing as in Pumir and Siggia, 1987) without vastly improved statistics over a much larger domain. It appears, however, that a large contribution to the vorticity fluctuations is associated with isolated, intense vorticity concentrations. Higher moments are needed at higher Reynolds number. The VOP may be uniquely suited to this task.

Other auxiliary data types might prove interesting in some applications. From the discussion in Subsection 3.4, it will be recalled that the χ_ν^2 goodness-of-fit parameter is sensitive to angular acceleration, i.e., $\dfrac{\partial \overline{\omega}}{\partial t}$, interpreting this as an error in the vorticity measurement. But since instrumental errors can be largely accounted for by the procedures outlined in previous chapters, this fluid dynamically driven feature should appear as a residual error which can be characterized. Recall that under the action of a straining field e_{ij} an aligned vortex filament will intensify as

$$\frac{\partial \omega_i}{\partial t} \propto \omega_i \cdot e_{ii} \quad . \tag{37}$$

This should appear as an "acceleration tail" in the χ_ν^2 distributions, recalling the discussion pertaining to Eq. (26) in Subsection 3.4.3. Figure 35(a) and (b) are the χ_ν^2 distribution for the 2 Hz laminar data, and the 8 Hz, $y_+ = 28$ data respectively. Some information on both the strength of the filament and the local strain rate mey be accessible in this way.

97

2 Hz
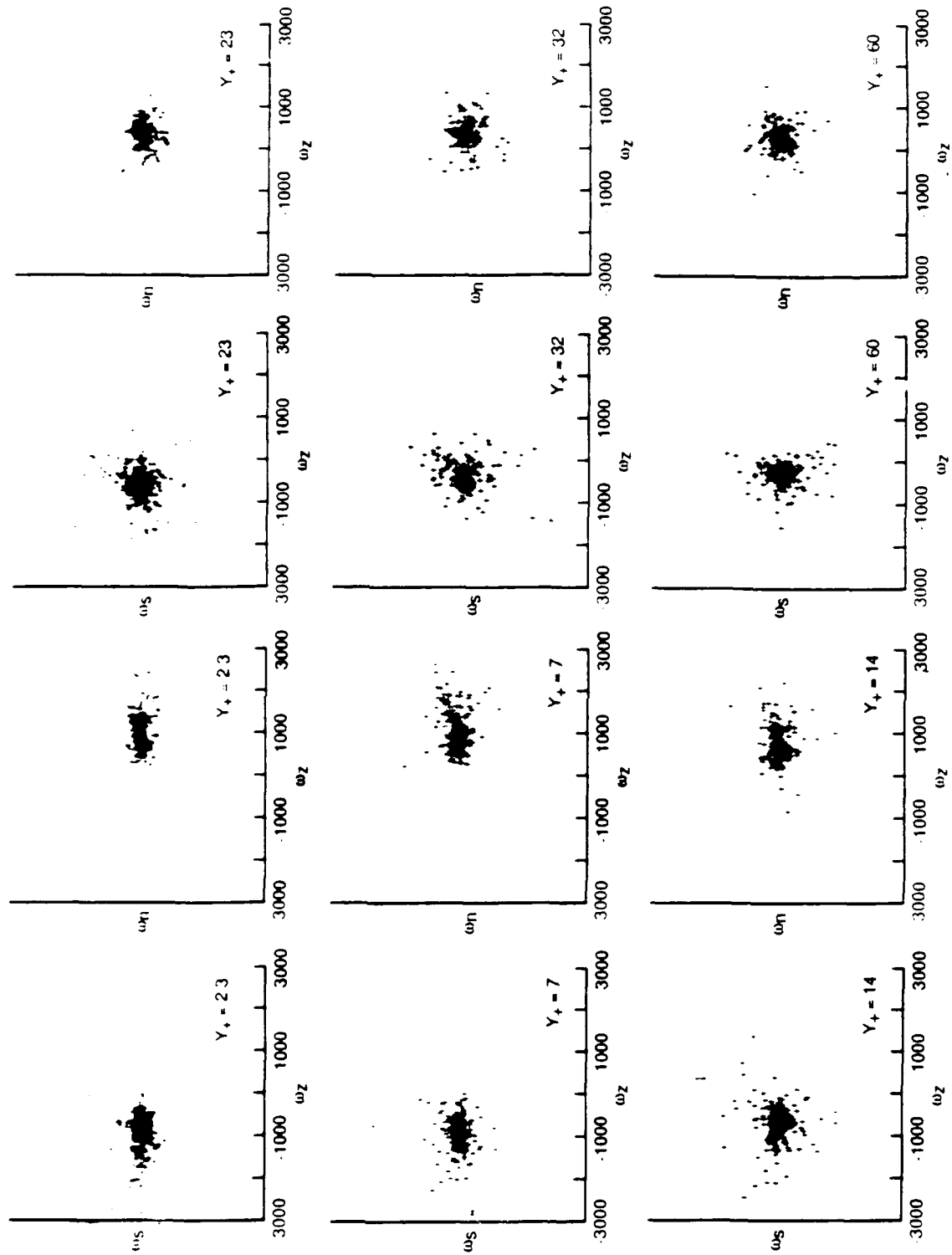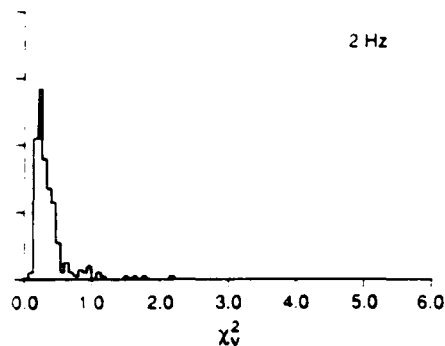
(a) 2 Hz . R = 6400: χ_ν^2 distribution reflects uniformly good fits.

8 Hz
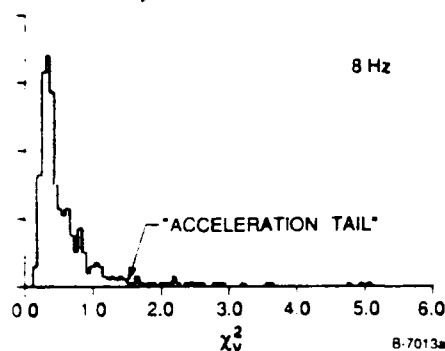
—"ACCELERATION TAIL"

(b) 8 Hz, R = 25,000: Turbulent accelerations give apparent degradation in goodness-of-fit

Figure 35

χ_ν^2 Distributions for Laminar and Turbulent Flow.

The elucidation of spatial and temporal vorticity structure is considered in the following sections describing

measurements in the inner boundary rotation regimes of Couette flow.

5.3 Inner Cylinder Rotation Data in Water

We return now to the R_i axis of Figure 26(a). The flowfield with inner boundary rotation is of fundamentally

different character as described in Subsection 5.1. It is inherently unstable and viscosity inhibits the breakdown

of flow until a critical Reynolds number R_c, is exceeded. The subcritical constant vorticity flow data has

already been presented in Section 4. Those measurements, as well as the remaining measurements described in

the following sections were performed in water, using the new acrylamide probe particles.

99

For these measurements performed near the wall of the outermost (stationary) boundary, we return to th

configuration of Figure 9 in Chapter 3. Thus the relationship between the primed VOP vorticity basis v

and the local flowfield cylindrical coordinates is $\omega_{z'} = \omega_z$, $\omega_{y'} = -\omega_r$, and $\omega_{x'} = \omega_\theta$, which is usually (

in which most computations are performed in Couette flow simulations (e.g., Marcus (1984)). Because (

angles of optical entry and exit in this configuration, all of the index-matching techniques discussed in S(

were employed at the optical interfaces, including an index-matched molded window section (PDFOMA

an acrylamide gel prism. The entire optical train, including the incident beam-steering optics, was mour

micrometer driven translation stages, so that any point in the flow field was reproducibly selectable, part

up and down the span (z-direction). The gel prism simply slides up and down the span with the optics.

5.3.1 Wavy Vortex Flow

Flow visualizations at three supercritical Reynolds numbers are shown in Figure 36. Figure 36(a) shows

standard stationary Taylor-Couette rolls at $R_i/R_c \approx 1.1$. These rolls have stationary inflow and outflow

boundaries corresponding to the positions where the streamwise vorticity (ω_θ) changes sign. The photogr

Figure 36(b) is $R_i/R_c \approx 1.5$. This is near the onset of the wavy-vortax regime, where the Taylor couel

exhibit periodic azimuthal traveling waves. Figure 36(c), at $R_i/R_c \approx 5.0$, still in the wavy-vortex regime

a disturbance in the flow due to change in azimuthal wavenumber propagating up the span as the flow s(

into a stable state.

The value of R_c for this system is ≈ 127. For water at 25°C, $R_0/R_c = 5$ corresponds to an inner boun

rotation rate of 0.35s Hz which lies squarely in the wavy vortex regime. This is a convenient starting p(

series of vorticity measurements since the amplitude of the vorticity fluctuation are strong relative to the

and yet this is sufficiently far from the quasi-periodic regime to minimize possible flow irregularities. A

period of time the flow settled into one of several preferred states (Coles, 1965) where it remained stabl

thereafter. If the flow was stopped during the course of the experiments, great care was taken to insure

upon restart it reached the same final state. This proved to be difficult since the azimuthal wave states a

number of spanwise rolls (which are rather degenerate at large height/gap) must be reproduced. Figure

(c)$R_I/R_c \approx 5$: Wavy-vortex Flow

(b)$R_I/R_c \approx 1.5$: Wavy-vortex Flow
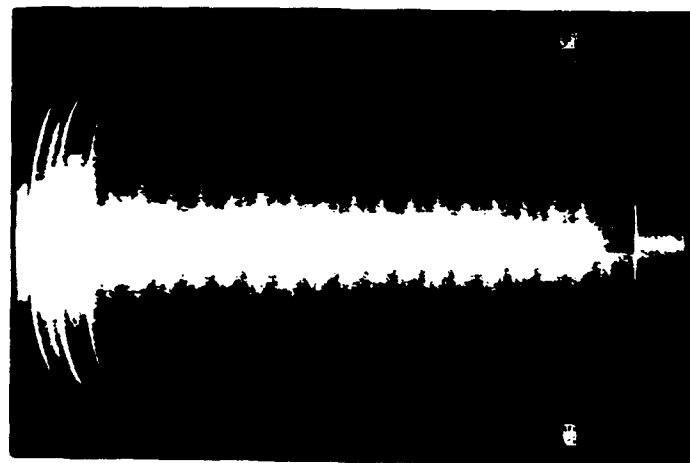
(a)$R_I/R_c \approx 1.1$: Taylor-Couette Rolls

V-505

Flow Visualization Photographs for Inner Boundary Rotation

the flow visualization photo at $R_i/R_c = 5$, has not yet reached a stable state, showing a pronounced irreg

When the flow had settled in to 7 azimuthal traveling waves and 15.5 waves (31 Taylor vortices) on the

vorticity measurements were performed at 8 Hz station at a depth of $y = 0.1$ g (one-tenth of the gap) fro

outer boundary. The wavy-vortex period for this state was measured to be 1.357s, and the spanwise ·

wavelength, $\chi = 1.4$ cm. Figure 37 is the measured mean vorticity components versus z/λ. Again, for

hundred points, the uncertainties in the values of $\bar{\omega}_z$ and $\bar{\omega}_x(=\bar{\omega}_\theta)$ are a few percent, but the uncertainty

$\bar{\omega}_y(=\bar{\omega}_r)$ is comparable to its value.

Since the time at which the individual data points are recorded is also logged, sparsely and randomly san

periodic data can be used to reproduce the temporal signature of the (vorticity) wave. Figure 38 is singl

of ~50 points acquired in just over 90 seconds. Thus the mean sampling rate is less than the period. B

of the accurately measured, stable wave period, however, the time behavior of the vorticity during a siņ

cycle can be reconstructed by folding the record, modulo-τ into a single cycle. (It is preferable to avoid

situation through, by sampling adequately in the first instance.) Figure 39 is a 'synthetic' time history o:

wavy vortex. The trend is clear though a bit noisy. There is a distinct phase relationship between the

components which cannot be easily interpreted with extensive flowfield mapping.
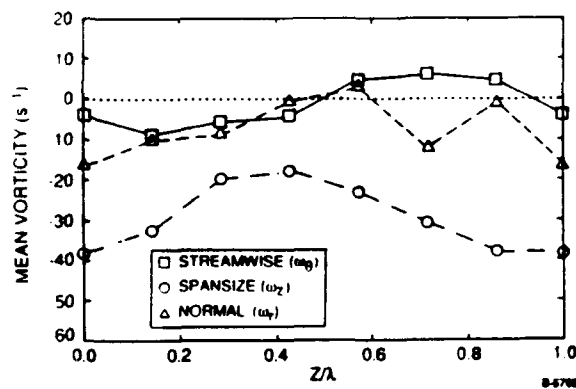
Figure 37

Wavy Vortex Spatial Vorticity Structure ($R/R_c = 5$, 7 wave azimuthally and 15.5 on the span)
Spanwise variation of mean vorticity component values near the wall,
over one spatial wavelength of wavy vortex flow $y/g = 0.1$, $\lambda \approx 1.4$ cm

102
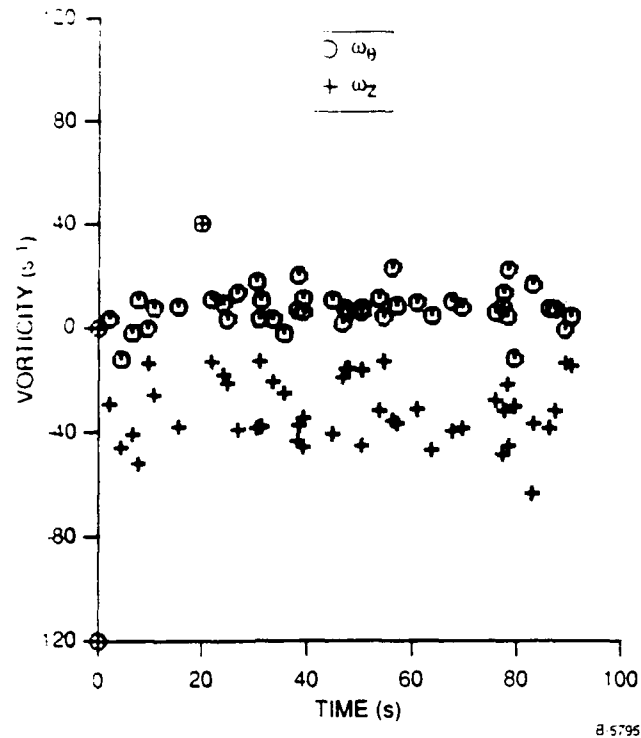
Figure 38

Wavy Vortex Flow (water) Vorticity Versus Time Sample Record
- In data collected over 2 min interval, no periodicity is visible
- Wavy vortex period, τ, measured 1.347s (viewing image plane)
  - Mean sampling period ~2s

This method is reminiscent of the phase averaging procedures used in the eduction of coherent structures by conditional sampling. In this case, the problem is a rather trivial one since the data is periodic and the phase information can thus be stored along with the data. Some phase jitter may be present in the data due to incipient instabilities. The 7 azimuthal wave flow at $R_i/R_c = 5$ appears to be only barely stable, owing perhaps to vibration or other flow irregularities. A Reynolds number, the 7 azimuthal wave flow, is not expected to be stable. Since the flow is essentially laminar, pair interactions have not been ruled out as additional sources of noise. Finally, at the outflow boundaries (near reduced time=0) where the vorticity is large, the velocity may be larger still, resulting in reduced $\frac{|\omega|}{|U|}$ and thus reduced precision in vorticity measurement. The size of the error bars (rms distribution widths, not shown) associated with the points in Figure 39 vary systematically

103
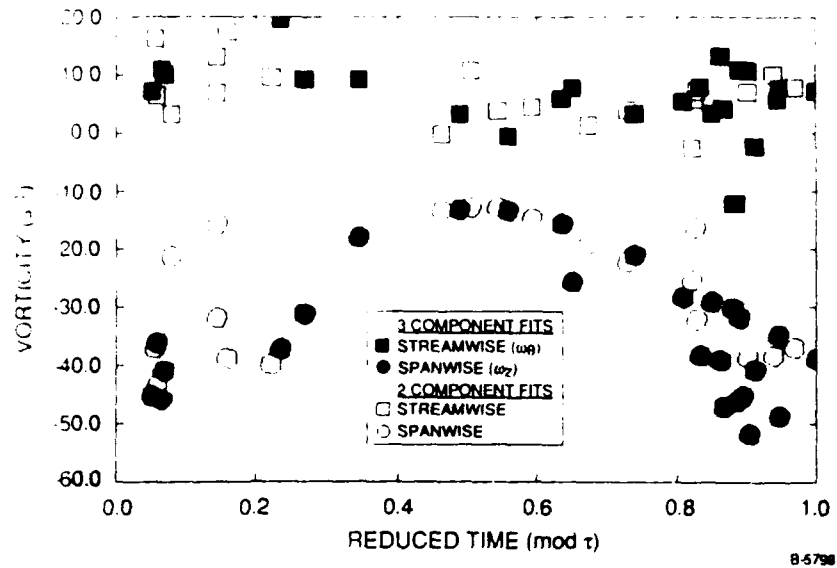
Figure 39

Wavy Vortex Periodogram (R/R$_c$ = 5, 7 azimuthal waves, τ = 1.347)

across the figure with the minimum near the center. This sampling bias, which is also periodic, is likel

affect the mean vorticity profiles, particularly for ω'_y. Correction strategies have been discussed in Ch.

The temporal autocorrelation is defined as

$$\Phi_{ii}(\tau) = \frac{\int_{-\infty}^{\infty} \omega_i(t)\omega_i(t+\tau)dt}{\int_{-\infty}^{\infty} \omega_i^2 dt}$$

Autocorrelations for discrete random data have been described by Frish (1981) and others and will not h

recounted here, except to note that the time axis is simply divided uniformly into bins of sufficient widt!

obtain reasonable statistics in each bin (properly normalized including statistical weights) and still insure

adequate time resolution. A necessary refinement of discrete auto-correlations for finite time events is t

time weighting (Buchhave, et al., 1979), which is the auto-correlation anaolog of transit time weighting

uniformly spaced bins are then suitable for Fourier transformation in order to estimate the power spectn

the random signal. This process has been carried out with the discrete time approximation of Eq. (38) 1

104

ensemble of records like those in Figure 39. Figure 40 is an autocorrelation of ω_z for 8 records (a total of

~400 points distributed over ~80 bins). The reflection symmetry is an artifact of the wrap-around algorithm

employed. While the autocorrelation must be unity at $\tau=0$, the reduced amplitude everywhere else is due to the

partial loss of coherence attributable to uncorrelated noise. A fitted cosine function shows that 65 percent of

Φ_{zz}, or ~80 percent of the rms $\Delta\omega_z$ is in the periodic structure of the signal. (Approximately 40 percent of

$\Phi_{\theta\theta}$, or 64 percent of $\Delta\omega_\theta$, is due to the periodicity.) Figure 41 is the FFT of the autocorrelation which

contains no additional information. It should be noted, however, that with sufficiently long records and

adequate sampling, these power spectra could potentially show as much temporal detail as the velocity records

in the famous study of Fenstermacher et al. (1979). The difference that vorticity vector measurement could

make is that amplitudes and phases of frequency components can be directly associated with the dynamical

variables that drive the flow physics and thus the instabilities.

5.3.2 Turbulent Taylor Vortex Flow

By increasing R_i/R_c an order of magnitude to 50, all vestiges of periodicity in the flow are lost, and

one is well into the turbulent Taylor vortex flow regime. A striking feature of this flow, however, is the

spanwise wave structure, which is clearly visible in the flow visualization photo in Figure 42. At much higher

values, this "coherent structure" still persists, though less visibly, in the presence of intense turbulence.
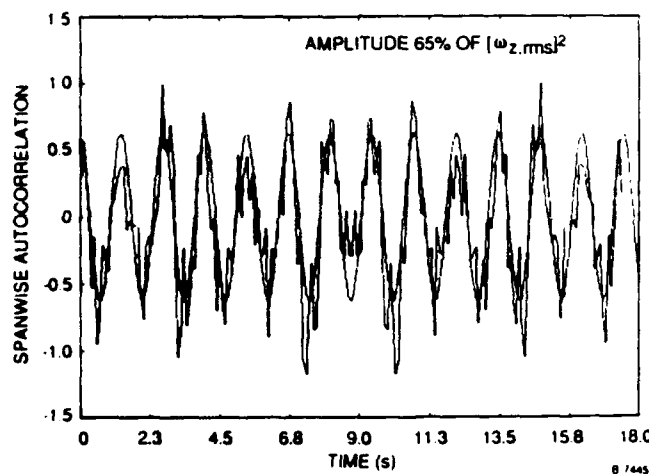
Figure 40

ω_z Autocorrelation for Wavy Vortex Flow ($R/R_c = 5$, 7 azimuthal waves, $\tau = 1.347$s)

105
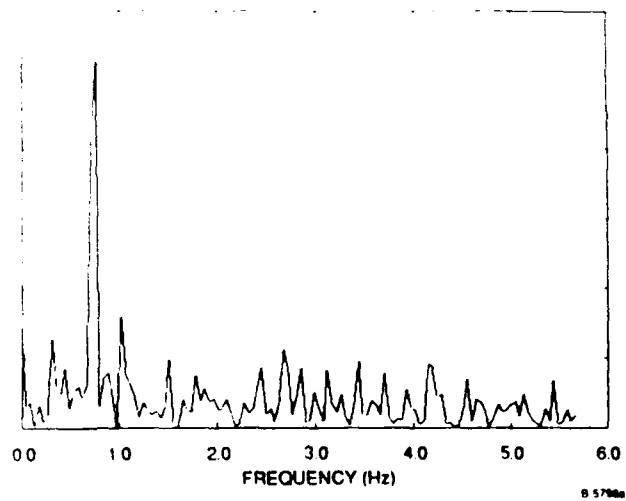
Figure 41

Linear Power Spectrum of Spanwise Vorticity

(from FFT of autocorrelation in arbitrary units)

Figure 42   V-506

Flow Visualization Photograph of Turbulent Taylor Vortices, $R_i/R_c = 50$

106

The $R_1 \cdot R_2 = 50$ spanwise structure is again measured across one spanwise wavelength at $y = 0.1g$. The histograms of these measurements, as well as the ω_z, ω_θ scatterplots, are included as a function of position on the span in Figure 43.

The scatterplots show an alternating pattern of left and right inclined vortex lines near the plane of the wall, which is to be expected from counter-rotating streamwise vortices in the mean flow. The fluctuations, however, seen clearly in the scatterplots, exhibit several interesting features. The spanwise vorticity fluctuations are most intense near inflow and outflow boundaries, (where $\omega_\theta = 0$). Figure 44(a) and (b) are the mean and rms vorticity values for these histograms. The near vanishing of the spanwise vorticity at $z/\lambda \sim 0.7$ is apparently the inflow boundary position, where low speed fluid accumulates at the outer wall. The small values of ω_x and ω_z result in enormous uncertainties for ω_y (noted in the Figure 44(b) as the 'two-component range'). The rms fluctuations normalized by the magnitude of the mean vorticity $|\bar{\omega}|$ are fairly uniform along z, suggestive of relatively homogeneous through highly anisotropic turbulence. Again, detailed flowfield mapping is needed for more definitive descriptions.

At still higher Reynolds numbers, the fluctuations increase dramatically in intensity. A few histograms are shown in Figure 45 at $R_1/R_c = 150$ for the condition indicated in the figure. The vorticity fluctuations in all of the turbulent Taylor-vortex flow data show strong interactions with the local mean flow. The eduction of the prevalent structures as the turbulence accomodates itself to the local flow would be an interesting study.

5.4   Summary of Couette Flow Measurements

Three-component vorticity measurements have been performed in the both outer and inner boundary rotation type Couette flow. Summaries of observations about the structure of the vorticity fields in each of these flows are given below.

107
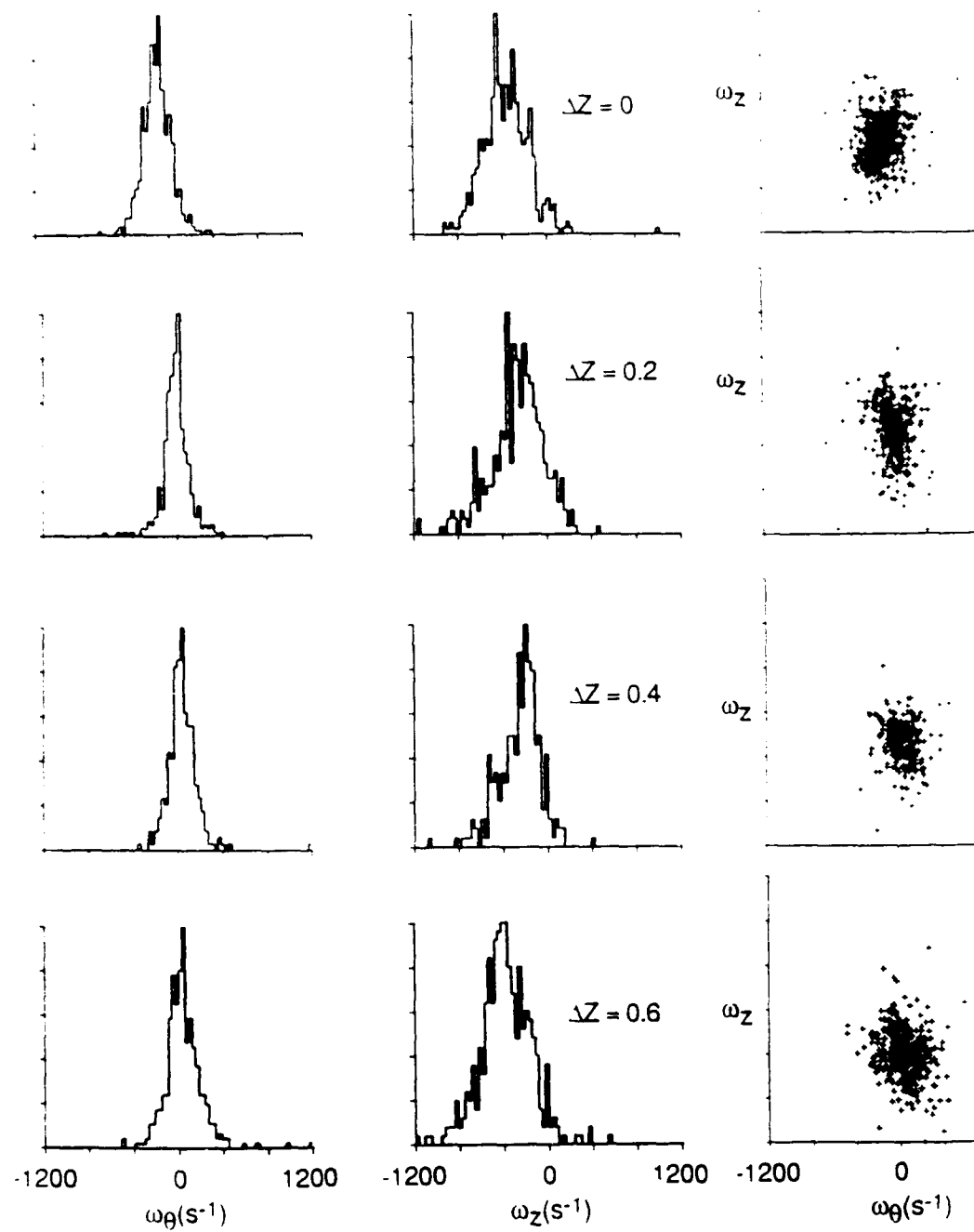
Figure 43

Turbulent Taylor Vortices $R_i/R_c = 50$: Spanwise Profile ($y/g = 0.1$)

108

$\Delta Z = 0.6$

ω_z

$\Delta Z = 0.8$

ω_z

$\Delta Z = 1.0$

ω_z

$\Delta Z = 1.2$

ω_z

$-1200 \qquad 0 \qquad 1200$

$\omega_\theta(s^{-1})$

$-1200 \qquad 0 \qquad 1200$

$\omega_z(s^{-1})$

$-1200 \qquad 0 \qquad 1200$

$\omega_\theta(s^{-1})$
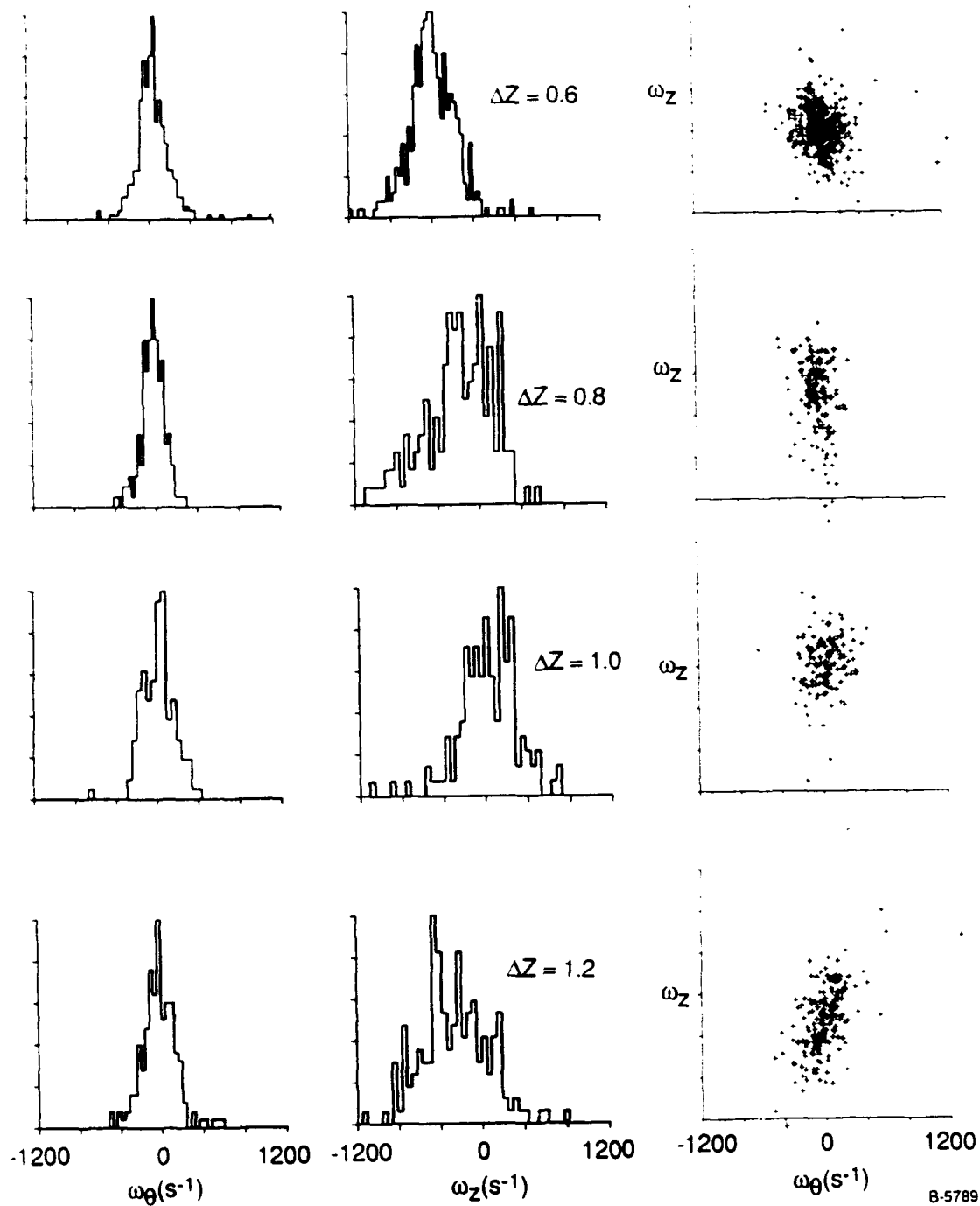
B-5789

Figure 43 (Continued)

Turbulent Taylor Vortices R_i/R_c = 50: Spanwise Profile (y/g = 0.1)

109
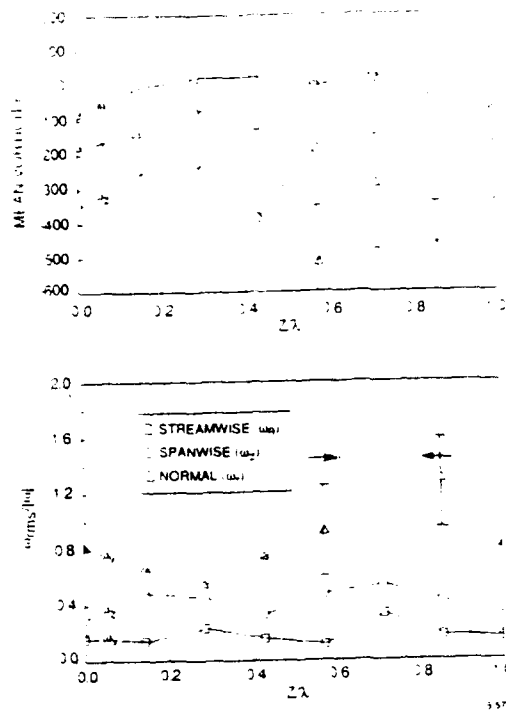
Figure 44

Spatial Variation of Normalized RMS Vorticity Fluctuations Near the Wall:

Corrected for Instrumental Noise
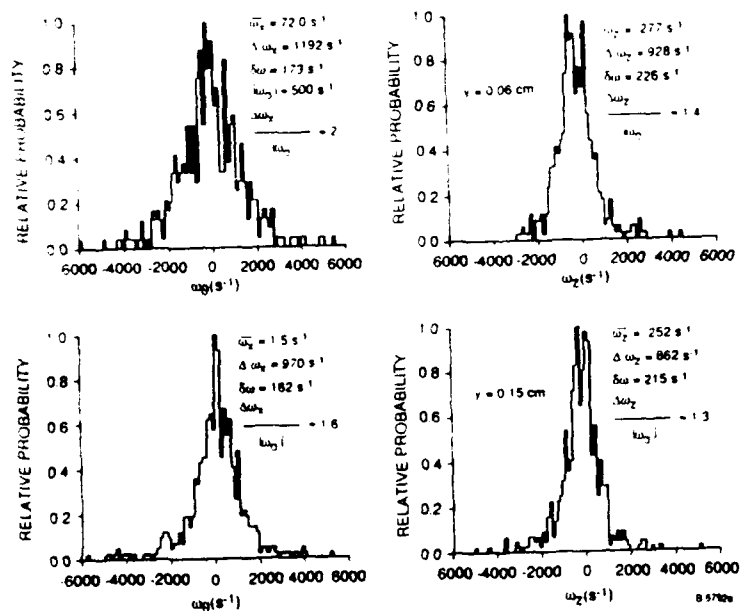
Figure 45

Turbulent Taylor Vortex Flow $R/R_c = 150$

5.4.1 Outer Boundary Rotation

For outer boundary rotation Couette flow, laminar, intermittent, and turbulent vorticity distributions were measured. It was found the laminar Couette flow exhibited uniform vorticity throughout the flowfield, at the values expected from the exact solution of the equation of motion. Intermittent turbulence appeared and was detected at the anticipated Reynolds number. Fully developed turbulence has mean and rms fluctuating vorticity profiles in y, the coordinate normal to the inner stationary bounday, which resemble standard plane-boundary layer turbulence very close to the wall. Farther from the wall, the vorticity fluctuations appear to be dominated by the fluctuating component of vorticity which lies parallel to the principal axis of the mean flow rate-of-strain tensor. Joint probability density functions of the turbulent vorticity show evidence of structures. The z and s component of the vorticity are only weakly correlated, though apprently not independent (Tennekes & Lumley, 1972). It is difficult to distinguish structures from background vorticity, however, and these observations await improved statistics from greater quantities of data for clarification.

5.4.2 Inner Boundary Rotation

The inner boundary rotation experiments served as both a test of the new acrylamide vorticity probe particles in water, and a test of the VOP's ability to distinguish temporal and spatial vorticity field structure in the presence of noise or turbulent flow fluctuations. The laminar inner boundary rotation Couette flow demonstated that the acrylamide particles behave as expected, and also were a clear indication of the particle pairing behavior anticipated in laminar shear flow. This pairing is observed to be significantly disrupted by the presence of turbulent flow fluctuations. The wavy-vortex flow experiments demonstrate the elucidation of spatially and temporally periodic vorticity. These measurements are limited by the currently available maximum record lenth that can be acquired. Unfortunately, this limitation neccessitated skipping over most of the interesting range of Reynolds number where the spectral evolution to turbulence transpires, since several incommensurate frequencies are difficult to resolve without long temporally continous records. Lastly, turbulent Taylor vortex flow exhibits fascinating interactions of the vorticity fluctuations with the mean flow, and deserves further study.

6.1   Summary

A system for simultaneous measurement of the three components of the local, instantaneous vorticity vect
laminar and turbulent liquid flow has been assembled and tested. This system is an extension of the sing!
component Vorticity Optical Probe system developed by Frish and Webb. The most powerful features of
approach to vorticity measurement are its superior spatial resolution, limited only by the size of the probe
particles, and its outstanding performance in high vorticity and low velocity regions without the need to u
Taylor's hypothesis. In this respect, the VOP is very complementary to other velocity-based vorticity
measurement methods. Not only are the three vorticity components measured, any two of them more acc
than the third, but uncertainties in the vorticity components as well. Other useful statistical parameters ar
derived during data reduction. This auxiliary information allows vorticity resolution and sampling functic
he derived as function of experimental parameters. The three-component VOP is 'self-characterizing', in
sense that it measures its own precision as it acquires data.

The VOP is now water-compatible. The invention of a new class of probe particles made of acrylamide
offers the possibility of new, widespread applicability of the VOP, particularly in larger scale, high Reyn
flow facilities. The new acrylamide particles are ideally suited to large scale application, since they are
~ 90 percent water by weight and readily mass-producible at low cost.

The three-component system has been tested in six distinct Couette flow regimes. Laminar, transitional ar
turbulent flows were studied for inner and outer boundary rotation. The laminar flows exhibit the expect
spatially and temporally constant vorticity anticipated from the analytic Couette flow solution of the equat
motion. For inner boundary rotation, the spatial and temporal behavior of the vorticity components the n
outer boundary in wavy-vortex flow at $R_i/R_c = 5.0$ has been measured. Comparisons with recent numer
simulations of this flow compare favorably (Coughlin, 1991). Turbulent taylor vortex flow shows strong
interactions between the fluctuating vorticity and the local mean flow. Outer boundary rotation data at

112

$R_o = 32,000$ (based on gap and surface speed) shows very large spanwise vorticity fluctuations at the wall, > 40 percent, after corrections for instrumental broadening. These measurements also compare well, close to the inner wall, with direct numerical simulations of turbulent boundary layers. Farther from the wall the difference in these flow types becomes evident. The mean background shear in the Couette flow dramatically amplifies the vorticity fluctuations in the s-direction, inclined at 45 deg to the flow direction which is also the principal strain direction. This observation agrees with recent simulations of turbulent shear flow, which suggest that hairpin vortices are an important feature of all turbulent shear flows. Scatterplot representations of joint ω_z, ω_s PDFs show some evidence of intense vortex filaments rotating toward the principal strain axis, though this must be confirmed with further measurements. These measurements show the potential power and versatility of the VOP technique, and invite new approaches to old problems.

6.2   Limitations of the Three-component VOP

As with any fluid flow measurement system, there are a number of fundamental limitations which the single point VOP, by the nature of its operation, can never overcome.

The sense in which vorticity measurements are time-resolved is somewhat different from other types of measurement. The VOP trades off some temporal resolution to 'see' the rotation of the particle-containing fluid element, in order to avoid the loss of spatial resolution which is invariably the price of finite-difference methods of velocity gradient measurement. The vorticity is measured at a probe particle's location which is convecting through the sampled volume. It may move a considerable distance during the measurement, depending on its vorticity and the allowed sampled volume dimensions. This is the sense in which the VOP is 'locally Lagrangian', and the Lagrangian microscale of time is the limiting period for accurate vorticity measurement. Up to this point, this does not really qualify as a limitation. Longer time of observation is required for vorticity of lesser magnitude, but the convection velocity through the sampled volume does not necessarily cooperate. The vorticity/velocity ratio problem and the VOP 'singularity' ($\overline{\omega} || \hat{u}$) are closely related. Short trajectories at finite signal-to-noise are almost invariably interpreted as having large (spurious) curvature, i.e, orbiting about a

113

nearby point, reflecting the indeterminate nature of the $\omega_y{}'$ component at a point. For larger trajectories situation improves rapidly giving a useful measure of this component, albeit with greater uncertainty than others. The vorticity/velocity ratio often drops below the lower limit of usefulness (typically from 0.1 to 1 cm^{-1} depending on the sampled volume dimensions). Here one must either make assumptions about th vorticity field in order to measure low vorticity values (e.g., that it is essentially two-dimensional, which usually a good approximation when fitting only two components near detector center), or put a count in a special bin for near zero vorticity and move on. At the end of the data reduction, if there is a sufficient of counts in this bin, then it may be statistically and fluid dynamically significant, e.g., an irrotational ($\bar{\omega}$ spike in the PDF due to intermittency.

The VOP has sampling limitations. Overlap of finite duration trajectories trajectory are not allowed in the currently used detection scheme. The mean time between trajectories must be at least three times the me detector transit time. This implies an average spacing of the probe particles in the flow, and thus typical the structures that will be resolved. This statement makes the connection between the local Langrangian vorticity measurements and the Eulerian structure of the flow. But here is Taylor's hypothesis is creepin in: the notion the spatial structure can be derived from a time sequence of values of a given quantity at a point in the flowfield is still a subject of debate, particularly in turbulent shear flows. Though the VOP eliminates this controversy for individual vorticity measurements, these questions pertaining to extended structures persist, as for all other single point measurements of flow variables.

6.3   New Measurements. New Methods

As an expansion of single point measurement capability, a second detector could be added, as indicated i Figure 9 in Chapter 3, in order to perform two-component velocity measurements simultaneously with th component vorticity measurements for the same particle in the sampled volume. Instantaneous vorticity- correlations would thus be accessible, including significant $\overline{u}$ and $\overline{u \times \omega}$ contributions and components. T

second detector can be just as easily configured as a second VOP. Two-point spatial vorticity correlation is still a measurement of fundamental importance in the study of coherent structures in turbulence.

Finally, it appears that the VOP must one day go the way of many other measurements--toward multiple point measurements, conditional sampling, (phase average) methods, and ultimately imaging techniques. The photograph in Figure 46 below is of VOP probe particles in a shear flow illuminated by a sheet of laser light. Sequences of bright flashes along the apparent streamlines indicate the presence of vorticity. As the particles rotate, reflections from some enter the camera lens producing a bright spot. Only a time base and a length scale are needed to extract vorticities. The logical extrapolation from these concepts is direct vorticity visualization techniques.

6.4   Closing

Another tool, the three-component water-compatible Vorticity Optical Probe, has now been added to the impressive collection already marshalled in the pursuit of a fundamental understanding of fluid flow. The new VOP is uniquely suited to the problems of high shear, high Reynolds number, non-parallel and near-wall flows that have plagued the experimental fluid dynamics community for decades. It is to be hoped that this new building block will enlarge our knowledge of this most common and most complex phenomenon -- turbulence.

Figure 46. Vorticity Visualization?

7. REFERENCES

Acarlar, M.S. and Smith, C.R. (1987), "A Study of Hairpin Vortices in a Laminar Boundary Layer. Part II: Hairpin Vortices Generated by Fluid Injection." J. Fluid Mech. $\underline{175}$, 43.

Adrian, R.J. (1991), "Particle-Imaging Techniques for Experimental Fluid Mechanics." Ann. Rev. Fluid Mech. $\underline{23}$, 261.

Anders, J.B. and Blackwelder, R.F. (1980), "Longitudinal Vortices in Transitioning Boundary Layer," in Laminar-Turbulent Transition (Eds. R. Eppler & E. Fasel) Springer-Verlag.

Antonia, R.A. (1981), "Conditional Sampling in Turbulence Measurement," Ann. Rev. Fluid Mech. $\underline{13}$, 131.

Aqüi, J.C. and Hesselink, L. (1990), "Application of Holography to the Measurement of Velocity Gradients in Fluid Flows Sensitized with Photochromic Dyes," Phys. Fluids A $\underline{2}$, 688.

Aqüi, J.C. and Jimènez, J. (1987), "On the Performance of Particle Tracking," J. Fluid Mech. $\underline{1875}$, 447.

Aref, H. and Flinchem, E.P. (1984), "Dynamics of a Vortex Filament in Shear Flow," J. Fluid Mech. $\underline{148}$, 447.

Aref, H. and Siggia, E.D. (1980), "Vortex Dynamics of the Two-Dimensional Turbulent Shear Layer," J. Fluid Mech. $\underline{100}$, 705.

Bakewell, H.P. and Lumley, J.L. (1967), "Viscous Sublayer and Adjacent Wall Region in Turbulent Pipe Flow." Phys. Fluids $\underline{10}$, 1880.

Balint, J.L., Wallace, J.M., and Vukoslavčević, P. (1989), "The Statistical Properties of the Vorticity Field of a Two-Stream Mixing Layer," in Advances in Turbulence II, (Eds. Fernholz & Fielder) Springer-Verlag.

Balint, J.L., Vukoslavčevic, P., and Wallace, J.M. (1987), "A Study of Vortical Structure of the Turbulent Boundary Layer," in Advances in Turbulence, (Eds. Comte Bellot & Mathieu) Springer-Verlag.

Batchelor, G.K. (1956), The Theory of Homogeneous Turbulence, Cambridge University Press.

Batchelor, G.K. (1967), An Introduction to Fluid Dynamics, Cambridge University Press.

Batchelor, G.K. and Green, J.T. (1972) "The Hydrodynamic Interaction of Two Small Freely-Moving Spheres in a Linear Flowfield," J. Fluid Mech. $\underline{56}$, 375.

Bendat, J.S. and Piersol, A.G. (1971) Random Data: Analysis and Measurement Procedures Wiley-Interscience.

Betchov, R. (1965), "On the Curvature and Torsion of an Isolated Vortex Filament," J. Fluid Mech. $\underline{22}$, 471.

Bevington, P.R. (1969) Data Reduction and Error Analysis for the Physics Sciences McGraw Hill.

Blackwelder, R.F. (1977), "On the Role of Phase Information in Conditional Sampling," Phys. Fluids $\underline{20}$, 5232.

Brown, G.L. and Rosko, A. (1974), "On Density Effects and Large Structure in Turbulent Mixing," J. Fluid Mech. $\underline{64}$, 775.

Buchhave, P., George, W.K., and Lumley, J.L. (1979), "The Measurement of Turbulence with Laser-Dop Anemometer." Ann. Rev. Fluid Mech. 11, 443.

Busse, F.H., Gollub, J.P., Maslowe, S.A., and Swinney, H.L. (1985), "Recent Progress." in Hydrodynam Instabilities and the Transition to Turbulence, Second Edition (Eds. H.L. Swinney & J.P. Gollub) Springer-Verlag.

Cantwell, B.J. (1981), "Organized Motion on Turbulent Flow." Ann Rev. Fluid Mech. 13, 457.

Chwang, A. and Wu, T. (1974), "Hydromechanics of Low-Reynolds Number Flow. Part I: Rotation of Axsimetric Prolate Bodies." J. Fluid Mech. 63, 607.

Coles, D. (1965), "Transition in Circular Couette Flow." J. Fluid Mech. 21, 385.

Coughlin, K. (1991), U.C. Berkely, Private Communication.

Corino, E.R. and Brodkey, R.S. (1969), "A Visual Investigation of the Wall Region of a Turbulent Flow. Fluid Mech. 37, 1.

Crow, S.S. and Champagne F.H. (1971) "Orderly Structure in Jet Turbulence." J. Fluid Mech. 48, 547.

Darabaner, C.L. and Mason, S.G. (1967), Rheol. Acta 6, 273.

DiPrima, R.C. and Swinney, H.L. (1985), "Instabilities and Transition in Flow Between Concentric Rotat. Cylinders." in Hydrodynamic Instabilities and the Transition to Turbulence, Second Edition (Eds. H.L. Swinney & J.P. Gollub) Top. Appl. Phys. 45, Springer-Verlag.

Donnelly, R.J. and Roberts, P.H. (1974) "Superfluid Mechanics." Ann. Rev. Fluid Mech. 6, 179.

Falco, R.E. and Chu, C.C. (1987), "Measurements of Two-Dimensional Fluid Dynamic Quantities Using Photo-Chromic Grid Tracing Technique." SPIE Photo Mechanics and Speckle Metrology, 814, 7C

Fenstermacher, P.R., Swinney, H.L., and Gollub, J.P. (1979), "Dynamical Instabilities and the Transition Chaotic Taylor Vortex Flow." J. Fluid Mech. 94, 103.

Ferguson, R.D. and Webb, W.W. (1983), "The Vorticity Optical Probe: A Fast Multi-Component Model. Proc. Symp. Turb. 8th, Rolla, Mo.

Ferguson, R.D. and Frish, M.B. (1990), "Water-Compatible Vorticity Optical Probe Particles." Bull. Am. Phys. Soc., 35, 2252.

Fermigier, M., Cloitre, M., Guyou, E., and Jenffer, P. (1982), "Utilization de la Diffusion Rayleigh Forc Al'etude Décoalements Laminaires et Turbulents." J. Mechanique Theor. Appl. 1, 123.

Foss, J.F. and Wallace, J.M. (1989), "The Measurement of Vorticity in Transition and Fully Developed Turbulent Flows." in Lecture Notes in Engineering, 45, Advances in Fluid Mechanics Measurem (Ed. M. Gad-el-Hak) 263.

Frish, M.B. and Webb, W.W. (1981), "Direct Measurement of Vorticity by Optical Probe." J. Fluid Mec 107, 173.

Frish, M.B. (1981), "Direct Optical Measurements of Vorticity in a Nearly Turbulent Boundary Layer." F Thesis, Cornell University.

Frish, M.B. and Ferguson, R.D. (1990), "Vorticity Measurements in Couette Flow," Bull. Am. Phys. Soc., 35, 2252.

Gupta, A.K., Laufer, J., and Kaplan, R.E. (1971), "Spatial Structure in the Viscous Sublayer," J. Fluid Mech. 50, 493.

Hama, F.R., Long, J.D., and Hegarty, J.C. (1957), "On Transition From Laminar to Turbulent Flow," J. Appl. Phys. 28, 388.

Hama, F.R. (1963), "Progressive Deformation of a Perturbed Vortex Line Element," Phys. Fluids 6, 526.

Head, M.R. and Bandyopadhyay, P. (1981), "New Aspects of Turbulent Boundary Layer Structure," J. Fluid Mech. 107, 297.

Hinze, J.O. (1975), Turbulence, McGraw Hill.

Hussain, A.K.M.F. (1986), "Coherent Structures and Turbulence," J. Fluid Mech. 173, 303.

Hussain, A.K.M.F. (1983), "Coherent Structures - Reality and Myth," Phys. Fluids 26, 2816.

Jeffrey, J.F. (1922), "The Motion of Ellipsoidal Particles Immersed in a Viscous Fluid," Proc. Roy. Soc. A., 192, 161.

Kambe, T. (1986), "Acoustic Emissions by Vortex Motions," J. Fluid Mech. 173, 643.

Kastrinakis, E.G. and Eckelmann, H. (1983), "Measurement of Streamwise Vorticity Fluctuations in a Turbulent Channel Flow," J. Fluid Mech. 137, 165.

Kim, J. Moin, P., and Moser, R. (1987), "Turbulent Statistics in Fully Developed Channel Flow at Low Reynolds Number," J. Fluid Mech. 177, 133.

Kim, J. (1985), "Turbulence Structures Associated with the Bursting Event," Phys. Fluids 28(1), 52.

Klewicki, J.C. and Falco, R.E. (1990), "On Accurately Measuring Statistics Associated with Small-Scale Structure in Turbulent Boundary Layers Using Hot-Wire Probes," J. Fluid Mech. 219, 119.

Kline, S.J., Reynolds, W.C., Schraub, F.A., and Runstadler, P.W. (1967), "The Structure of Turbulent Boundary Layers," J. Fluid Mech. 30, 741.

Kücheman, D. (1965), "Report on the I.U.T.A.M. Symposium on Concentrated Vortex Motions in Fluids," J. Fluid Mech. 21, 1.

Landau, L.D. and Lifshitz, E.M. (1959), Fluid Mechanics, Pergamon.

Lang, D.B. and Dimotakis, P.E. (1982), "Measuring Vorticity Using the Laser Doppler Velocimeter," Bull. Am. Phys. Soc. 27, 1166.

Laufer, J. (1975), "New Trends in Experimental Turbulence Research," Ann. Rev. Fluid Mech. 7, 307.

Lee, M.J., Kim, J., and Moin, P. (1990), "Structure of Turbulence at High Shear Rate," J. Fluid Mech. 216, 561.

Lighthill, M.J. (1963), "Introduction: Boundary Layer Theory," in Laminar Boundary Layers - Chapter I: (Ed. L. Rosenhead) Oxford University Press.

Lin, C.J., Lee, K.J., and Sather, N.F. (1970), "Slow Motion of Two Spheres in a Shear Field," J. Fluid ? 43, 35.

Lin, C.T., Peery, J.H., and Schowalter, W. (1970), "Simple Shear Flow Round a Rigid Sphere: Inertial Effects and Suspension Rheology," J. Fluid Mech. 44, 1.

Lumley, J.L. (1981), "Coherent Structures in Turbulence, in Transition and Turbulence, (Ed. R.E. Meyer Academic Press.

Lumley, J.L. (1957) "Some Problems Connected with the Motion of Small Particles in Turbulent Fluid," I Thesis, Johns Hopkins University.

Moffatt, H.K. (1969), "The Degree of Knottedness of Tangled Vortex Lines," J. Fluid Mech. 35, 117.

Moin, P. and Kim, J. (1985), "The Structure of the Vorticity Field in Turbulent Channel Flow. Part I: Analysis of Vorticity Fields and Statistical Correlations," J. Fluid Mech. 155, 441.

Moore, D.W. and Saffman, P.G. (1975), "The Density of Organized Vortices in Turbulent Mixing Layer, Fluid Mech. 69, 465.

Perry, A.E. and Chong, M.A. (1987), "A Description of Eddying Motions and Flow Patterns Using Critic Point Concepts," Ann. Rev. Fluid Mech. 19, 125.

Perry, A.E. and Chong, M.S. (1982), "On the Mechanism of Wall Turbulence," J. Fluid Mech. 119, 173

Perry, A.E., Lim, T.T., and Teh, E.W. (1981), "A Visual Study of Turbulent Spots," J. Fluid Mech. 10? 387.

Piomelli, U., Balint, J.L., and Wallace, J.M. (1989), "On the Validity of Taylors Hypothesis for Wall-Bo Turbulent Flows," Phys. Fluids A 1, 609.

Pumir, A. and Siggia, E.D. (1987), "Vortex Dynamics and the Existence of Solutions to the Navier-Stoke Equations," Phys. Fluids 30(6), 1606.

Reichardt, H. (1956) "Uber Die Geschwindigkeitsverteilung in Einer Geradlinigen Turbulenten Couette-Strömung," ZAMM 36, 26 (Schlichting, (1979) Boundary Layer Theory.

Robinson, S.K. (1991), "Coherent Motions in the Turbulent Boundary Layer," Ann. Rev. Fluid Mech. 23

Rogers, M.M. and Moin, P. (1987), "The Structure of the Vorticity Field in Homogeneous Turbulent Flo J. Fluid Mech. 176, 33.

Saffman, P.G. and Baker, G.R. (1979), "Vortex Interaction," Ann. Rev. Fluid Mech. 11, 95.

Saffman, P.G. (1981), "Vortex Interactions and Coherent Structures in Turbulence," in Transition and Turbulence, (Ed. R.E. Meyer) Academic Press.

Schlichting, H. (1979), Boundary Layer Theory, McGraw Hill.

Smith. C.R. (1984). "A Synthesized Model of the Near-Wall Behavior in Turbulent Boundary Layer." Proc. Symp. Turb. 8th Rolla. Mo.

Taylor. G.I. (1936) "Fluid Friction Between Rotating Cylinders. Part II. Distribution of Velocity Between Concentric Cylinders when Outer One is Rotating and Inner One is at Rest." Proc. Roy. Soc. A 157, 565.

Tennekes. J. and Lumley. J.L. (1972). A First Course in Turbulence, MIT press.

Theodorsen. T. (1952). "Mechanisms of Turbulence." Proc. 2nd Midwestern Conference on Fluid Mech., Ohio State University.

Townsend. A.A. (1956) The Structure of Turbulent Shear Flow, Cambridge University Press.

Utami. T. and Ueno. T. (1987). "Experimental Study on the Coherent Structure of Turbulent Open-Channel Flow Using Visualization and Picture Processing." J. Fluid Mech. 173, 339.

Wallace. J.M. and Brodkey. R.S. (1977). "Reynolds Stress and Joint Probability Density Distributions in the U-V Plane of a Turbulent Channel Flow." Phys. Fluids 20, 351.

Wallace. J.M. (1986). "Methods of Measuring Vorticity in Turbulent Flows." Exper. in Fluids 4, 61.

Willmarth. W.W. and Tu. B.J. (1967). "Structure of Turbulence in the Boundary Layer Near the Wall." Phys. Fluids Supp. 10, 134.

Willmarth. W.W. and Lu. S.S. (1972). Structure of the Reynolds Stress Near the Wall." J. Fluid Mech. 55, 65.

Willmarth. W.W. (1975). "Structure of Turbulence in Boundary Layers." in Advances in Applied Mechanics, 15, 159 Academic Press.

Winant. C.D. and Browand. F.K. (1974). "Vortex Pairing: The Mechanism of Turbulent Mixing-Layer Growth at Moderate Reynolds Number." J. Fluid Mech. 63(2), 237.

Wyngaard. J.C. (1969). J. Phys. E:Sci. Instrum. 2, 983.

VOP Data Reduction and Hardware Simulation Program

```
C
                VERS. 6   DEC 90
C
C
SLARGE
C               ARRAY AND COMMOM DECLARATION
C
        REAL*4 RDATAX(1024)
      REAL*4 DDATAX(1024)
      REAL*4 SDATAX(1024)
        REAL*4 RDATAY(1024)
      REAL*4 DDATAY(1024)
      REAL*4 SDATAY(1024)
        REAL*4 CHIOPD(10)
        INTEGER*2 SQRFLG
        COMMON/FLG/SQRFLG
      COMMON/WDAT/W(1024),Y(1024),SINTX(1024),SINTY(1024),NCOUNT
        COMMON/CDAT/PERIOD,SCALE,YDET,SNOISE,BTX,BTY,CDHI,CDLO,CUTMAX,Q
        COMMON/OMEG/TM(1024),WX(1024),WY(1024),WZ(1024),NU(1024)
        COMMON/STAT/DWX(1024),DWY(1024),DWZ(1024),CHI2(1024)
        COMMON/MAP1/VXMAP(20,20),VZMAP(20,20)
        COMMON/MAP2/XP(20),ZP(20)
        COMMON/TIMR/TOTAL,LST,TSCA,NCSEG
        COMMON/BLIN/BERMAX,ISCRAP,IBENAB
        COMMON/PROX/PROXC,PROXW,PROXP,CLIPR
      CHARACTER*20 FXS,FXD,FYS,FYD,TSMP,ZNAME,FMAP
        INTEGER*2 OFF6,OFF7,OFF8,OFF9,OFF10
        LOGICAL LPOS,LTRS,LROUND,LTRS1,LTEST
        DATA IDFILE/5/
        DATA NSM/7/
        DATA NWORDS/1024/
        FMAP='C:\FORT50\MAP.DAT'
C
C
26      WRITE(*,'(A\)')' ENTER X SUM FILENAME: '
        READ (*,'(A)',ERR=26) FXS
C
C
27      WRITE(*,'(A\)')' ENTER X DIFF FILENAME: '
        READ (*,'(A)',ERR=27) FXD
C
C
28      WRITE(*,'(A\)')' ENTER Y SUM FILENAME: '
        READ (*,'(A)',ERR=28) FYS
C
C
29      WRITE(*,'(A\)')' ENTER Y DIFF FILENAME: '
        READ (*,'(A)',ERR=29) FYD
C
```

122

```fortran
      WRITE(*,'(A )')' ENTER TIMESTAMP FILENAME: '
      READ (*,'(A)',ERR=29) TSMP
C
C              READ DETECTOR MAP DATA FILE
C
      OPEN(IDFILE, FILE=FMAP, STATUS='OLD', FORM='FORMATTED')
      DO 13 L=1,20
      READ(IDFILE,*)PZ
      ZP(L)=PZ-.863
      XP(L)=.909-0.1*(L-1)
      DO 12 M=1,20
      READ(IDFILE,*)VXMAP(M,L),VZMAP(M,L)
12    CONTINUE
13    CONTINUE
      CLOSE(IDFILE)
C
C              OPEN DATA FILES
C
      OPEN(6, FILE=FXS, STATUS='OLD', FORM='UNFORMATTED')
      CALL CAT(6)
      OPEN(7, FILE=FXD, STATUS='OLD', FORM='UNFORMATTED')
      CALL CAT(7)
      OPEN(8, FILE=FYS, STATUS='OLD', FORM='UNFORMATTED')
      CALL CAT(8)
      OPEN(9, FILE=FYD, STATUS='OLD', FORM='UNFORMATTED')
      CALL CAT(9)
      OPEN(10, FILE=TSMP, STATUS='OLD', ACCESS='SEQUENTIAL',
     1 FORM='BINARY')
      CALL CAT(10)
C
C
C     SET INITIAL CODES AND COUNTERS
C
      NEV=1
      ISEG=0
      IBDSG1=999
      IBDSG2=999
      IAUTO=0
      ISM=0
      ITURN=0
      NEND=0
      NOPT=2
      IFLAG=0
      IFLAG2=0
      ISCRAP=0
      IBENAB=0
C
C
      WRITE(*,'(A\)')' ANY BAD SEGMENTS? ;'
      READ(*,'(I4)')IBDSG
      IF(IBDSG.EQ.1)THEN
      WRITE(*,'(A\)')' BAD SEGMENT 1 ;'
      READ(*,'(I4)')IBDSG1
```

123

```
                    WRITE(*,'(A\)')' BAD SEGMENT 2 :'
                    READ(*,'(I4)')IBDSG2
                    ENDIF
      C
                    WRITE(*,'(A\)')' CHANGE DEFAULT SUM NOISE?(1 = YES):'
                    READ(*,'(I4)')ICH
                    IF(ICH.EQ.1)THEN
      37            WRITE(*,'(A\)')' ENTER SUM NOISE LEVEL (VOLTS):'
                    READ(*,'(F12.7)',ERR = 37)SNOISE
                    IF(SNOISE.LT.0.001)GO TO 37
                    ENDIF
      C
      C
                    YDET = -1.9
      38            WRITE(*,'(A\)')' DETECTOR PLANE POSITION? (DFLT = -1.9):'
                    READ(*,'(I1)')NDET
                    IF(NDET.EQ.1)READ(*,'(F12.7)',ERR = 38)YDET
                    WRITE(*,'(A\)')'       Y = '
                    WRITE(*,1200)YDET
      C
      C       SET DEFAULT PARAMETERS
      C
                    NMIN = 25
                    NMAX = 650
                    TRS = 0.5
                    TRS1 = TRS
                    TOTAL = 0.0
                    HYS = 10.
                    NSM = 17
                    CDHI = 20.
                    CDLO = 2.0
                    CUTMAX = 5.0
                    BERMAX = 15.0
                    CLIPR = 0.06
                    RCUT = 2.
                    PROXC = .990
                    PROXW = .998
                    PROXP = .994
                    QDECR = 0.065
                    Q = 0.65
                    QDEF = Q
      C
      C       START BIG LOOP
      C
                    DO 11 ICSEG = 1,NCSEG
                    ISEG = ISEG + 1
      C
      C               BASELINE SUBTRACTION
      C
                    CALL BASE(6,OFF6,SDATAX,NEND,TIME)
                    IF(NEND.EQ.1)IFLAG = 1
                    CALL BASE(7,OFF7,DDATAX,NEND,TIME)
                    IF(NEND.EQ.1)IFLAG = 1
```

```
      CALL BASE(8.OFF8.SDATAY.NEND.TIME)
      IF(NEND.EQ.1)IFLAG = 1
      CALL BASE(9.OFF9.DDATAY.NEND.TIME)
      IF(NEND.EQ.1)IFLAG = 1
      CALL BASE(10.OFF10.DDATAY.NEND.TIME)
      TOTAL = TOTAL + TIME
      IF(IFLAG.EQ.1)THEN
      NSEG = ISEG-1
      WRITE(*,'(A\)')' END OF FILE ENCOUNTERED AT SEG#'
      WRITE(*,1201)NSEG
      GO TO 107
      ENDIF
C
      IF(ISCRAP.EQ.1)THEN
      WRITE(*,'(A\)')' BASELINE PROBLEM IN  SEG #'
      WRITE(*,1201)ICSEG
      ISCRAP = 0
      GO TO 11
      ENDIF
C
      IF((ICSEG.EQ.IBDSG1).OR.(ICSEG.EQ.IBDSG2))THEN
      WRITE(*,'(A\)')' SKIPPING BAD SEG #'
      WRITE(*,1201)ICSEG
      GO TO 11
      ENDIF
C
1200  FORMAT(F12.7)
1201  FORMAT(I3)
C
      IF(IAUTO.NE.1)THEN
      DO 1 I=1.NWORDS
      W(I)=(I-1)*PERIOD
1     CONTINUE
      ENDIF
C
3     IRET = 0
      IF(IAUTO.NE.1)THEN
C
C           SWITCH TO AUTOMATIC (NON-INTERACTIVE) REDUCTION MODE?
C
47    WRITE(*,'(A\)')' INTERACTIVE OR BATCH? (1=BATCH);'
      READ(*,'(I1)',ERR=47)IAUTO
C
C           VIEW RAW DATA?
C
251   WRITE(*,'(A\)')' DISPLAY X SUM? (1=YES);'
      READ(*,'(I1)',ERR=251)ITD
      IF(ITD.EQ.1)CALL FTDISP(SDATAX,1,0)
C
252   WRITE(*,'(A\)')' DISPLAY X DIFFERENCE? (1=YES);'
      READ(*,'(I1)',ERR=252)ITD
      IF(ITD.EQ.1)CALL FTDISP(DDATAX,1,0)
C
```

```
253      WRITE(*,'(A\)')' DISPLAY Y SUM? (1 = YES);'
         READ(*,'(I1)',ERR = 253)ITD
         IF(ITD.EQ.1)CALL FTDISP(SDATAY,1,0)
C
254      WRITE(*,'(A\)')' DISPLAY DIFFERENCE? (1 = YES);'
         READ(*,'(I1)',ERR = 254)ITD
         IF(ITD.EQ.1)CALL FTDISP(DDATAY,1,0)
C
C                CHANGE DEFAULT PARAMETER?
C
56       WRITE(*,1300)TRS
256      WRITE(*,'(A\)')'      SET NEW THRESHOLD? (1 = YES);'
         READ(*,'(I1)',ERR = 56)ICH
         IF(ICH.EQ.1)THEN
         READ(*,'(F12.5)',ERR = 56)TRS
         IF(TRS.LT.0.01)GO TO 56
         ENDIF
57       WRITE(*,1301)HYS,NSM
257      WRITE(*,'(A\)')' SET NEW VALUES? (1 = YES);'
         READ(*,'(I1)',ERR = 57)ICH
         IF(ICH.EQ.1)THEN
         WRITE(*,'(A\)')' SET HYSTERESIS( +/- % OF THRESHOLD); '
         READ(*,'(F12.5)',ERR = 57)HYS
         WRITE(*,'(A\)')' SET SMOOTHING PAD LENGTH; '
         READ(*,'(I3)',ERR = 57)NSM
         ENDIF
C
         IF(IBENAB.EQ.0)THEN
         WRITE(*,'(A\)')' BASELINE CHECKER IS OFF. TURN ON?(1 = YES)'
         READ(*,'(I1)')IBENAB
         ENDIF
C
58       WRITE(*,1302)BERMAX
258      WRITE(*,'(A\)')' RESET MAX BASELINE ERROR? (1 = YES);'
         READ(*,'(I1)',ERR = 58)ICH
         IF(ICH.EQ.1)THEN
         READ(*,'(F12.5)',ERR = 58)BERMAX
         ENDIF
C
         WRITE(*,212)QDECR
         WRITE(*,'(A\)')' NEW EDGE DECREMENT ? (1 = YES);'
         READ(*,'(I1)')ICH
         IF(ICH.EQ.1)READ(*,'(F12.5)')QDECR
C
         WRITE(*,2121)CLIPR
         WRITE(*,'(A\)')' NEW END CLIPPING FRACTION (1 = YES);'
         READ(*,'(I1)')ICH
         IF(ICH.EQ.1)READ(*,'(F12.5)')CLIPR
C
         WRITE(*,211)RCUT
         WRITE(*,'(A\)')' NEW FIT IMPROVEMENT RATIO ? (1 = YES);'
         READ(*,'(I1)')ICH
         IF(ICH.EQ.1)READ(*,'(F12.5)')RCUT
```

```fortran
C
C
      WRITE(*,'(A )')' CHANGE PROXIMTY COSINES?(1 = YES);'
      READ(*,'(I4)')ICH
      IF(ICH.EQ.1)THEN
      WRITE(*,'(A\)')' ENTER W II n COSINE (DEF .998);'
      READ(*,'(F12.7)')PROXW
      WRITE(*,'(A\)')' ENTER n II C COSINE (DEF .990);'
      READ(*,'(F12.7)')PROXC
      WRITE(*,'(A\)')' ENTER W II C COSINE (DEF .994);'
      READ(*,'(F12.7)')PROXP
      ENDIF
C
C
      WRITE (*,1303)NMIN
      WRITE(*,'(A\)')' NEW MIN TRAJ LENGTH ? (1 = YES);'
      READ(*,'(I1)')ICH
      IF(ICH.EQ.1)READ(*,'(I3)')NMIN
C
      WRITE (*,1304)NMAX
      WRITE(*,'(A\)')' NEW MAX LENGTH ? (1 = YES);'
      READ(*,'(I1)')ICH
      IF(ICH.EQ.1)READ(*,'(I3)')NMAX
C
      ENDIF
1300  FORMAT(' DEFAULT THRESHOLD IS CURRENTLY',F8.4,)
1301  FORMAT(' HYSTERESIS CURRENTLY',F8.4,', WITH',I3,' PT SMOOTHING')
1302  FORMAT(' DEFAULT BASELINE ERROR (NOISE LEVELS)',F8.4,)
1303  FORMAT(' DEFAULT MIN TRAJ LENGTH IS CURRENTLY ',I3,)
1304  FORMAT(' DEFAULT MAX TRAJ LENGTH IS CURRENTLY ',I3,)
C
      IF(IAUTO.NE.1)THEN
C
      DO 10 J = 1,NWORDS
      LTRS = (SDATAX(J) + SDATAY(J)).GT.TRS
      LPOS = (SDATAX(J).GT.0.0).AND.(SDATAY(J).GT.0.0)
      IF(LPOS.AND.LTRS)THEN
      RDATAX(J) = DDATAX(J)/SDATAX(J)
      RDATAY(J) = DDATAY(J)/SDATAY(J)
      ELSE
      RDATAX(J) = 0.0
      RDATAY(J) = 0.0
      ENDIF
10    CONTINUE
C
C         DISPLAY RAW QUOTIENTS?
C
      WRITE(*,'(A\)')' DISPLAY X QUOTIENT? (1 = YES);'
      READ(*,'(I1)')ITD
      IF(ITD.EQ.1)CALL FTDISP(RDATAX,1,0)
C
C
      WRITE(*,'(A\)')' DISPLAY Y QUOTIENT? (1 = YES);'
```

```
                    READ(*,'(I1)')ITD
                    IF(ITD.EQ.1)CALL FTDISP(RDATAY,1,0)
C

                    ENDIF
C
C
C       COMMENCE INNER LOOP: THRESHOLDING/MASKING/MAPPING/ANALYSIS
C
C
                    WRITE(*,'(A\)')' STARTING NEW SEGMENT #'
                    WRITE(*,1201)ICSEG
                    F=0.0
                    TRS1=TRS*(1.0-HYS/100.)
                    NCT=1
                    NSTRT=(NSM+1)/2
                    LLST=NSTRT+1
179                 IF(LLST.EQ.(NSTRT+1))THEN
                    SUMW2=0.0
                    DO 4 KK=1,NSM
                    SUMW2=SUMW2+SDATAX(KK)+SDATAY(KK)
4                   CONTINUE
                    ENDIF
C
                    BTX=0.0
                    BTY=0.0
                    SBTX=0.0
                    SBTX2=0.0
                    SBTY=0.0
                    SBTY2=0.0
C
                    DO 94 L=LLST,NWORDS-NSM
                    IF(F.EQ.1.0) GO TO 96
                    LST=L
                    NINC=L+NSTRT-1
                    NDEC=L-NSTRT
                    SUMW2=SUMW2+SDATAX(NINC)+SDATAY(NINC)-SDATAX(NDEC)-SDATAY(NDEC
                    LTRS=(SUMW2/NSM).GT.TRS
                    LTRS1=(SUMW2/NSM).GT.TRS1
                    LTEST=LTRS
                    IF(NCT.GT.NMIN)LTEST=LTRS1
                    LPOS=(SDATAX(L).GT.0.0).AND.(SDATAY(L).GT.0.0)
                    IF(LPOS.AND.LTEST)THEN
                    RDATAX(L)=DDATAX(L)/SDATAX(L)
                    RDATAY(L)=DDATAY(L)/SDATAY(L)
                    SBTX=SBTX+SDATAX(L)
                    SBTX2=SBTX2+SDATAX(L)*SDATAX(L)
                    SBTY=SBTY+SDATAY(L)
                    SBTY2=SBTY2+SDATAY(L)*SDATAY(L)
                    WT=RDATAX(L)
                    YT=RDATAY(L)
                    SQRFLG=0
                    CALL INTERP(WT,YT)
                    IF(SQRFLG.EQ.1)GO TO 11
```

```fortran
            W(NCT) = WT
            Y(NCT) = YT
            SINTX(NCT) = SDATAX(L)
            SINTY(NCT) = SDATAY(L)
            NCT = NCT + 1
            LROUND = (SQRT(WT*WT + YT*YT).GT.Q)
            IF(LROUND)THEN
            IF(NCT.LE.NMIN)THEN
            NCT = 1
            RDATAX(L) = 0.0
            RDATAY(L) = 0.0
            ELSE
            NCOUNT = NCT-2
            F = 1.0
            ENDIF
            ENDIF
            ELSE IF (NCT.LE.NMIN)THEN
            NCT = 1
            RDATAX(L) = 0.0
            RDATAY(L) = 0.0
            ELSE
            NCOUNT = NCT-1
            F = 1.0
            ENDIF
94          CONTINUE
            NCOUNT = NCT-1
96          F = 0.0
            IF(ICHI.EQ.0)LLLST = LST + 1
            IF(NCOUNT.GE.1)THEN
            BTX = SBTX2/SBTX
            BTY = SBTY2/SBTY
            ENDIF
            NCT = 1
C
            IF(NCOUNT.LE.NMIN)THEN
            WRITE(*,'(A)')' TOO FEW POINTS!!!'
            GO TO 103
C
            ELSE IF(NCOUNT.GE.NMAX)THEN
            WRITE(*,'(A)')' TOO MANY POINTS!!!'
            GO TO 103
C
            ELSE
            WRITE(*,'(I4)')NCOUNT
C
            IF(IAUTO.NE.1)THEN
C
C
C
            WRITE(*,'(A\)')' DISPLAY TRAJECTORY? (1 = YES);'
            READ(*,'(I1)')ITD
            IF(ITD.EQ.1)CALL FTDISP(Y,2,NCOUNT)
C
```

```fortran
C
        WRITE(*,'(A\)')' DISPLAY CORRECTED X QUOTIENT? (1 = YES);'
        READ(*,'(I1)')ITD
        IF(ITD.EQ.1)CALL FTDISP(W,3,NCOUNT)
C
C
        WRITE(*,'(A\)')' DISPLAY CORRECTED Y QUOTIENT? (1 = YES);'
        READ(*,'(I1)')ITD
        IF(ITD.EQ.1)CALL FTDISP(Y,3,NCOUNT)
C
C
        WRITE(*,219)QDEF
        WRITE(*,'(A\)')' NEW EDGE CUTOFF ? (1 = YES);'
        READ(*,'(I1)')ICH
        IF(ICH.EQ.1)THEN
        READ(*,'(F12.5)')QDEF
        Q=QDEF
        ENDIF
C
C
        WRITE(*,'(A\)')' ANOTHER PASS THROUGH THIS SET? (1 = YES);'
        READ(*,'(I1)')IRET
        IF(IRET.EQ.1)GO TO 8
C
        ENDIF
C
C
        IF(ICHI.EQ.1) THEN
        IF(NCLAST.EQ.NCOUNT)GO TO 101
        ENDIF
C
C       CALL THREE-COMPONENT VORTICITY LEAST-SQUARES FITTING ROUTINE
C
C
98      CALL OMEGA(NEV,IAUTO,ITURN,ICHI,CHIOP)
C
C
C             TEST FOR OPD EDGE EFFECTS
C
101     IF(ICHI.EQ.1)THEN
        NCHI=NCHI+1
        CHIOPD(NCHI)=CHIOP
        IF(NCHI.EQ.1)THEN
        WRITE(*,'(A)')' TAKING ANOTHER CUT'
        Q=Q-QDECR
        NCLAST=NCOUNT
        GO TO 179
        ENDIF
        IF(NCHI.GE.2)THEN
        RCHI=CHIOPD(NCHI-1)/CHIOPD(NCHI)
        IF(RCHI.GT.RCUT)THEN
        WRITE(*,'(A)')' TAKING ANOTHER CUT'
        Q=Q-QDECR
```

130

```
                NCLAST = NCOUNT
                GO TO 179
                ELSE
                WRITE(*,'(A)')' NO FURTHER IMPROVEMENT'
                IF(CHIOP.GE.CUTMAX)THEN
                WRITE(*,'(A)')' CHI SQUARE STILL TOO HIGH.  TRAJECTORY REJECTED'
                NEV=NEV-1
                ENDIF
                ENDIF
                ENDIF
                ENDIF
                ENDIF
                WRITE(*,'(A)')' LEAVING OMEGA'
                NEV=NEV+1
                NCOUNT=0
103             ICHI=0
                LLST=LLLST
                NCHI=0
                IF(LLST.LT.(NWORDS-2*NSM))GO TO 179
                Q=QDEF
11              CONTINUE
C
C               END OF OUTER LOOP
C
107             CLOSE(6)
                CLOSE(7)
                CLOSE(8)
                CLOSE(9)
C
C               WRITS DATA TO DISK
C
                WRITE(*,'(A\)')' ENTER FILENAME; '
                READ (*,'(A)') ZNAME
                OPEN(IDFILE,FILE=ZNAME,STATUS='NEW',ACCESS='SEQUENTIAL',
     1 FORM='FORMATTED')
                DO 109 J=1,NEV-1
                WRITE(IDFILE,193)TM(J),WZ(J),WX(J),WY(J)
                WRITE(IDFILE,200)DWZ(J),DWX(J),DWY(J),CHI2(J),NU(J)
109             CONTINUE
                CLOSE(IDFILE)
C
193             FORMAT(4(1PE12.5))
200             FORMAT(12X,4(1PE12.5),I4)
211             FORMAT('    DEFAULT FIT IMPROV. RATIO;',F12.4)
212             FORMAT('    DEFAULT EDGE DECREMENT;',F12.6)
2121            FORMAT('    DEFAULT TRAJ. ENDCLIP FRACTION;',F12.6)
219             FORMAT('    DEFAULT EDGE CUTOFF;',F12.5)
237             STOP
                END
C
C
C
                PLOTTING SUBROUTINE
```

```
C
C                    CALLS TO PLOT88 PLOTTING ROUTINES--NOT INCLUDED HERE
C
C
C

        SUBROUTINE CAT(JDFILE)
C
C           THIS SUBROUTINE READS LECROY 6810 SINGLE CHANNEL TIME DATA
C
C
C


        SUBROUTINE BASE(NCHAN,OFFSET,RDATA,NEND,TIME)
C
C               THIS SUBROUTINE SUBTRACTS THE MOST PROBABLE BASELINE
C               FROM THE RAW PSD SIGNALS
C
C
C


        SUBROUTINE INTERP(X,Z)
C
C               THIS SUBROUTINE PERFORMS A BILINEAR INTERPOLATION
C               ON THE NON-ORTHOGONAL DETECTOR MAP GRID TO FIND TRUE
C               REFLECTION COORDINATES
C
C
C
C
C
C
C               OMEGA3 VERS. 1  DEC 87
C
C
C       COMPUTES THETA,PHI AND ASSOCIATED COEFFICIENTS FROM X,Z PAIRS
C       COMPUTES dTHETA'/dt,dPHI'/dt ....ACCUMULATES SUMS, AND SOLVES
C       3X3 TO EXTRACT Wx, Wy, Wz.
C
        SUBROUTINE OMEGA(ISEG,IAUTO,ITURN,ICHI,CSUM)
        REAL*4 WGHTX(1024),WGHTZ(1024)
        REAL*4 SD(3),W(3)
        REAL*8 SA(5,5),DET,SS11,SS22,SS33,SS12,SS13,SS23
        INTEGER*2 SQRFLG
        COMMON/FLG/SQRFLG
        COMMON/OPDT/PHP(1024),THP(1024),PFUNC(1024),TFUNC(1024)
      COMMON/WDAT/WD(1024),YD(1024),SINX(1024),SINY(1024),NCOUNT
        COMMON/CDAT/PERIOD,SCALE,Y,SNOISE,BTX,BTY,CDEFHI,CDEFLO,CUTMAX,Q
        COMMON/OMEG/TM(1024),WX(1024),WY(1024),WZ(1024),NU(1024)
        COMMON/STAT/DWX(1024),DWY(1024),DWZ(1024),CHI2(1024)
        COMMON/TIMR/TOTAL,LST,TSCA,NCSEG
        COMMON/PROX/PROXC,PROXW,PROXP,CLIPR
        PI=3.14159
C
        WRITE(*,'(A)')' ENTERING OMEGA'
C       LOAD DATA
```

```
C
      SY = 1.0
      IF(Y.LT.0.0)SY = -1.0
      DT = PERIOD
      SNT = SNOISE
      AS = 0.0
      NP = 3
      ISUP = 1
C
C           CLEAN UP TRAJECTORY ENDPOINTS
C
      edg1 = SQRT(wd(1)*wd(1) + yd(1)*yd(1))
      edgn = SQRT(wd(ncount)*wd(ncount) + yd(ncount)*yd(ncount))

      I1 = 3
      IF(EDG1.LT.0.96*Q)I1 = 3 + INT(NCOUNT*CLIPR)
      I2 = NCOUNT-2
      IF(EDGN.LT.0.96*Q)I2 = NCOUNT-2-INT(NCOUNT*CLIPR)
C
C           COMPUTE SIGNAL-TO-NOISE STATISTICAL WEIGHTS
C           CORRECT OPTICAL DISTORTION
C
18    NMAX = I2-I1 + 1
      DO 3 I = 1,NMAX
      II = I + I1-1
      X = WD(II)
      Z = YD(II)
      WGHTX(I) = 2*SINX(II)*SINX(II)*Y*Y*DT*DT/(SNT*SNT*(1 + X*X))
      WGHTZ(I) = 2*SINY(II)*SINY(II)*Y*Y*DT*DT/(SNT*SNT*(1 + Z*Z))
      IF(ITURN.EQ.1)WGHTZ(I) = 0.0
      IF(ITURN.EQ.2)WGHTX(I) = 0.0
      RF = SQRT(X*X + Z*Z)
      RN = 1.284*ASIN(RF/1.284)
      X = X*RN/RF
      Z = Z*RN/RF
      PHP(I) = SY*PI/2.0-ATAN(X/Y)
      THP(I) = PI/2.0-ATAN(Z/SQRT(X*X + Y*Y))
C     WRITE(*,399)THP(I),PHP(I)
      N = I
3     CONTINUE
4     CONTINUE
C
C           INVOKE ORTHOGONAL POLYNOMIAL DECOMPOSITION
C
      CALL OPD(N,PHP,PFUNC,AP,BP,CP,DPH,BTX,CHP)
C
      CALL OPD(N,THP,TFUNC,AT,BT,CT,DTH,BTY,CHT)
C
      CSUM = CHP + CHT
      SNR = 0.5*(BTX + BTY)/SNOISE
      NOPT = 2*INT(0.2/SQRT((BT*BT + BP*BP)*SNR))
      IF(NOPT.LT.2)NOPT = 2
      IF(NOPT.GT.N/2)THEN
```

133

```
                    WRITE(*,'(A)')'    WARNING: NON-OPTIMUM DIFFERENCING NEEDED'
                    NOPT = N/2
                    ENDIF
C
                    DO 33 I = 1,N-1
33                  AS = AS + SQRT((PFUNC(I + 1)-PFUNC(I))**2 + (TFUNC(I + 1)-TFUNC(I))**2)
C
                    IF(IAUTO.NE.1)THEN
C
                    WRITE(*,'(A\)')' DISPLAY TRAJECTORIES? (1 = YES);'
                    READ(*,'(I1)')ITD
                    IF(ITD.EQ.1)CALL FTDISP(PHP,4,N)
C
                    WRITE(*,502)AP,BP,CP,DPH,BTX,CHP
                    WRITE(*,503)AT,BT,CT,DTH,BTY,CHT
                    WRITE(*,507)NOPT,N
C
                    CCUT = CDEFHI
                    CCUTLO = CDEFLO
36                  WRITE(*,506)CDEFHI,CDEFLO,CUTMAX
                    WRITE(*,'(A\)')' SET OPD CHI2S? (1 = YES);'
                    READ(*,'(I1)')ITD
                    IF(ITD.EQ.1)THEN
                    WRITE(*,'(A\)')' ENTER MAXIMUM ACCEPTABLE OPD CHI2;'
                    READ(*,*,ERR = 36)CDEFHI
                    WRITE(*,'(A\)')' ENTER MINIMUM SINGLE PASS VALUE;'
                    READ(*,*,ERR = 36)CDEFLO
                    WRITE(*,'(A\)')' ENTER MAXIMUM ACCEPTABLE CHI2 AFTER ALL CUTS;'
                    READ(*,*,ERR = 36)CUTMAX
                    CCUT = CDEFHI
                    CCUTLO = CDEFLO
                    ENDIF
                    ENDIF
C
                    IF(CSUM.GT.CCUT)THEN
                    WRITE(*,'(A)')'    OPD TRAJECTORY REJECTION!'
                    ISEG = ISEG-1
                    ICHI = 0
                    RETURN
                    ELSEIF((CSUM.GT.CCUTLO).AND.(CSUM.LT.CCUT))THEN
                    ICHI = 1
                    ELSE
                    ICHI = 0
                    ENDIF
C
C
C       INITIALIZE ARRAYS
C
                    S2 = 0.0
                    DO 6 K = 1,3
                    SD(K) = 0.0
                    W(K) = 0.0
                    DO 5 KK = K,3
```

134

```fortran
      SA(K,KK)=0.D0
5     CONTINUE
6     CONTINUE
C

      WRITE(*,'(A)')' ACCUMULATING SUMS'
C
C     COMPUTE DERIVATIVES, COEFFICIENTS, AND ACCUMULATE SUMS
C
      DO 7 L=1+NOPT/2,N-NOPT/2
      DTHPDT=(THP(L+NOPT/2)-THP(L-NOPT/2))/(NOPT*DT)
      DPHPDT=(PHP(L+NOPT/2)-PHP(L-NOPT/2))/(NOPT*DT)
C
      SQRFLG=0
      CALL TRANS(THP(L),PHP(L),SY,A,B,C,D,E,F)
      IF(SQRFLG.EQ.1)RETURN
C
      WGHTX(L)=NOPT*NOPT*WGHTX(L)/4.0
      WGHTZ(L)=NOPT*NOPT*WGHTZ(L)/4.0
C
      S2=S2+DTHPDT*DTHPDT*WGHTZ(L)+DPHPDT*DPHPDT*WGHTX(L)
C
      SD(1)=SD(1)+DTHPDT*A*WGHTZ(L)+DPHPDT*D*WGHTX(L)
      SD(2)=SD(2)+DTHPDT*B*WGHTZ(L)+DPHPDT*E*WGHTX(L)
      SD(3)=SD(3)+DTHPDT*C*WGHTZ(L)+DPHPDT*F*WGHTX(L)
C
      SA(1,1)=SA(1,1)+A*A*WGHTZ(L)+D*D*WGHTX(L)
      SA(1,2)=SA(1,2)+A*B*WGHTZ(L)+D*E*WGHTX(L)
      SA(1,3)=SA(1,3)+A*C*WGHTZ(L)+D*F*WGHTX(L)
      SA(2,2)=SA(2,2)+B*B*WGHTZ(L)+E*E*WGHTX(L)
      SA(2,3)=SA(2,3)+B*C*WGHTZ(L)+E*F*WGHTX(L)
      SA(3,3)=SA(3,3)+C*C*WGHTZ(L)+F*F*WGHTX(L)
7     CONTINUE
      IF(NP.EQ.2)THEN
      SA(3,3)=0.0
      SA(1,3)=0.0
      SA(2,3)=0.0
      SD(3)=0.0
      W(3)=0.0
      ENDIF
C
      SS11=SA(1,1)
      SS22=SA(2,2)
      SS33=SA(3,3)
      SS13=SA(1,3)
      SS23=SA(2,3)
      SS12=SA(1,2)
C
C
C     ... A SYMMETRIC MATRIX
C
      SA(3,2)=SA(2,3)
      SA(3,1)=SA(1,3)
      SA(2,1)=SA(1,2)
```

```
C
C        DO 20 M = 1,3
C20      WRITE(*,449)SD(M),SA(M,1),SA(M,2),SA(M,3)
C
C
C        WRITE(*,'(A)')' ENTERING MATINV'
         SQRFLG = 0
         CALL MATINV(SA,NP,DET)
         IF(SQRFLG.EQ.1)RETURN
C        WRITE(*,'(A)')' LEAVING MATINV'
C
         IF(DET.LE.0.0)THEN
         WRITE(*,'(A)')'     ERROR: SINGULAR MATRIX'
         ISEG = ISEG-1
         ICHI = 0
         RETURN
         ENDIF
C
C        DO 30 M = 1,3
C30      WRITE(*,450)SA(M,1),SA(M,2),SA(M,3)
C
C        COMPUTE Wx,Wy,Wz
C
         DO 9 I = 1,NP
         DO 8 J = 1,NP
         W(I) = W(I) + SA(I,J)*SD(J)
8        CONTINUE
9        CONTINUE
C
C        COMPUTE CHI-SQUARE AND UNCERTAINTIES
C
         NU(ISEG) = 2*N-7
         IF(ITURN.GE.1)NU(ISEG) = N-5
         CHID = W(1)*W(1)*SS11 + W(2)*W(2)*SS22 + W(3)*W(3)*SS33
         CHIC = 2.D0*(W(1)*W(3)*SS13 + W(1)*W(2)*SS12 + W(2)*W(3)*SS23)
         CHIY = -2.D0*(W(1)*SD(1) + W(2)*SD(2) + W(3)*SD(3))
         CHI2(ISEG) = (CHID + CHIC + CHIY + S2)/NU(ISEG)
C
         IF((SS11.LE.0.0).OR.(SS22.LE.0.0))THEN
         WRITE(*,'(A)')' ERROR: NON POSITIVE-DEFINITE DIAGONAL'
         ISEG = ISEG-1
         ICHI = 0
         RETURN
         ENDIF
C
         WZ(ISEG) = 2.*W(1)
         WX(ISEG) = 2.*W(2)
         WY(ISEG) = 2.*W(3)
         IF(SA(1,1).LT.0)THEN
         SQRFLG = 1
         RETURN
         ENDIF
         IF(SA(2,2).LT.0)THEN
```

136

```
                SQRFLG = 1
                RETURN
                ENDIF
                IF(SA(3,3).LT.0)THEN
                SQRFLG = 1
                RETURN
                ENDIF
                DWZ(ISEG) = 2.*SQRT(SA(1,1))
                DWX(ISEG) = 2.*SQRT(SA(2,2))
                DWY(ISEG) = 2.*SQRT(SA(3,3))
                TM(ISEG) = TOTAL + PERIOD*LST
C
C                  PROXIMITY TESTS
C
                AFLAG = 0.0
                IF(NP.EQ.2)GO TO 40
                UZ = COS(0.5*(AT + PI/2.0))
                UX = SIN(0.5*(AT + PI/2.0))*COS((0.5*AP)-PI/4.0)
                UY = SIN(0.5*(AT + PI/2.0))*SIN((0.5*AP)-PI/4.0)
                POLEY = -1
C
                UDOTW = 2.*(UZ*W(1) + UX*W(2) + UY*W(3))
                WMAG = 2.*SQRT(W(1)*W(1) + W(2)*W(2) + W(3)*W(3))
                TSTMAG = 2.*SQRT(W(1)*W(1) + W(2)*W(2) + AS*AS*W(3)*W(3))
                DWMAG = SQRT(DWZ(ISEG)*DWZ(ISEG) + DWX(ISEG)*DWX(ISEG) +
        1   AS*AS*DWY(ISEG)*DWY(ISEG))
                WDOTP = 2*W(3)/WMAG
                IF(WMAG.EQ.0)THEN
                WRITE(*,'(A)')' DIVIDE BY ZERO ERROR - SKIPPING SEGMENT'
                ISEG = ISEG-1
                ICHI = 0
                RETURN
                ENDIF
                THPAR = ABS(UDOTW/WMAG)
                IF(THPAR.GE.PROXW)THEN
                WRITE(*,'(A\)')' W NEARLY PARALLEL TO N!'
                ISEG = ISEG-1
                ICHI = 0
                RETURN
                ENDIF
                COSERR = TSTMAG/SQRT(TSTMAG*TSTMAG + DWMAG*DWMAG)
                IF((ABS(COSERR).LE.ABS(THPAR)).OR.
        1   (AS.LE.ACOS(ABS(UY))))AFLAG = 1.0
                IF(AFLAG.EQ.1.0)THEN
                WRITE(*,'(A\)')' W ERROR CONE CONTAINS N!'
                DZTMPR = DWZ(ISEG)
                DXTMPR = DWX(ISEG)
                DYTMPR = DWY(ISEG)
                ENDIF
C
40              IF(IAUTO.NE.1)THEN
                WRITE(*,500) WZ(ISEG),WX(ISEG),WY(ISEG)
                WRITE(*,501) DWZ(ISEG),DWX(ISEG),DWY(ISEG)
```

137

```
                    WRITE(*,499) NU(ISEG),CHI2(ISEG)
                    WRITE(*,504) UZ,UX,UY
                    WRITE(*,505) THPAR,COSERR,WDOTP
                    WRITE(*,508) AS
      C
      C

                    ENDIF
                    IF(AFLAG.EQ.1.0)THEN
                    IF((ABS(UY).LE.PROXC).OR.(THPAR.GT.ABS(UY)))THEN
                    ISEG=ISEG-1
                    ICHI=0
                    RETURN
                    ENDIF
      C             IF((ISUP.EQ.1).AND.(NP.EQ.3))THEN
                    NP=2
                    GO TO 18
      C             ELSE
      C             ISEG=ISEG-1
      C             RETURN
      C             ENDIF
                    ENDIF
                    IF(NP.EQ.2)THEN
                    DWZ(ISEG)=DZTMPR
                    DWX(ISEG)=DXTMPR
                    DWY(ISEG)=DYTMPR
      C             ICHI=0
                    ENDIF
      C
      C
      398           FORMAT( '0  THETA'    PHI'')
      399           FORMAT(2(1PD12.4))
      449           FORMAT( '0  ',1PD12.4,'  >  ',3(1PD12.4))
      450           FORMAT( '0  MATRIX INVERSE',3(1PD12.4))
      499           FORMAT( '0   CHI-SQUARE PER ',I4,' DEGREES OF FREEDOM = ',1PE12.4)
      500           FORMAT( '0  Wz=',1PE12.4,'   Wx=',1PE12.4,'   Wy=',1PE12.4)
      501           FORMAT( '0   +/-',1PE12.4,'    ',1PE12.4,'    ',1PE12.4)
      502           FORMAT( '0  PHI:',6(1PE12.4))
      503           FORMAT( '0  THETA:',6(1PE12.4))
      504           FORMAT( '0  Uz=',F12.6,'  Ux=',F12.6,'  Uy=',F12.6)
      505           FORMAT( '0   W;N COSINE',F12.6,' W;DW ',F12.6,' W;C ',F12.6)
      506           FORMAT( 'DFLTS; MAX',F12.6,' MIN',F12.6,' MAX AFTER CUTS ',F12.6)
      507           FORMAT( '0  OPTIMAL SAMLING NOPT=',I4,' OVER ',I4,' PTS')
      508           FORMAT( '0  TRAJ. ANGULAR SIZE',F12.6)
                    RETURN
                    END
      C
      C

                    SUBROUTINE TRANS(THP,PHP,SY,A,B,C,D,E,F)
      C
      C                   TRANSFORM TO UNPRIMED ANGLES, COMPUTE COEFFTS.
      C
      C
      C
```

138

```
        SUBROUTINE MATINV(ARR,N,DET)
C
C               MATRIX INVERSION ROUTINE
C
C
C
C

        SUBROUTINE OPD(N,Y,YFUNC,A,B,C,D,BT,CHI2)
C
C               ORTHOGONAL POLYNOMIAL DECOMPOSITION SUBROUTINE
C
C
C                       END
```

SNR Distribution

The signal-to-noise ratio (SNR) is determined by the ratio of the total incident power from a valid reflect and total equivalent noise power P_N. The noise power which has a variety of uncorrelated sources, predominantly fluctuating background light P_B and thermal detector noise P_T, is

$$P_N = \left(P_{B,rms}^2 + P_{T,rms}^2\right)^{1/2} \quad , \quad P_{T,rms} = NEP \cdot f^{1/2}$$

where NEP is the noise-equivalent power factor of the detector and f is the amplifier band-width. (Dete noise includes thermal noise and shot noise.) The noise voltage $V_{N,rms}$ is

$$V_{N,rms} = \left(V_{B,rms}^2 + V_{T,rms}^2 + V_{A,rms}^2\right)^{1/2}$$

with

$$V_{B,rms} = P_{B,rms} \cdot S_D \cdot R_T , \quad V_{T,rms} = NEP \cdot f^{1/2} \cdot S_D \cdot R_T , \quad V_{A,rms} = V_{A,rms}$$

where S_D is the detector sensitivity and R_T is the pre-amplifier transimpedance and $V_{A,rms}$ is the pre-ai voltage noise. The signal voltage is $V_s = P_I \cdot S_D \cdot R_T$.

Both the background fluctuation noise and the pre-amp noise are typically small compared to detector no the SNR is computed on the basis of this value. (In the unusual case where background fluctuations are errors are forced into χ_ν^2 goodness-of-fit parameter.) For NEP $= 10^{-11}W/\sqrt{Hz}$, $S_D = 0.5$ amps/W, . $R_T = 10^6$ V/amps, and the band-width f ~ 50 kHz, the detector noise $V_{N,rms}$ V, is approximately 1 m

The SNR is

$$SNR = \frac{V_s}{V_{N,rms}} = \frac{P_s}{P_{N,rms}} \quad .$$

Since V_N is constant, the instantaneous SNR is always proportional to V_s. The distribution of SNR over a data set is thus equivalent to the distribution of reflected laser power.

The distribution of reflected power is itself composed of variations due to random mirror positions within the Gaussian profile of the incident beam, and the variation of mirror diameter, d. The instantaneous reflected power is P_r

$$P_r(r,d) = I_o \frac{\pi}{\sqrt{2}} \left[\frac{d}{2}\right]^2 e^{-\frac{|\bar{r} - \bar{r_c}|^2}{2\sigma_B^2}} \tag{B-1}$$

where $|r - r_c|$ is the distance from the (axi-symmetric) beam center and σ_B is the beamwidth. The factor of $\frac{1}{\sqrt{2}}$ is included to account for the near 45 deg angle of inclination of the mirror-normal to the incident beam. The area of the hexagonal lead carbonate mirror is approximated by $\pi \left[\frac{d}{2}\right]^2$. In the special case where the flow velocity vector is parallel to the incident beam, then $P_r(r,d)$ is constant and given by Eq. (B-1). When the incident beam is inclined to the flow, the reflection intensity, and thus the SNR, varies with time and position

$$P_r(y,t,d) = I_o \frac{\pi}{\sqrt{2}} \left[\frac{d}{2}\right]^2 e^{-\frac{(ut\sin\lambda)^2}{2\sigma_B^2}} e^{-\frac{y^2}{2\sigma_B^2}} \tag{B-2}$$

where $\bar{u}$ is the flow velocity, λ is the angle between the velocity vector and the incident beam direction, and y is the coordinate perpendicular to both velocity and incident beam. This is illustrated in Figure B-1. Only two cases are considered, $\sin\lambda = 0$ and 1, i.e., parallel and perpendicular beam and velocity.
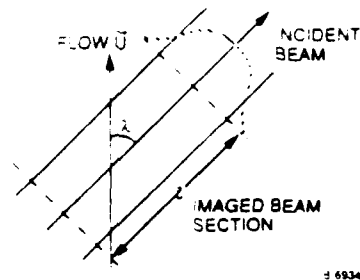
Figure B-1

Definition Sketch. Incident beam inclined to the flow gives rise to time varying SNR

A) $\sin \lambda = 0$

The incident light intensity in the sampled volume is

$$I(r) = I_o e^{-\frac{r^2}{2\sigma_b^2}}$$

But, $p(I)dI = p(r)dr$, and $p(r) = 2\pi r$, so

$$\phi_r(I) = 2\pi r \left|\frac{dr}{dI}\right|$$

eliminating r using Eq. (B-3)

$$p_I(I) = \frac{C}{I} \quad \text{for} \quad 0 < I < I_o \quad .$$

A threshold will determine the actual lower intensity limit, and thus the normalization c.

Mirror diameters are approximately log-normally distributed with most probable value d_o and log-normal width σ_d

$$p(d) \propto e^{-\frac{(\ln d - \ln d_o)^2}{2(\ln \sigma_d)^2}} \quad .$$

142

(For ZTX-B $d_o \sim 15 \ \mu m$, $\sigma_d \approx 4/3$.) The PDF for mirror area A is therefore

$$p_A(A) \propto \frac{1}{A} e^{-\frac{(\ln A - \ln A_o)^2}{2(\ln \sigma_d)^2}} \ .$$

The reflected power $P_r = IA$, thus $\ln(P_r) = \ln(I) + \ln(A)$ and

$$p(\ln Pr) = \int_{-\infty}^{\ln I_o} p_I(\ln I) p_A(\ln Pr - \ln I) d(\ln I) \ .$$

Integrated and transforming $\ln(P_r) \rightarrow P_r$,

$$p(SNR) = p_r(P_r) \propto \frac{1}{P_r} \ \mathrm{erf} \left[\frac{\ln(I_o/P_r A_o)}{2\sqrt{2} \ln \sigma_d} \right] \quad \propto \frac{P_N}{SNR} \ \mathrm{erf} \left[\frac{\ln \left[\frac{I_o \ P_N}{SNR \ A_o} \right]}{2\sqrt{2} \ \ln \sigma_d} \right] \ . \tag{B-4}$$

The threshold sets a minimum $P_{r,threshold}$ and determines the normalization constant. Note that the threshold interacts with the beam diameter through $P_{r,threshold} = IA_{threshold}$. Larger mirrors see, in effect, a larger beam diameter.

B) $\underline{\sin \lambda = 1}$

The situation for beam perpendicular to velocity vector is more complex. The mirror diameters are log-normally distributed as before, but now the threshold interacts with both beam diameter and transit time, depending upon where the particles traverse the beam profile. To simplify the discussion, it is assumed that σ_d is sufficiently small that mirror area $A = A_0$ and $P_{r,o} = I_o A_o$. From the expression for the intensity Eq. (B-3), the PDF of transit times at given $P_{r,threshold}$ is

$$p(\tau_{tr}) = \frac{\tau_{tr}}{\left[\frac{2\sigma_B^2}{u^2} \ln \left[\frac{P_{r,o}}{P_{r,threshold}} \right] - \tau_{tr}^2 \right]^{1/2}} \ .$$

143

Estimation of $\delta\dot{r}$, $\delta\dot{\psi}$, AND $\delta\left(\dfrac{\partial\psi}{\partial R}\right)$

In the optimum differencing discussion of Subsection 3.2.6, and optimum differencing interval was deriv

$$\Delta t_{opt} = m\Delta t = \frac{1}{\dot{r}\sqrt{SNR}} \quad .$$

An estimate of trajectory length (the fraction of the one radian detector surface angular diameter spanned trajectory) is

$$r_N \sim N\bar{\dot{r}}\Delta t = Nr_\Delta$$

where r_Δ is the average separation between adjacent samples. The relation for $\delta\bar{\dot{r}}$

$$\delta\bar{\dot{r}} = \left(\sigma_{\theta'}^2 + \sigma_{\phi'}^2\right)^{1/2} = \frac{\alpha\bar{\dot{r}}}{\sqrt{SNR}\sqrt{N}} = \frac{\alpha\bar{\dot{r}}\sqrt{r_\Delta}}{\sqrt{SNR}\cdot\sqrt{r_N}}$$

in terms of the trajectory angular size r_N, where α is a constant of order one. Similarly, for the angle $\dot{\psi} = \tan^{-1}\left(\dfrac{\dot{\theta}}{\dot{\phi}'}\right)$, the trajectory inclination with respect to the detector axes

$$\delta\dot{\psi} = \sigma_\psi = \frac{\alpha\sqrt{r_\Delta}}{\sqrt{SNR}\cdot\sqrt{r_N}} \quad .$$

When the component ω'_x, ω'_z can be approximated as $\omega'_z \approx \bar{\dot{r}}\cos\psi$, $\omega'_x = \bar{\dot{r}}\sin\psi$, then, clearly,

$$\delta\omega'_z, \delta\omega'_x = \left[\left(\delta\bar{\dot{r}}\right)^2\cos^2\psi + (\bar{\dot{r}}\delta\psi)^2\sin^2\psi\right]$$

and

$$\delta\omega'_z, \delta\omega'_x \sim \frac{\alpha\bar{\dot{r}}\sqrt{r_\Delta}}{\sqrt{SNR}\sqrt{r_N}} \quad .$$

This is only the case for trajectories passing close to the detector center. Typically, curvature-related errors $\left[\frac{\partial \psi}{\partial r}\right]$ will dominate.

The computation of $\delta(\partial\psi/\partial r)$ is more involved. Estimates of $\partial\psi/\partial r$, and $\delta(\partial\psi/\partial r)$ are

$$\left[\frac{\partial\psi}{\partial r}\right]_n = \frac{\psi_n - \overline{\psi}}{r_n - r_a} \quad , \quad \delta\left[\frac{\partial\psi}{\partial r}\right]_n \sim \frac{\delta\left(\psi_n - \overline{\psi}\right)}{r_n - r_a}$$

where r_a is the position of the trajectory centroid, i.e., the ath point divides the trajectory in half. With

$$\overline{\delta(\psi_n - \psi)} \approx \sigma_\psi$$

$$\sigma^2_{\frac{\partial\psi}{\partial r}} \approx \frac{\displaystyle\sum_{n=1, n\neq a}^{N} \left[\left(\frac{\psi_n - \overline{\psi}}{r_n - r_a}\right) - \frac{\overline{\partial\psi}}{\partial r}\right]^2 \frac{(r_n - r_a)^2}{\sigma^2_\psi}}{\displaystyle\sum_{n=1, n\neq a}^{N} \frac{(r_n - r_a)^2}{\sigma^2_\psi}}$$

$$= \frac{\sigma^2_\psi}{\displaystyle\sum_{n=1, n\neq a} (r_n - r_a)^2}$$

but $r_n - r_a$ can be approximated by $(n-a)\dot{r}\Delta t$ with $r_N = N\dot{r}\Delta t$

$$\sigma^2_{\frac{\partial\psi}{\partial r}} \approx \frac{6\sigma^2_\psi}{\dot{r}^2\Delta t^2 N^2} \quad \text{(large N)}$$

thus

$$\sigma_{\frac{\partial\psi}{\partial r}} \approx \frac{\sqrt{6}\,\alpha}{\sqrt{SNR}\,r_N} \quad .$$

145

Appendix D

Proximity Tests

The geometry of trajectories in the detector plane shown in Figure 17 forms the basis of another set of : particular, the vectors $\overline{a}$, $\overline{\gamma}$, and $\overline{c}$, are monitored in order to test for conditions leading to erroneous interpretations of data near the singularity in the VOP geometry ($\overline{\omega}$ parallel to $\overline{n}$). Since these tests use magnitudes $|\overline{a}|$, $|\overline{\gamma}|$, and $|\overline{c}|$, they are called proximity tests. There are three basic types:

1) Proximity to zero vorticity magnitude.

For a stationary reflection on the detector surface $|\overline{\gamma}| \rightarrow 0$. A finite SNR invariably leads to the misinterpretation of fluctuations or drift in its position as a rapid rotation about an axis nearly parallel to mirror-normal vector. It is highly improbable, however, that this rotation is real. Indeed, this would be interpreted as zero vorticity except for the fact that the uncertainty in the vorticity diverge near the VOP singularity.

$$\delta(\overline{\omega}_{\hat{n}}) \rightarrow \infty \text{ as } \overline{\omega}_{\hat{n}} \rightarrow c\hat{n} \quad .$$

One must interpret zero vorticity data carefully since it cannot be distinguished from contaminant or bui signals.

2) Test for $\overline{\omega}$ parallel to $\hat{n}$ within experimental uncertainty.

Erroneous curvature measurements for short, faster moving trajectory fragments tend to give $|\overline{\gamma}| \ll 1$ uncertainties of the ω components can be thought of as forming an ellipsoidal volume with semi-axes $\delta\omega_x$ $\delta\omega_y$ at the tip of each vorticity vector. The projection of the ellipsoid onto the plane perpendicular to the vorticity vector defines a conical region describing the range of possible orientations of the measured v vector within experimental error. If the mirror-normal vector falls within this cone, it is likely that err curvature dominates the vorticity measurement. (This is actually a special case of type (1).) A decision

then be made. When $|\bar{a}|$ is greater than a preset cutoff, the event is discarded. When $|\bar{a}|$ is less than the cutoff, the contamination of ω'_x and ω'_z due to ω'_y is within acceptable limits in which case only two components are fit and there is no measurement of ω'_y.

3) Test for $|\bar{c}| \ll 1$.

This indicates a measured vorticity consisting of almost pure ω_y. If this occurs, having passed the other tests, the trajectory is subjected to the same criteria as those failing test type (2).

Appendix E

Trajectory Length Distribution

In the following, $2\ell_{_\omega}$ represents the total angular size of a trajectory on the unit sphere limited only by time through the sampled volume, i.e., it is not restricted to that piece which would fall on the detector ($= D/2$) is the masked detector radius, and the random variable $d(k)(= 2r(k))$ is the fractional chord leng trajectory section on the detector surface, whose distribution is sought. ℓ, R, and r are used below for convenience (without subscripts).

The probability of finding a chord of (half) length r on a circle of radius R for a randomly placed segm length ℓ, in the plane of the circle is naturally divided into two regimes: $\ell > R$, and $\omega \le R$.

1) $\underline{\ell > R}$

This case is itself divided into two parts: full chords (spanning the circle), and partial chords (a segmer endpoint falling within the circle). The situation is illustrated in Figure E-1.
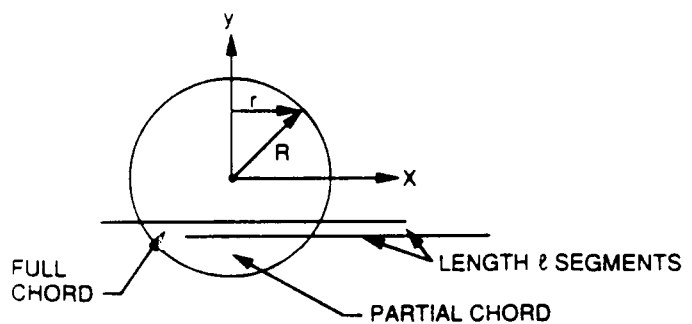

Figure E-1

Definition Sketch for Trajectory Length Distribution Derivation

148

The full chord distribution is

$$p_f(r; \; r \le R < \ell) = \frac{\ell - r}{\ell + r} \; \frac{r}{\sqrt{R^2 - r^2}} \quad .$$

The partial chord distribution is

$$p_p(r; \; r \le R < \ell) = \int_0^{\sqrt{R^2 - r^2}} \frac{2\sqrt{R^2 - y^2}}{\ell + \sqrt{R^2 - y^2}} \; dy$$

$$= 2\left\{ \sqrt{R^2 - r^2} + \ell \left[\sin^{-1}\left[\frac{r}{R}\right] - \frac{\pi}{2}\right] - \frac{\ell^2}{\sqrt{\ell^2 - R^2}} \left[\sin^{-1}\left[\frac{R^2 + r\ell}{R(r+\ell)}\right] - \frac{\pi}{2}\right] \right\} \quad .$$

The total PDF for case (1) is

$$p(r; \; r < R < \ell) = p_f(r) + p_p(r) \; , \; R < \ell$$

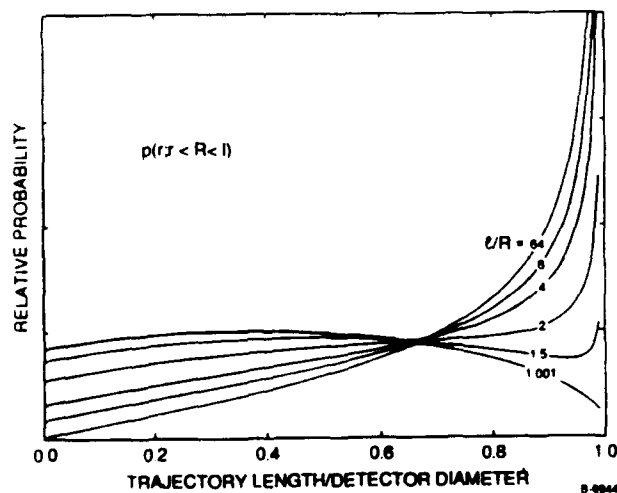which is shown in Figure 3E-2 at several ℓ/R ratios.

Figure E-2

PDFs of Trajectory Length for $\ell/R > 1$

149

2) $\ell < R$

There are four situations to be distinguished in this case: full chords confined to $y \geq \sqrt{R^2 - \ell^2}$, parti chords confined to this same region, partial chords of length ℓ for $y < \sqrt{R^2 - \ell^2}$, and partial chords region, $r < \ell$. The result

$$p(r; r < \ell < R) = p_1 + p_2 + p_3 + p_4$$

is shown in Figure E-3. The only point noted here is that p_3, for $r = \ell$, is a delta-function with amplitud dependant on ℓ/R which has been artificially broadened in the figure.

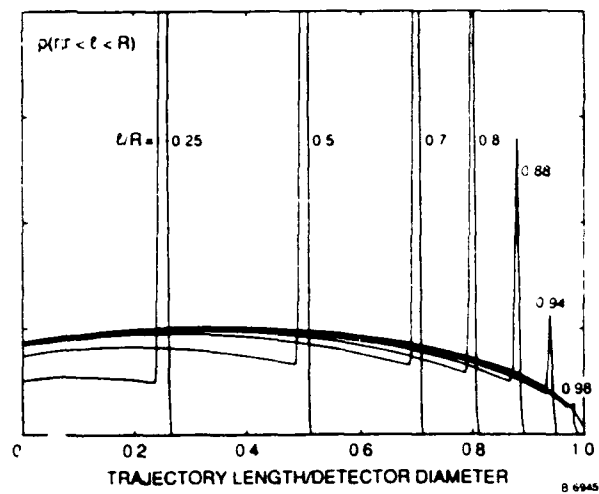When ℓ is itself randomly distributed, that distribution must be convolved with the PDFs above to find t

Figure E-3

PDFs of Trajectory Lengths for $\ell/R \leq 1$